©Copyright 2012
Stephanie E. Vasko

High Field Chemistry with Scanning Probes

Stephanie E. Vasko

A dissertation

submitted in partial fulfillment of the

requirements for the degree of

Doctor of Philosophy

University of Washington

2012

Reading Committee:

Marco Rolandi, Chair

Charles T. Campbell

Daniel R. Gamelin

Program Authorized to Offer Degree:

Chemistry

University of Washington

Abstract

High Field Chemistry with Scanning Probes

Stephanie E. Vasko

Chair of the Supervisory Committee:
Assistant Professor Marco Rolandi
Department of Materials Science & Engineering

Fabricating Ge and Si integrated structures with nanoscale accuracy is a challenging pursuit essential for novel advances in electronics and photonics. While several scanning probe-based techniques have been proposed, no current technique offers control of nanostructure size, shape, placement, and chemical composition. To this end, atomic force microscope direct write uses a high electric field (> 10^9 V m^{-1}) to create nanoscale features as fast as 1 cm s^{-1} by reacting a liquid precursor with a biased AFM tip. In this work, I present the first results on fabricating inorganic nanostructures via AFM direct write. Using diphenylgermane (DPG) and diphenylsilane (DPS), carbon-free germanium and silicon nanostructures (SIMS, x-ray PEEM) are fabricated. For this chemistry, I propose a model that involves electron capture and precursor fragmentation under the high electric field. To verify this model, experimental data and simulations are presented. High field chemistry for DPG and DPS has also been demonstrated for both sequential deposition and the creation of nanoscale heterostuctures, in addition to microscale deposition using a flexible stamp approach. This high field chemistry approach to the deposition of organometallic precursors could offer a low-cost, high throughput alternative for future optical, electronic, and photovoltaic applications.

TABLE OF CONTENTS

List of Figures		iv
List of Tables		vi
Glossary		vii
Acknowledgements		ix
Chapter 1:	Introduction	1
1.1	Introduction	1
1.2	Scanning Probes for Lithography	4
1.2.1	Scanning Probe Microscopy	4
1.2.2	Scanning Probe Lithography	6
1.3	This Thesis	12
1.4	References	14
Chapter 2:	Insights into the Scanning Probe High-Field Chemistry of Diphenylgermane	17
2.1	Introduction	17
2.2	Scanning Probe Lithography for Localized Chemistry	17
2.3	Temporary Negative Ion Model for the Deposition of Ge from DPG	21
2.4	Conclusions	34
2.5	References	34
Chapter 3:	Si and Ge Nanostructure AFM Direct Write	37
3.1	Introduction	37
3.2	Developing an AFM Direct Write Model for Inorganic Precursors of the form DPX	38

3.3 Conclusions 57

3.4 References 57

Chapter 4: Germanium Nanostructure Fabrication via AFM Direct Write 60

4.1 Introduction 60

4.2 Scanning Probe Direct Write of Ge Nanostructures 61

4.3 Ge Direct Write from DPG 63

4.4 Characterization of Nanostructures Fabricated by AFM Direct Write 67

4.4.1 Introduction to Characterization of Nanostructures Fabricated by AFM Direct Write 67

4.4.2 Time-of-Flight Secondary Mass Ion Spectroscopy 67

4.4.3 Photoemission Electron Microscopy for Near Edge X-Ray Absorption Fine Structure 72

4.4.4 PEEM-NEXAFS for C Content in AFM Direct Write Structures 78

4.4.5 PEEM-NEXAFS for Inorganic Content in AFM Direct Write Structures 84

4.4.6 Transmission Electron Microscopy 81

4.5 Conclusions 83

4.6 References 84

Chapter 5: Si, Ge, and $Si_{1-x}Ge_x$ Nanostructure Fabrication 88

5.1 Introduction 88

5.2 Serial Si, Ge, and $Si_{1-x}Ge_x$ Direct Write with Scanning Probes 89

5.3 Deposition of Ge and Si Hetrostructures 92

5.4 Characterization of Si, Ge, and $Si_{1-x}Ge_x$ Nanostructures 94

5.5 Reactive Stamping 99

5.5.1 Introduction to Reactive Stamping 99

5.5.2 Stamp Preparation 99

5.5.3 Proof-of-Concept Ge and Si Nanostructure Stamping on Si(100) 100

5.5.4 Large Area Reactive Stamping Using Photomask Aligner Technology 102

5.6 Conclusions 105

5.7 References 105

Bibliography 108

Appendix A: Experimental Methods for AFM Direct Write 115

Vita 117

LIST OF FIGURES

1.1 Photololithography Schematic 3

1.2 Scanning Tunneling Microscope/Atomic Force Microscope Schematic 5

1.3 STM-induced Chemical Vapor Deposition 8

1.4 General AFM Direct Write Schematic 11

2.1 AFM Direct Write Schematic with Applied Electric Field Simulations 20

2.2 I-V Curve and Simulation for DPG 22

2.3 Electron Impact Mass Spectrometer Schematic 25

2.4 Electron Impact Mass Spectrum for DPG 26

2.5 Heights and Widths of Fabricated Nanostructures 28

2.6 Current during writing 30

2.7 Volume and Reaction Efficiency 33

3.1 Generalized Direct Write Deposition Scheme 40

3.2 Band Diagram/Fowler Nordheim Tunneling Scheme 44

3.3 DPG and DPS UV-Visible Spectra 45

3.4 DPG and DPS I-V Curves 47

3.5 Volume versus voltage comparison for DPG and DPS 48

3.6 Electron Impact Mass Spectra for DPG and DPS 52

3.7 Collision Induced Dissociation EI-MS Data for DPG and DPS 53

3.8 Electron Impact Mass Spectra for DPG and DPS, sub-100 m/z 54

4.1 AFM Direct Write Schematic 64

4.2 Ge Nanostructures 65

4.3 Ge Nanostructure Height and Width 66

4.4 Time-of-Flight Secondary Ion Mass Spectroscopy 69

4.5 Ge Nanostructure Characterization by ToF-SIMS 71

4.6 Photoemission Electron Microscopy 74

4.7 Ge Nanostructure Carbon Characterization by PEEM-NEXAFS 77

4.8 Ge Nanostructure Germanium Characterization by PEEM-NEXAFS 80

4.9 Transmission Electron Microscopy 82

5.1 AFM Direct Write and Reactive Stamping Schematic 91

5.2 Ge, Si, and SiGe Heterostructures 93

5.3 Ge, Si, and SiGe Characterization by ToF-SIMS 95

5.4 Carbon comparison on Ge and Si Direct Write Nanostructures Using PEEM-NEXAFS 106

5.5 Si Nanostructure Carbon Characterization by PEEM-NEXAFS 97

5.6 Ge and Si Reactive Stamping 101

5.5 Mask Aligner Reactive Stamping Prototype 104

LIST OF TABLES

Table 2.1: DFT Simulation 24

GLOSSARY

AFM = Atomic Force Microscopy

CVD= Chemical Vapor Deposition

DEA = Dissociative Electron Attachment

DFT = Density Functional Theory

DPG = Diphenylgermane

DPS = Diphenylsilane

EA = Electron Affinity

HMDS = Hexamethyldisilazane

HOMO = Highest Occupied Molecular Orbital

IP = Ionization Potential

I-V = Current/Voltage

LAO= Local Anodic Oxidation

LUMO = Lowest Unoccupied Molecular Orbital

MOCVD = Metallorganic Chemical Vapor Deposition

NEXAFS= Near Edge X-ray Absorption Fine Structure

PEEM= Photoemission Electron Microscopy

SAM = Self-Assembled Monolayer

STM= Scanning Tunneling Microscopy

SPL= Scanning Probe Lithography

SPM= Scanning Probe Microscopy

TEM= Transmission Electron Microscopy

TNI= Temporary Negative Ion

ToF-SIMS= Time-of-Flight-Secondary Ion Mass Spectroscopy

UV-Vis = Ultraviolet-Visible

VASP = Vienna Ab-initio Simulation Package

ACKNOWLEDGEMENTS

I would like to thank Professor Rolandi for the opportunity to work on this project. I'd like to thank my group members, especially Dr. Jessica Torrey and Adnan Kapetanovic for their assistance with this research and for their discussions in the lab. Additionally, I'd like to thank the members of my committee for taking the time out of their busy schedules to offer suggestions and critiques that have helped me to improve my research: Dr. Lloyd Burgess, Dr. Suzanne Gage Brainard, Dr. Charlie Campbell, Dr. Scott Dunham, and Dr. Daniel Gamelin.

I'd like to thank the team of Dr. Andreas Scholl, Dr. Tony Young, and Dr. Andrew Doran at ALS Beamlines 11.0.1 (PEEM-3) and 7.3.1 (PEEM-2) for helping me with the NEXAFS-PEEM experiments. I'd like to thank Dr. Zhihua Zhu at Pacific Northwest National Laboratory for ToF-SIMS work. I'd also like to thank Dr. Martin Sadilek for his aid in performing EI-MS at the University of Washington and for his insightful discussions and persistent optimism. I'd like to thank Renyu Chen, Wenjun Jiang, and Haoyu Lai of the Dunham group for their collaborative efforts in understand the AFM direct write model and their insightful comments and discussions. I'd like to thank Dr. Marjorie Olmstead, Dr. Melissa Eblen-Zayas, John Cosgrove, and Allan Hodge for their mentoring and support over the past few years.

Finally, I would like to thank my family and friends for their continued support during my educational journey. To my friends for giving me a shoulder to cry on and a sounding board for research questions. To the people I've dragged into running with me or forced to listen to me talk about running, thanks for supporting my crazy quest to run a marathon in the last year of my Ph.D. To my dad, for his advice that the same reason they call it fishing instead of catching is the same reason they call it doing experiments and to my mom for always picking up the phone.

To both of my parents for their continued support. Without all of you, this would not have been possible.

CHAPTER 1: Introduction

1.1. Introduction

Originally, lithography (from the greek (*λίθος* - *lithos*, 'stone' + *γράφειν* - *graphein*, 'to write') was a technique wherein an image is created in a wax or oily surface that has been applied to a stone. Ink is then placed on the surface, and by pressing the surface to paper; the ink is transferred in the form of the pattern onto the paper.

The invention of the transistor in 1947 and the development of the first integrated circuit in 1958[1] forever altered the definition of lithography. While lithography for artistic applications has adapted to meet changing technology, lithography for micro and nanostructure fabrication has evolved to match and enable technological innovation. As technology has grown and generations of applications have demanded progress, so has lithography evolved to meet this challenge. From the microscale structure of the single transistor in 1958 to Intel's 22 nm 3D Tri-Gate,[2] increasing the amount of circuits on a chip and decreasing the size of each circuit has become the goal of lithography. In addition to being an excellent way to reproduce art and produce micro/nanoscale electronics, lithographic development has become a catalyst for the understanding and development of new chemistries.[3,4]

Initial lithographic techniques for microcircuit components were based on optical exposure of a photosenstivie chemical, called a resist. The resist is applied to a silicon wafer, and when exposed to light through a mask with the desired patterns, either undergoes a photochemical reaction to become soluble (positive resist) or is prevented from becoming soluble (negative resists) when rinsed in a developer solution (Figure 1.1).[1] The mask in photolithography plays the same role as the stone in conventional

lithography. Initial photolithography schemes used a photomask in direct contact with the substrate to be patterned. Since then, photolithography has evolved from noncontact photomask use to mask projection.[5] In this scheme, light is shined through the mask, which is then focused through a lens before reaching the substrate. While this has allowed for smaller feature size and greater mask reuse, the fundamental feature size that can be produced by this technique is limited by the wavelength of light. Several alternatives have been proposed to reach smaller feature sizes, including the shorter wavelength light (extreme ultraviolet light (EUV)) and nanoimprint lithography, which creates features much like copying a CD from a master.[1] Scanning probe based techniques, which can be used in ambient conditions and do not require the use of light for patterning, have also been suggested as a possible alternative. These techniques are especially attractive because they can operate “maskless;” many scanning probe techniques can directly pattern a substrate without the use of a template in a process known as direct write.

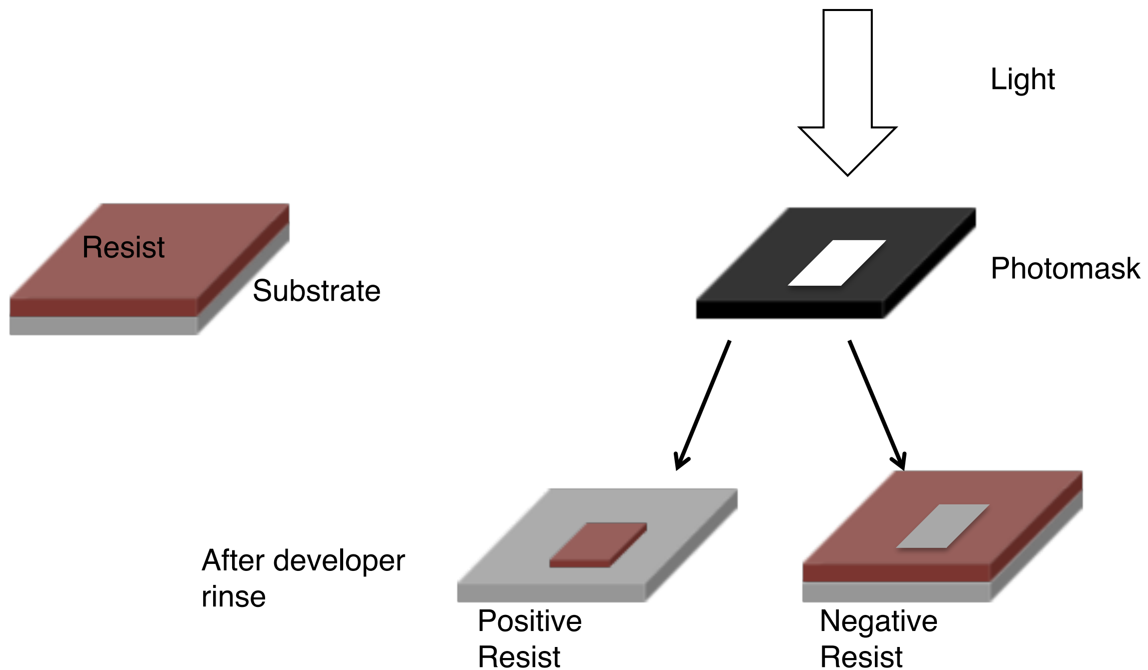

Figure 1.1. Generalized photolithography process. First, a chemical resist is applied to a substrate, such as a silicon wafer. A patterned mask, called a photomask is placed over the substrate and then the mask and substrate are exposed to light. If the resist that is used is a positive tone resist, when developed, the area exposed to light will remain and the rest of the resist will be removed. If the resist that is used is a negative tone resist, when developed, the area exposed to light will be removed and the rest of the resist will remain.

1.2 Scanning Probes for Lithography

1.2.1 Scanning Probe Microscopy

The field of scanning probe-based lithography (SPL) began with the invention of the scanning tunneling microscope (STM) by Binning and Rohrer in 1982; originally conceived as a high-resolution metrology tool for imaging surfaces.[6] Subsequent research on scanning probe techniques resulted in the development of the atomic force microscope (AFM) in 1986. While STM and AFM perform the same general function, i.e. the topographical imaging of a sample, they differ in the principal method in which they achieve this image. In STM, a voltage is applied to the tip, and when the tip is sufficiently close enough to the sample for electrons to tunnel through the tip to the sample, a current can be measured (Figure 1.2a). This current, called the tunneling current, is monitored as the tip scans across the sample. STM performs imaging by monitoring the tunneling current while the tip-sample is kept constant. STM imaging gives topographical information on an atomic scale.[7] AFM also produces topographical images, but is based on monitoring the force between the tip and substrate (Figure 1.2b). In brief, a sharp tip is brought near a surface and various forces between the tip and substrate cause the tip to be deflected. This deflection is monitored by focusing a laser on the cantilever on which the tip is mounted and monitoring the deflection of the laser with a photodetector. These deflections are the basis of the topographic image. AFM can be operated in ambient conditions. The high spatial resolution of SPM techniques as well as the localized interaction area between the tip and sample prompted the expansion of SPM techniques from metrology to lithography.

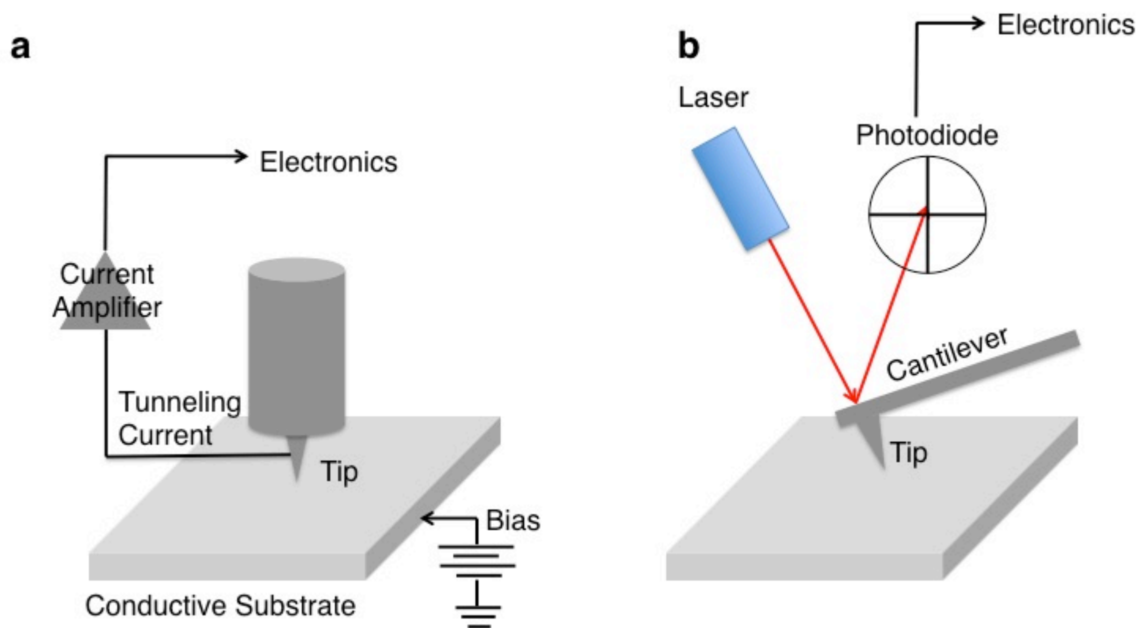

Figure 1.2. Schematic of the scanning tunneling microscope (a) and atomic force microscope (b).

1.2.2 Scanning Probe Lithography

Scanning probe microscope (SPM)-based techniques for nanofabrication utilize the limited tip-sample interaction area to confine chemical reactions either by delivering a stimuli,[3] such as heat or an electric field, or a reactant,[8] such as additional molecules, to the sample surface. These techniques merge the spatial precision of SPM with nanoscale compositional control for a wide range of applications from semiconductor heterostructures to biological self-assembly. In addition, they also provide interesting case studies for using new methods to performing existing or new chemical reactions. Reactions of interest have ranged from click chemistry[9] and Diels-Alder[9,10] reactions to thermochemical reactions of resist materials[11] for 2D and 3D nanostructures.[12-15]

Nanostructure for integrated circuit technology via SPL has been the subject of both STM and AFM-based techniques over 20 years. Many of these techniques are based on the application of a voltage between the tip and a conductive substrate that induces a large electric field.[3,7,16] The voltage, field, or a combination of both is used to perform localized chemistry. One of the first methods towards this goal was the introduction of STM-induced chemical vapor deposition (Figure 1.3). While traditional CVD requires a heated substrate for decomposition of a gaseous precursor material, energy can be supplied to the precursor molecules by an applied voltage from the STM.[17] This process was first demonstrated to deposit Cd on Si(111) using gaseous dimethylcadmium on Si(111),[18] and has been followed by the deposition of Al on Si(001) and Si(111) from trimethylaluminum gas[17], ~ 5nm Si based structures using SiH_4 gas on Si(111),[19] and Fe from iron pentacarbonyl [$Fe(CO)_5$] gas on Si(111) substrates.[20] Unfortunately, this technique requires the STM to be housed in an ultrahigh vacuum chamber, and that a

large quantity of gaseous precursor is used for each deposition. Furthermore, in STM, the voltage and current are linked to imaging. In AFM, these parameters are not linked to imaging, allowing fine-tuning during the lithography. Moving from STM to AFM techniques allows for more control over more of the deposition variables.

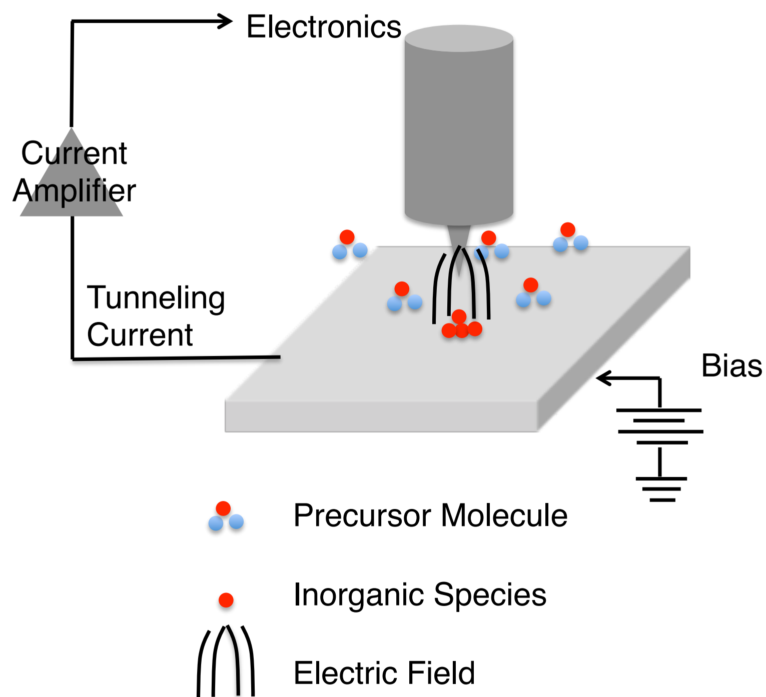

Figure 1.3 STM-induced Chemical Vapor Deposition Schematic.

AFM can not only operate at faster than STM,[21] but can also be used to fabricate nanostructures in ambient conditions.[22-25] At these conditions, a water meniscus can be formed between an AFM tip and substrate. Using the water meniscus in combination with an applied voltage, redox chemistry can be performed at the surface. Local anodic oxidation was first developed for the scanning tunneling microscope[26,27] and expanded to the atomic force microscope.[3,28] Using the nanoscale water meniscus, silicon can be oxidized, and nanoscale silicon oxide patterns formed by scanning substrate with respect to the AFM tip. The meniscus formed acts like a nanoelectrochemical cell which contains 5×10^4 molecules.[3] Menisci of 20 nm are easily reproducible and can lead to sub-10 nm oxidized features.[3] Additionally, changing the humidity can change the feature size produced by the oxidation technique. Additional STM and AFM techniques for the electrochemical deposition of metal structures have been demonstrated. These techniques require the desired material to first be deposited on the tip. Methods for depositing material on the tip range from evaporation to electrochemical plating.[29-31] Using a series of voltage pulses, material can be transferred from the tip to the surface via field evaporation.[29-31]

Further expansion of the localized oxidation technique to oxidation through self-assembled monolayers (SAMs) has proven useful.[32] In experiments where a conductive surface such as a semiconductor or metal surface is treated with a SAM, local oxidation can also be performed. Previous research on Ti surfaces treated with large carbon-based branched molecules indicated that the Ti layer was oxidized through the SAM.[32] Additionally, however, it was noted that the molecules themselves were being degraded by the large electric field present between the tip and the sample and depositing on the Ti

surface as amorphous carbon[32]. This novel outcome prompted the study of conventional and affordable sources of carbon material in the tip-sample gap.

Work by Fréchet *et al*. replaces the water meniscus or SAM in the experiments described above with an immersion of the tip and the substrate in an organic solvent.[33] A biased AFM tip traces desired shapes along the silicon sample while immersed in a liquid organic precursor or meniscus condensed from a saturated inorganic precursor (Figure 1.3). During this process, carbonaceous nanostructures are deposited. Organic liquids such as toluene, n-octane, ethyl alcohol, and dioxane have been used as organic precursors in the tip/sample gap.[33,34] Using octane and 1-octane vapors, it was determined that the growth rate of nanostructures is modified by the composition of the solvent.[35] From this technique, 2 nm wide structures with a periodicity of 6 nm could be fabricated.[36] Previously, spatially controlled synthesis of fluorocarbon nanowires from a perfluorooctane precursor on a Si(100) with a native oxide layer has been demonstrated.[21] These structures could be written as fast as 1 cm/sec and as narrow as 28 nm.[21] While the experiments described above illustrate the capability of the AFM to directly fabricate structures of a desired chemical composition, until now, AFM direct write has been limited to organic features. While STM-CVD, as discussed above, could produce inorganic features, it has been limited by slow fabrication speeds and the use of only gaseous precursors.

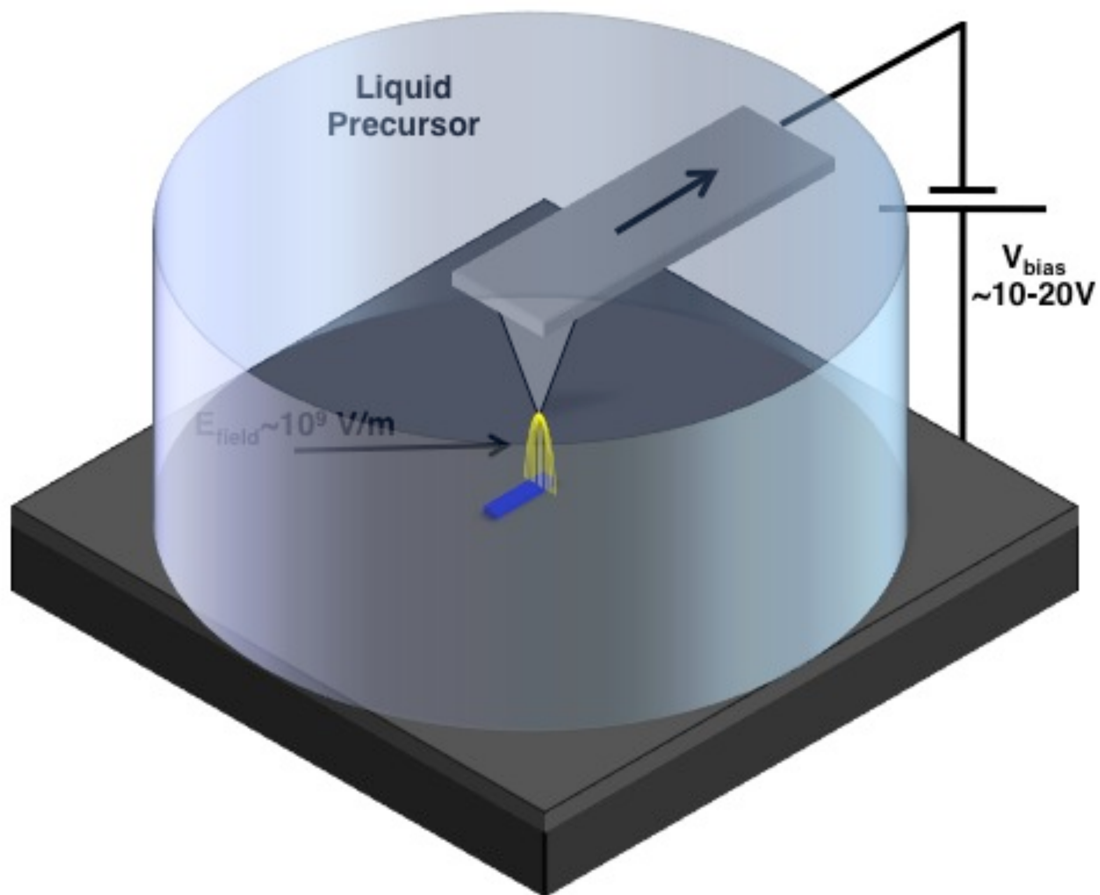

Figure 1.4 AFM Direct Write Schematic. The liquid precursor in which the tip and substrate are submerged defines the chemistry of the final nanostructure. Using water as a precursor (in a condensed meniscus) yields the formation of oxides, using organic solvents yields the formation of carbonaceous features, and in this thesis, I introduce using inorganic precursors to fabricate inorganic nanostructures.

1.3 This Thesis

In this thesis, I demonstrate the first application of AFM direct write for the fabrication of inorganic nanostructures. AFM direct write of inorganic nanostructures combines the functionalities added using STM-assisted CVD with the speed and operating conditions of AFM-based techniques. By replacing the organic precursor in the work described above with an inorganic precursor, inorganic nanostructures can be produced by AFM direct write.

Germanium and silicon were selected as the target materials due to their wide application for electrical and optical applications. Several factors were examined in choosing an appropriate inorganic precursor for AFM direct write of carbon-free inorganic nanostructures including: commercial availability, immunity to water-driven or gaseous parasitic reactions, benign leaving groups, and carbon content. Diphenylgermane (DPG) and diphenylsilane (DPS) were chosen for several reasons: they are commercially available, stable in the liquid form at room temperature, contain potentially good leaving groups, and DPG has been demonstrated in the past as a precursor for carbon-free synthesis of Ge nanowires.[37]

This thesis will also explore the unique high field chemical reaction occurring in the tip-sample gap. Due to the tip-sample proximity, even a moderate bias of 10 V can induce an electric field on the order of 10^9 V m^{-1}. In high electric fields above 10^9 V m^{-1}, new pathways in chemical reactions may be established.[38] In high fields, electronic orbitals are distorted in such a way that the chemical characteristics of a molecule are altered.[38] Working in the high field regime opens the possibility of utilizing the new chemical pathways that are a result of the stabilization of otherwise unstable atoms,

molecules, or radicals.[38]

Chapter II discusses the initial efforts on understanding the chemical reaction of diphenylgermane in the tip-sample gap. Initial experiments confirmed the feasibility of AFM direct write of Ge nanostructures from diphenylgermane. In Chapter II, I propose an initial model for the deposition process during AFM direct write. The model is based on the formation of a temporary negative ion and its subsequent fragmentation. As mentioned earlier, the tip-sample gap is a unique nanoscale environment where highly-localized chemical reactions can occur. These reactions are probed experimentally and via simulation (performed in collaboration with the Dunham group, UW Dept. of Electrical Engineering) to develop an initial model.

Chapter III further probes the localized reaction chemistry in the tip-sample gap. A series of experiments designed to tackle the proposed steps of a generalized reaction mechanism for group IVb DPX (X=Ge, Si) molecules is presented. Additionally, deposition of Si from diphenylsilane is presented along with a discussion of the differences in deposition between Si from DPS and Ge from DPG.

In Chapter IV, the flexibility of AFM direct write is demonstrated. AFM direct write can be used to control the size, shape, and composition of a fabricated nanostructure. In this chapter, the direct write of Ge from diphenylgermane is explored. A characterization scheme for materials deposited using AFM direct write is discussed in this chapter, including the use of ToF-SIMS and NEXAFS-PEEM for initial carbon content analysis. Efforts towards microstructure characterization via transmission electron microscopy are presented as well.

Chapter V demonstrates the serial and parallel patterning of Si, Ge, and $Si_{1-x}Ge_x$ nanostructures from DPS, DPG, and a DPS/DPG mixture. Characterization of these structures is presented. Additionally, the expansion of this technique to heterostructure fabrication and reactive stamping are demonstrated and a discussion of upscaling reactive stamping to wafer-scale throughput is presented. Low-cost, high throughput of semiconductor heterostructures also remains a challenge. To this end, parallel patterning using the high field direct write technique has been demonstrated using a flexible stamp approach. By substituting the AFM probe with conductive, microstructured stamps, the high field chemical reaction can be scaled up from one reaction site at the tip-sample gap to a user-defined large array of reaction sites.

1.4 References

1 Landis, S. *Nano-Lithography*. (Wiley, 2011).

2 Intel. *Moore's Law Inspires Intel Innovation*, <http://www.intel.com/content/www/us/en/silicon-innovations/moores-law-technology.html> (2012).

3 Garcia, R., Martinez, R. V. & Martinez, J. Nano-chemistry and scanning probe nanolithographies. *Chemical Society Reviews* **35**, 29 (2006).

4 Ito, H. Chemical Amplification Resists: History and Development within IBM. *IBM Journal of Research Development* **41**, 119-130 (1997).

5 Fuller, G. E. in *SPIE.* 14-27.

6 Bard, A. J. & Faulkner, L. R. *Electrochemical Methods*. Second edn, (John Wiley & Sons, 2001).

7 Soh, H. T., Guarini, K. W. & Quate, C. F. *Scanning Probe Lithography*. (Kluwer Academic Publishers, 2001).

8 Ginger, D. S., Zhang, H. & Mirkin, C. A. The evolution of dip-pen nanolithography. *Angewandte Chemie-International Edition* **43**, 30-45 (2004).

9 Gotsmann, B., Duerig, U., Frommer, J. & Hawker, C. J. Exploring chemical switching in a diels-alder polymer for nanoscale probe litohography and data storage. *Advanced Functional Materials* **19**, 1499-1505 (2006).

10 Long, D. A., Unal, K., Pratt, R. C., Malkoch, M. & Frommer, J. Localized "click" chemistry through dip-pen nanolithography. *Advanced Materials* **19**, 4471-4473 (2007).

11 Vettiger, P. *et al.* The "Millipede"-More than thousand tips for future AFM storage. *IBM Journal of Research Development* **44**, 323-340 (2000).

12 Fenwick, G. *et al.* Thermochemical nanopatterning of organic semiconductors. *Nature Nanotechnology* **4**, 664-668 (2009).
13 Knoll, A. W. *et al.* Probe-Based 3-D Nanolithography Using Self-Amplified Depolymerization Polymers *Advanced Materials* **22** (2010).
14 Pires, D. *et al.* Nanoscale Three-Dimensional Patterning of Molecular Resists by Scanning Probes. *Science* **328**, 732-735 (2010).
15 Szoszkiewicz, R. *et al.* High-Speed, Sub-15 nm feature size thermochemical nanolithography. *Nano Letters* **7**, 1064-1069 (2007).
16 Li, Y., Maynor, B. W. & Liu, J. Electrochemical AFM "Dip-Pen" Nanolithography. *Journal of American Chemical Society* **123**, 2105-2106 (2001).
17 Laracuente, A., Bronikowski, M. J. & Gallagher, A. Chemical Vapor Deposition of Nanometer-Size Aluminum Features on Silicon Surfaces Using an STM Tip. *Applied Surface Science* **107**, 11-17 (1996).
18 Ehrichs, E. E., Yoon, S. & de Lozanne, A. L. Direct writing of 10 nm features with the scanning tunneling microscope. *Applied Physics Letters* **53**, 2287-2289 (1988).
19 Rauscher, H., Behrendt, F. & Behm, R. J. Fabrication of surface nanostructures by scanning tunneling microscope induced decomposition of SiH4 and SiH2Cl2. *Journal of Vacuum Science & Technology B* **15**, 1373-1377 (1997).
20 Kent, A., Shaw, T., von Molnar, S. & Awschalom, D. D. Growth of High Aspect Ratio Nanometer-Scale Magnets with Chemical Vapor Deposition and Scanning Tunneling Microscopy. *Science* **262**, 1249-1252 (1993).
21 Rolandi, M., Suez, I., Scholl, A. & Frechet, J. M. J. Fluorocarbon Resist for High-Speed Scanning Proble Lithography. *Angewandte Chemie-International Edition* **46**, 7477-7480 (2007).
22 Rolandi, M., Quate, C. F. & Dai, H. A New Scanning Probe Lithography Scheme with a Novel Metal Resist *Advanced Materials* **14**, 191-194 (2002).
23 Germain, J., Rolandi, M., Backer, S. A. & Frechet, J. M. J. Sulfur as a novel nanopatterning material: an ultrathin resist and a chemically addressable template for nanocrystal self assembly. *Advanced Materials* **20**, 4526-4529 (2008).
24 Torrey, J. D. *et al.* Scanning Probe Direct-Write of Germanium Nanostructures. *Advanced Materials* **22**, 4639-4642 (2010).
25 Vasko, S. E. *et al.* Insights into the high field chemistry of diphenylgermane. *Physical Chemistry Chemical Physics* **13**, 4842-4845 (2011).
26 Dagata, J. A. *et al.* Modification of hydrogen-passivated silicon by a scanning tunneling microscope operating in air. *Applied Physics Letters* **56**, 2001-2003 (1990).
27 Day, H. C. & Alleee, D. R. Selective Area Oxidation of Silicon With Scanning Force Microscope. *Applied Physics Letters* **62**, 2691-2693 (1993).
28 Snow, E. S. & Campbell, P. M. Fabrication of Si Nanostructures with an Atomic Force Microscope. *Applied Physics Letters* **64**, 1932-1934 (1994).
29 Kolb, D. M., Ullman, R. & Will, T. Nanofabrication of Small Copper Clusters on Gold(111) Electrodes by a Scanning Tunneling Microscope. *Science* **275**, 1097-1099 (1997).
30 Wei, Y.-M. *et al.* The Creation of Nanostructures on an Au(111) Electrode by Tip-Induced Iron Deposition from an Ionic Liquid. *Small* **4**, 1355-1358 (2008).

31 Song, J. Q. *et al.* Fabrication of Gold Nanostructures on Graphite Using Atomic Force Microscope. *Molecular Crystal Liquid Crystal Science and Technology Section A* **294-295**, 51 (1997).

32 Rolandi, M., Suez, I., Dai, H. & Frechet, J. M. J. Dendrimer Monolayers as Negative and Positive Tone Resists for Scanning Probe Lithography. *Nano Letters* **4**, 889-893 (2004).

33 Suez, I., Backer, S. A. & Frechet, J. M. J. Generating an Etch Resistant "Resist" Layer From Common Solvents Using Scanning Probe Lithography in a Fluid Cell. *Nano Letters* **5**, 321-324 (2005).

34 Tello, M. & Garcia, R. Giant growth rate in nano-oxidation of p-silicon surfaces by using ethyl alcohol liquid bridges. *Applied Physics Letters* **83**, 2339-2341 (2003).

35 Martinez, R. V. & Garcia, R. Nanolithography Based on the Formation and Manipulation of Nanometer-Size Organic Liquid Menisci. *Nano Letters* **5**, 1161-1164 (2005).

36 Martinez, R. V., Losilla, N. S., Martinez, J., Huttel, Y. & Garcia, R. Patterning polymeric structures with 2 nm resolution at 3 nm half pitch in ambient conditions. *Nano Letters* **7**, 1846-1850 (2007).

37 Chockla, A. M. & Korgel, B. A. Seeded germanium nanowire synthesis in solution. *Journal of Materials Chemistry* **19**, 996-1001 (2009).

38 Kreuzer, H. J. Physics and Chemistry in High Electric Fields. *Interface Analysis* **36**, 372-379 (2004).

CHAPTER 2: Insights into Scanning Probe High-Field Chemistry of Diphenylgermane

Abstract

Experiments and simulations are used to elucidate a new class of chemical reactions occurring near the tip–sample interface during high field chemistry of diphenylgermane. Current data during writing and bias dependent growth rate are analyzed, supplemented with data from ionization mass spectrometry, and compared with the simulation results.

2.1 Introduction

In determining a suitable model for precursor deposition, inspiration was drawn from the vast history of SPM techniques. By directly writing semiconductor nanostructures in ambient conditions, AFM direct write merges the added functionality of STM-CVD with the experimental conditions of the direct write of carbonaceous features. The initial model for nanostructure fabrication via AFM direct write of inorganic precursors draws upon models developed for STM-CVD, but adapted to ambient conditions and a liquid-phase precursor.

In conjunction with the Dunham research group (University of Washington Dept. of Electrical Engineering), I propose a model that involves electron capture and precursor fragmentation in this unique high field (10^9 V m^{-1}) nanoscale environment. To verify this theory, experimental data and simulations are used to elucidate the chemical reactions occurring near the tip–sample interface during high field chemistry of diphenylgermane semiconductors. Current data during writing and bias dependent growth rate are analyzed, supplemented with data from ionization mass spectrometry, and compared with the simulation results.

This chapter is presented in a similar form as it was published in *Physical Chemistry Chemical Physics* (Vasko, S. E. *et al.* Insights into the high field chemistry of

diphenylgermane. *Physical Chemistry Chemical Physics* **13**, 4842-4845 (2011), http://pubs.rsc.org/en/content/articlelanding/2011/cp/c0cp02150d).[1] Reproduced by permission of the PCCP Owner Societies.

2.2 Scanning Probe Lithography for Localized Chemistry

Scanning probe microscopes can confine chemical reactions at the nanoscale through the delivery of specific stimuli[2] or reactants[3] to a small area of the sample surface. This confinement can be used to produce chemical patterns with well defined functionality by exploiting macroscale reactions such as “click” chemistry and Diels-Alder coupling.[4,5] Nanoscale thermochemistry is also available with heated tips to create 2D and 3D patterns in reduced graphene,[6] or polymeric[7,8] and macromolecular resists.[9] Another common strategy for reaction confinement is to apply a moderate bias between the tip and the sample. In humid environment, the water meniscus at the tip sample interface is often described as a nanoscale electrochemical cell where H^+ and OH^- are created. The extremely high electric field (> 10^9 V m^{-1}) arising from tip-sample proximity directs the desired ions onto the sample, which is oxidized or reduced depending on bias. In this fashion, the field-induced oxidation or reduction of conducting substrates[10-12] and organic monolayers[13,14] has been demonstrated. Recent efforts in replacing the water meniscus in the tip-sample gap with menisci of organic and inorganic molecules have introduced a novel class of chemical reactions that do not seem to follow a clear electrochemical pathway. It has been previously theorized that these reactions are triggered by the high electric field and are analogous to the processes occurring in field ionization microscopes.[15] These reactions include self-assembled monolayer activation,[16-18] polymer cross linking,[19] sulfur polymerization,[20] and localized synthesis of carbon nanostructures from liquid[21-24] or gaseous precursors.[25] Kinetic studies

of carbon growth have found trends in agreement with the high-field conjecture, but a conclusive model for the localized high field chemistry is still lacking. Most recently, the localized high-field reaction of diphenylgermane via AFM has demonstrated the direct-write of germanium nanofeatures.[26] Remarkably, this process produces carbon-free germanium, suggesting that, unlike the growth process of carbon nanostructures, the reaction of the inorganic precursor follows a very specific pathway. Diphenylgermane thus presents a model system to better understand the high field chemistry occurring near the tip-sample interface.

In this chapter, an attempt at understanding the fundamental processes occurring in the high-field reaction of diphenylgermane (DPG) by comparing experimental results from AFM writing and electron ionization mass spectroscopy with simulations is presented. In brief, a biased AFM tip traces desired shapes along the silicon sample while a diphenylgermane meniscus is condensed via saturated vapor at the tip-sample interface (Figure 2.1a). Due to tip-sample proximity, even a moderate 10 V bias induces an electric field with peak values above 10^9 V m^{-1} (Figure 2.1b) near the tip-sample interface. Here, we propose that the high electric field leads to electrons tunneling from the AFM tip to the DPG molecule creating a temporary negative ion (TNI).[27] In the high electric field, the charged DPG then fragments, leading to carbon-free germanium nanostructures. We propose a reaction where phenyl groups and hydrogens leave the diphenylgermane as benzene, which is a stable leaving group. The benzene most likely dissolves into the DPG meniscus. The germanium, in form of ions or radicals, then condenses onto the surface to form nanostructures (Figure 2.1a). Carbon-free low-temperature synthesis of germanium nanowires from DPG has previously been demonstrated,[28] suggesting that DPG is a viable precursor for this chemistry.

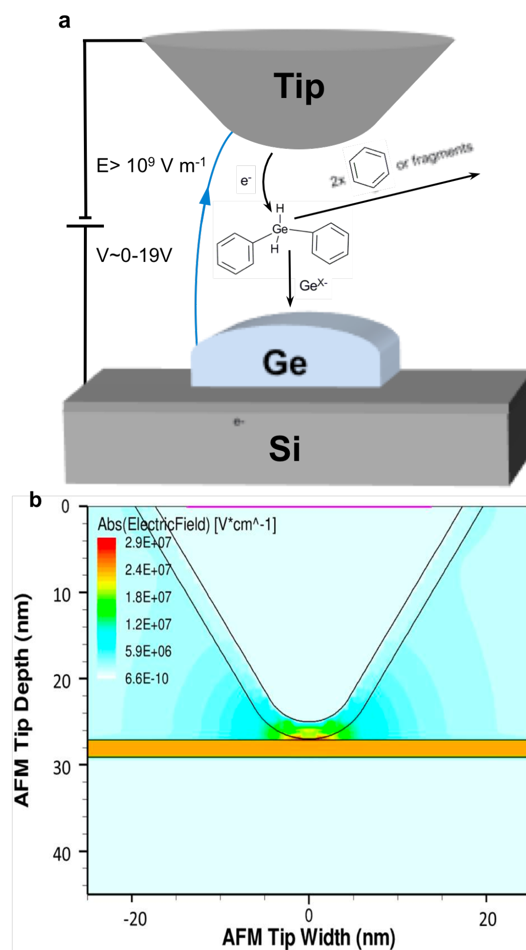

Figure 2.1 a) Schematic of the probe-sample geometry and the proposed chemical reaction of DPG for Ge nanostructure AFM direct write. b) Calculation of electric field distribution (V cm^{-1}) Si AFM tip in diphenylgermane in contact with Si substrate (3.5 nm oxide) biased at 10 V. The calculation includes distribution of ionized precursors in DPG and thin oxide on both tip and substrate.

2.3 Temporary Negative Ion Model for the Deposition of Ge from DPG

To test the first part of our model, we have measured the current across the tip-sample interface with stationary tip as a function of applied voltage and compared it with the prediction of simulations that consider non-local tunneling across the SiO_2 layers on the substrate and tip (Figure 2.2). During this measurement, the use of the DPG meniscus ensures that all the current measured goes through the reaction area. The onset of the current at 8±1 V corresponds to the predicted onset for electron emission from the AFM tip into the diphenylgermane liquid. For negative voltages as low as –20 V (sample), the current follows a linear behavior and no deposition occurs. For positive voltages on the sample, a reaction threshold is observed after the onset of field emission. These results are consistent with previous STM observations of field emission and dielectric breakdown in liquid octane.[29]

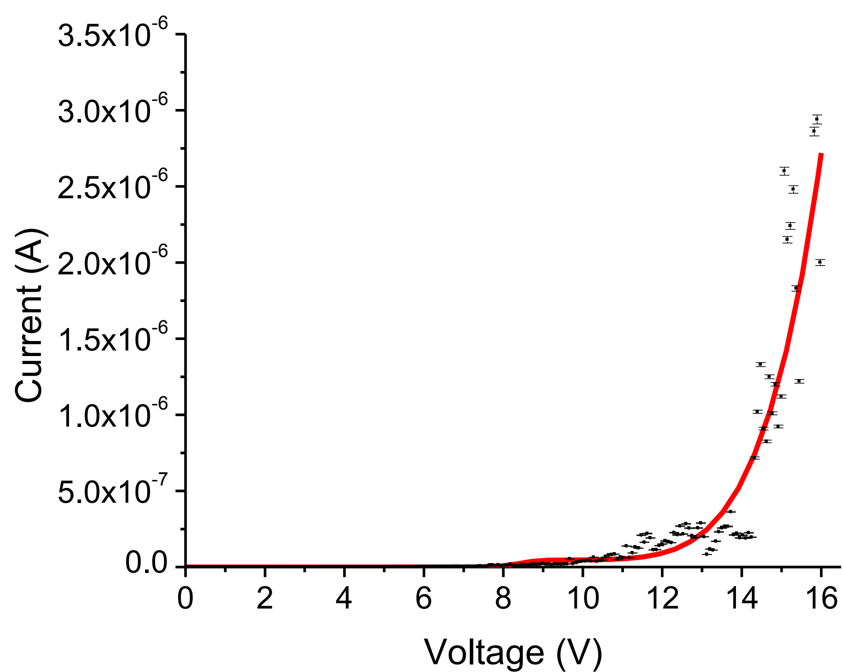

Figure 2.2 Current versus applied voltage (measured positive on the sample) obtained in a single I-V sweep with stationary tip (black points). Simulation of current between sample and tip including non-local tunneling model using structure matched to experimental conditions (red line).

Insights into the potential fragmentation routes were provided by density functional theory (Table 1). From these calculations, it emerges that electron capture by DPG greatly reduces the dissociation energy, with the lowest energy occurring for the separation of a benzene molecule from DPG. This dissociation route becomes energetically favorable upon electron capture. These calculations are consistent with our proposed model. Ideally, one would directly verify the reaction pathway by collecting intermediate fragments during AFM writing. However, the sub-attomolar quantities of precursor reacted in this process do not allow for such analyses. To overcome these issues, mass spectrometry data from electron ionization was collected (Figure 2.3, 2.4). A similar strategy was previously adopted to explain STM induced reactions of gaseous precursors.[27] In such experimental set-up, a field equivalent to the one present during AFM writing cannot be induced. However, using mass spectrometry of the precursor liquid, electron attachment fragmentation routes can still be verified. In an effort to reproduce the AFM conditions, the lowest energy electrons (17 eV) that would give a reasonable signal to noise ratio were employed. This energy is comparable to the energy of the electrons emitted from the AFM tip. In electron ionization mass spectromertry (EI-MS), electrons boil off of a heated metal filament and are accelerated towards an anode. A sample is introduced into the chamber, where interactions between the electron and sample molecules can cause the formation of the expulsion of an electron (formation of a molecular ion), positive fragments, radicals, and neutral fragments.[30] This technique works by detecting positively charged fragments, therefore, radical and neutral fragments are undetected.[30]

Electron impact mass spectrometry of diphenylgermane was performed using a JEOL HX-110 magnetic sector mass spectrometer at the University of Washington Department of

Chemistry Mass Spectrometry Facility. Small quantities of diphenylgermane liquid (Gelest) were introduced into the system via capillary tube. Negative ion spectra were collected in electron impact ionization mode with 17 eV electrons (Figure 2.4). Electron ionization spectra were analyzed using the MASPECII32 data acquisition interface (Mass Spectrometry Services, Ltd., Manchester, UK).

From this data, it is clear that during electron ionization the route that leads to a diphenylgermane fragmenting into benzene and a phenylgermane radical is a favorable one. The signature for fragments of Ge attached to other smaller organic fragments does not appear in this low-energy electron spectrum in agreement with the AFM findings of creating a carbon-free Ge product.

E_d	System Charge (q)		
Fragment	0	-1	-2
$(C_6H_5)^0$	3.77	1.84	1.83
$(C_6H_5)^-$	7.25	2.71	0.91
$(C_6H_6)^0$	1.05	-0.10	-0.08

Table 2.1 Dissociation Energies (E_d) for diphenylgermane as function of system charge and identity of the removed fragment.

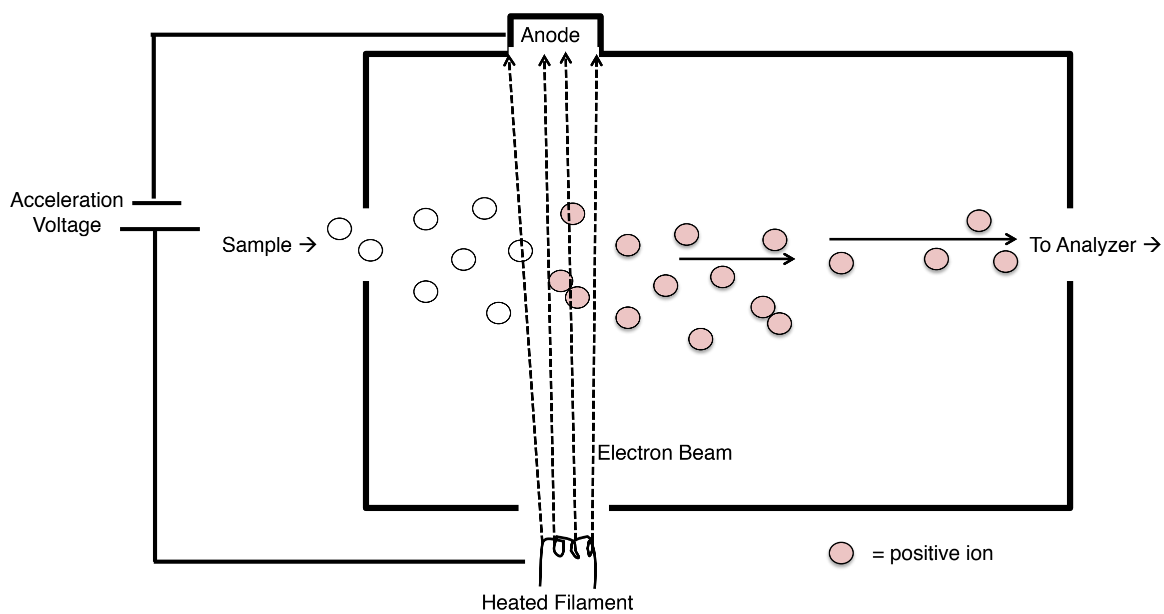

Figure 2.3 Electron Ionization Mass Spectrometer Schematic

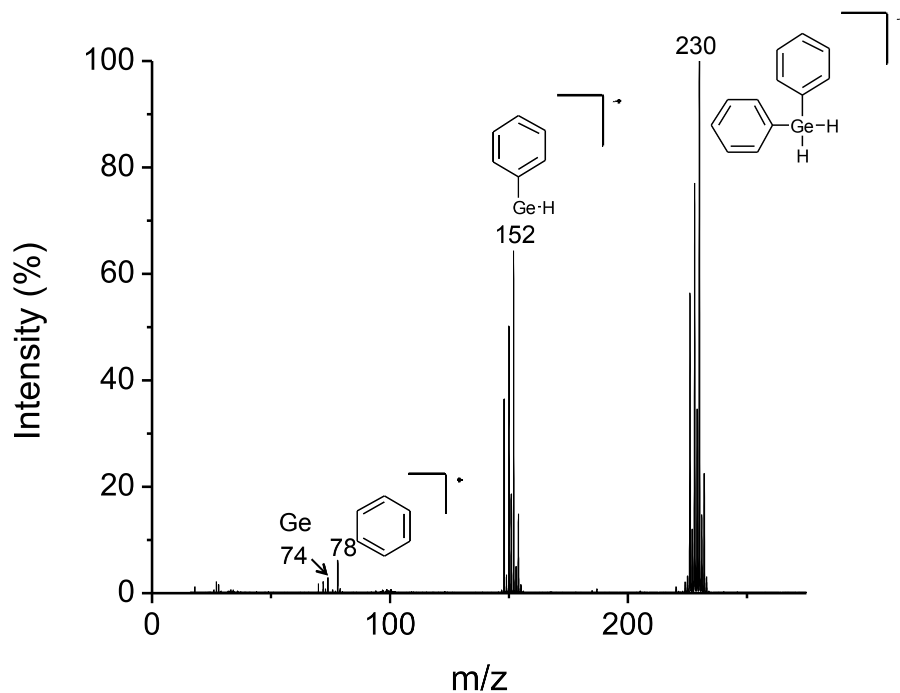

Figure 2.4 Electron Ionization Mass spectroscopy data acquired from liquid diphenylgermane using 17 eV ionization electrons. The signature of positive molecular fragments corresponding to diphenylgermane molecular ion (230 amu), phenylgermane radical cation (152 amu), benzene cation (78 amu), and germanium radical cation(74) are clearly discernible and dominate the spectra. The spectra are consistent with the isotopic abundances of C, and Ge as well as loss of 1 additional H from the Ge complexes.

To further understand the writing process, we have produced features with different bias voltages (Figure 2.5). To minimize the effects of the growth material accumulating under the tip, we translate the tip at a constant rate (1 $\mu m\ s^{-1}$) while writing germanium lines on the sample. The onset voltage for writing occurs at 8 ± 2 V and typically corresponds with the onset of the field emission current, but varies more widely than the latter. We attribute the somewhat large variability of the writing onset to the disparity in tip radius of curvature and tip shape. SEM investigation before and after writing suggests that the tip changes shape continuously during writing, thus affecting its field emission properties. It is interesting to note that high-quality patterns with relatively small line edge roughness can be produced by a somewhat blunt and irregular tip. After onset, the germanium lines grow wider and taller with increasing voltage up to *ca.* 20 V positive on the sample. Above 20 V, the deposition becomes erratic and microscopic irregular features are often observed. These appear to be caused by small explosive discharges occurring near the tip-sample interface.[19] To minimize tip convolution effects, the images were recorded in air in tapping mode with a new tip ($r < 10$nm).

For regular deposition, line width starts at 40 nm (8 V) and reaches a maximum width of *ca.* 80 nm (19 V). The feature height follows a similar trend starting at 0.5 nm for deposition occurring at 8 V and reaching its maximum of 3.5 nm for deposition occurring at 19 V. The height increases by sevenfold from the minimum to the maximum voltage, the width only increases by twofold. This anisotropic growth trend may be caused by the direction and gradient of the electric field that likely directs the deposition of the reactive species. Another factor to be considered is that the maximum width of the DPG meniscus likely laterally confines the reaction.[31]

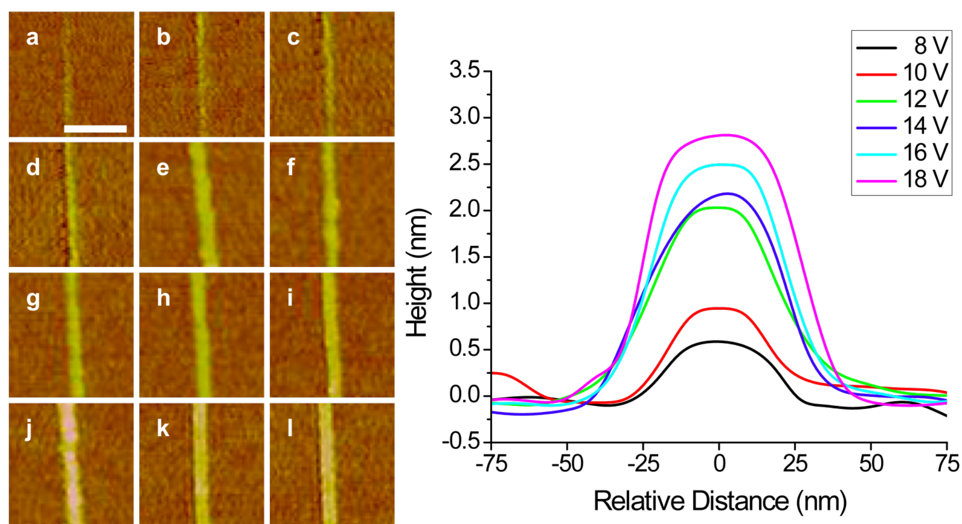

Figure 2.5 (left) Tapping mode AFM images of Germanium nanostructures written at 8 through 19 V respectively at 1 μm sec^{-1}. Scale bar is 250 nm. Height scale from dark brown to light yellow 10 nm. (right) Cross-sections of the germanium features. For clarity, only the plots at even voltage are shown for clarity.

Current was also collected during writing at different voltages. Data was collected at multiple times during the writing process for each voltage and averaged. Three such sets were collected and averaged. The error in the current value is a product of propagation of the error in the measurement (estimated as the noise peak to peak value during writing) as well as the standard deviation of the three measurements (Figure 2.6). The overall data is in good agreement with the IV curve presented in Figure 2.2 as well as the simulation at low voltages, but diverges (is lower) at higher voltages. Continuous change of tip shape during writing is likely responsible for these discrepancies at higher voltages.

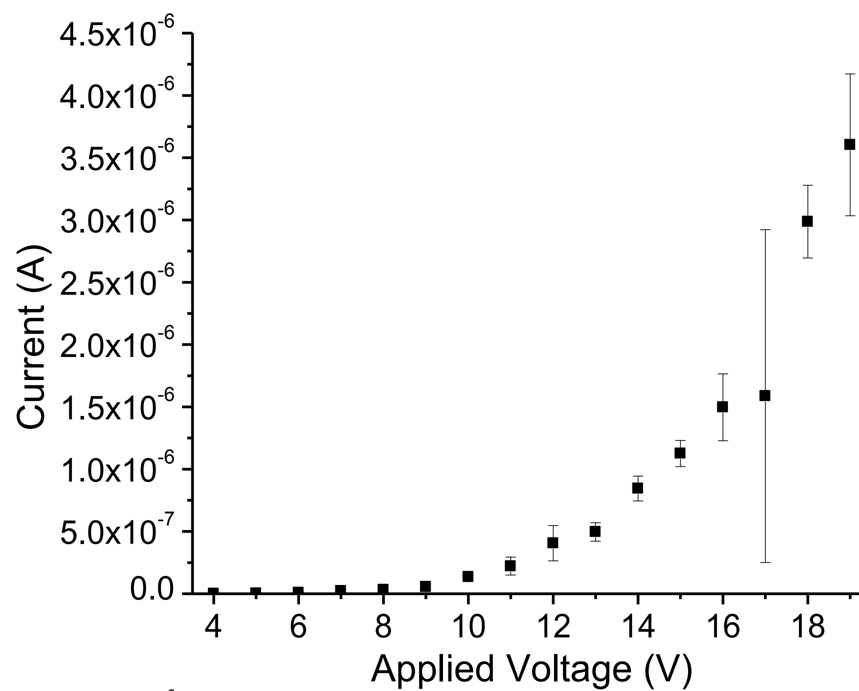

Figure 2.6. Plot of current as a function of applied voltage acquired during writing.

To estimate the reaction rate, we measure the average volume of germanium deposited per second as a function of voltage (Figure 2.7a). We estimate the number of germanium atoms deposited per second as $N_{Ge\ atoms} = \frac{Volume\ per\ second_{Ge} * \rho_{Ge}}{A_{r\ Ge}} * N_A$ where ρ_{ge} is the density of germanium (5.32 g cm^{-3}), N_A is Avogadro's number (6.02 x 10^{23}), and A_{rGe} is the molecular weight of germanium (72.64 g mol^{-1}). The number of electrons emitted per second was derived by $N_e = \frac{I}{e}$ where I is the current and e is equal to the charge of an electron (1.6 x 10^{9} C). The volume of the lines was calculated using the measured height multiplied by the measured width and length.

With increased voltage, more material is deposited per unit time. This trend has also been observed for high-field deposition of carbon from CO_2.[25] However, the volume of material deposited does not increase as fast as the field emitted current that is measured during writing. To further investigate this phenomenon, we calculate the inverse of the number of electrons required to react a DPG molecule and yield a germanium atom (Figure 2.7b). This value is an estimate of the reaction efficiency as a function of average electron energy.

This is an estimate of the reaction efficiency as a function of average electron energy. From these this data it is clear that most electrons cross the tip-sample interface without leading to the dissociation and deposition of a DPG molecule. This is a confirmation that the reaction occurring at the tip-sample interface is not purely electrochemical in nature, where one would expect a one-to-one correlation of electrons to reacted molecules. A significantly less efficient electron attachment process is involved in this reaction. At higher voltage bias (higher electron energy), reaction efficiency is decreased. This attachment process was already observed in the formation of TNIs during the reaction of silane precursors using

STM. However, in the STM work,[27] where the tip is further away from the surface, the electric field is too small[15] to be responsible for direct field- induced dissociation of the silane. In this work, the electric field is above the reaction threshold[27] and likely plays a role in the dissociation of the TNIs to yield the desired product.

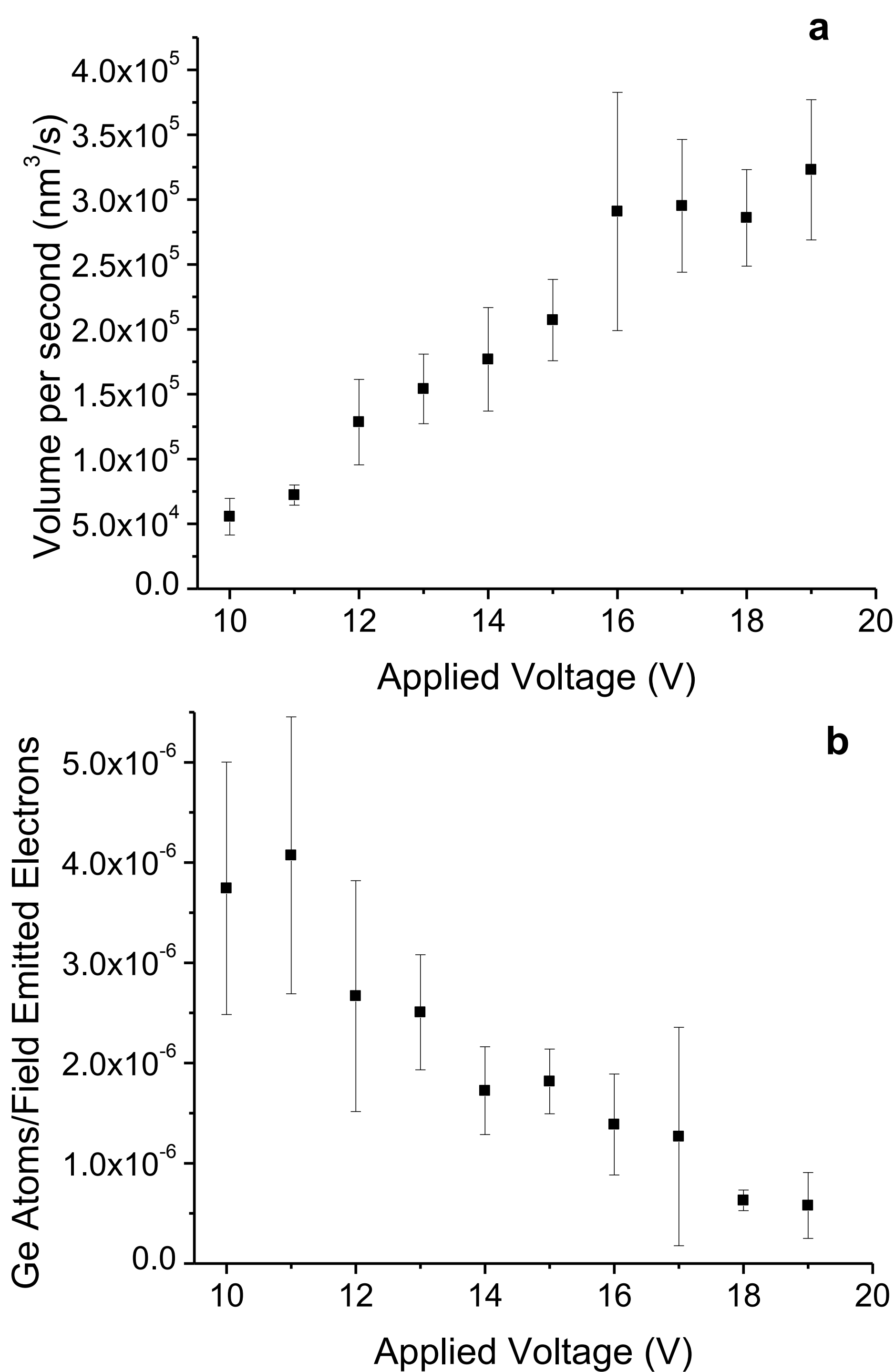

Figure 2.7 a) Germanium volume write rate as a function of tip-sample bias, b) Plot of the number of germanium atoms deposited per field emitted electrons (reaction efficiency) as a function of voltage. Data for voltages lower than 10 where not all series resulted in deposited germanium are omitted for clarity.

2.4 Conclusions

In conclusion, we have experimentally investigated and modeled via simulations the mechanisms of Ge nanostructure growth by the high-field reaction of diphenylgermane. We propose a model that involves electron field emission from the tip, followed by electron attachment with formation of temporary negative ions and high field fragmentation. We thus confirm that the reaction of the diphenylgermane precursor at the tip-sample interface is neither purely electrochemical in nature nor purely high-field activated and follows the same trends as the previously reported carbon deposition from organic precursors. This work contributes to the understanding of the possible reactions occurring at the tip-sample interface and can be used to expand the scope of this technique. Examples include using different organometallic precursors for the direct-write of a broad variety of materials.

2.5 References

1 Vasko, S. E. *et al.* Insights into the high field chemistry of diphenylgermane. *Physical Chemistry Chemical Physics* **13**, 4842-4845 (2011).

2 Garcia, R., Martinez, R. V. & Martinez, J. Nano-chemistry and scanning probe nanolithographies. *Chemical Society Reviews* **35**, 29-38 (2006).

3 Ginger, D. S., Zhang, H. & Mirkin, C. A. The evolution of dip-pen nanolithography. *Angewandte Chemie-International Edition* **43**, 30-45 (2004).

4 Gotsman, B., Duerig, U., Frommer, J. & Hawker, C. J. Exploiting Chemical Switching in a Diels-Alder Polymer for Nanoscale Probe Lithography and Data Storage. *Advanced Functional Materials* **16**, 1499-1505 (2006).

5 Long, D. A., Unal, K., Pratt, R. C., Malkoch, M. & Frommer, J. Localized "click" chemistry through dip-pen nanolithography. *Advanced Materials* **19**, 4471-4473 (2007).

6 Wei, Z. *et al.* Nanoscale Tunable Reduction of Graphene Oxide for Graphene Electronics. *Science* **328**, 1373-1376 (2008).

7 Fenwick, O. *et al.* Thermochemical nanopatterning of organic semiconductors. *Nature Nanotechnology* **4**, 664-668 (2009).

8 Knoll, A. W. *et al.* Probe-Based 3-D Nanolithography Using Self-Amplified Depolymerization Polymers. *Advanced Materials* **22**, 3361-3365.

9 Pires, D. *et al.* Nanoscale Three-Dimensional Patterning of Molecular Resists by Scanning Probes. *Science* **328**, 732-735, (2010).

10 Rolandi, M., Quate, C. F. & Dai, H. J. A new scanning probe lithography scheme with a novel metal resist. *Advanced Materials* **14**, 191-194 (2002).

11 Avouris, P., Hertel, T. & Martel, R. Atomic force microscope tip-induced local oxidation of silicon: Kinetics, mechanism, and nanofabrication. *Applied Physics Letters* **71**, 285-287 (1997).

12 Cen, C., Thiel, S., Mannhart, J. & Levy, J. Oxide Nanoelectronics on Demand. *Science* **323**, 1026-1030, doi:Doi 10.1126/Science.1168294 (2009).

13 Maoz, R., Frydman, E., Cohen, S. R. & Sagiv, J. "Constructive nanolithography": Inert monolayers as patternable templates for in-situ nanofabrication of metal-semiconductor-organic surface structures - A generic approach. *Advanced Materials* **12**, 725-+ (2000).

14 Unruh, D. A., Mauldin, C., Pastine, S. J., Rolandi, M. & FreÃÅchet, J. M. J. Bifunctional Patterning of Mixed Monolayer Surfaces Using Scanning Probe Lithography for Multiplexed Directed Assembly. *Journal of the American Chemical Society*, doi:10.1021/ja101627e.

15 Kreuzer, H. J. Physics and chemistry in high electric fields. *Surface and Interface Analysis* **36**, 372-379 (2004).

16 Fresco, Z. M., Suez, I., Backer, S. A. & Frechet, J. M. J. AFM-induced amine deprotection: Triggering localized bond cleavage by application of tip/substrate voltage bias for the surface self-assembly of nanosized dendritic objects. *Journal of the American Chemical Society* **126**, 8374-8375 (2004).

17 Fresco, Z. M. & Frechet, J. M. J. Selective surface activation of a functional monolayer for the fabrication of nanometer scale thiol patterns and directed self-assembly of gold nanoparticles. *Journal of the American Chemical Society* **127**, 8302-8303 (2005).

18 Backer, S. A., Suez, I., Fresco, Z. M., Rolandi, M. & Frechet, J. M. J. Covalent formation of nanoscale fullerene and dendrimer patterns. *Langmuir* **23**, 2297-2299, doi:Doi 10.1021/La0631973 (2007).

19 Xie, X. N. *et al.* Creating polymer structures of tunable electric functionality by nanoscale discharge-assisted cross-linking and oxygenation. *J Am Chem Soc* **128**, 2738-2744, doi:10.1021/ja0577241 (2006).

20 Germain, J., Rolandi, M., Backer, S. A. & Frechet, J. M. J. Sulfur as a Novel Nanopatterning Material: An Ultrathin Resist and a Chemically Addressable Template for Nanocrystal Self-Assembly. *Advanced Materials* **20**, 4526-4529, doi:Doi 10.1002/Adma.200802024 (2008).

21 Suez, I., Backer, S. A. & Frechet, J. M. J. Generating an etch resistant "resist" layer from common solvents using scanning probe lithography in a fluid cell. *Nano Letters* **5**, 321-324 (2005).

22 Suez, I. *et al.* High-field scanning probe lithography in hexadecane: Transitioning from field induced oxidation to solvent decomposition through surface modification. *Advanced Materials* **19**, 3570-+, doi:Doi 10.1002/Adma.200700716 (2007).

23 Martinez, R. V., Losilla, N. S., Martinez, J., Huttel, Y. & Garcia, R. Patterning polymeric structures with 2 nm resolution at 3 nm half pitch in ambient conditions. *Nano Letters* **7**, 1846-1850 (2007).

24 Rolandi, M., Suez, I., Scholl, A. & Frechet, J. M. J. Fluorocarbon resist for high-speed scanning probe lithography. *Angewandte Chemie-International Edition* **46**, 7477-7480 (2007).

25 Garcia, R. *et al.* Nanopatterning of carbonaceous structures by field-induced carbon dioxide splitting with a force microscope. *Applied Physics Letters* **96**, 143110:143111-143113 (2010).

26 Torrey, J. D. *et al.* Scanning Probe Direct-Write of Germanium Nanostructures. *Advanced Materials* **22**, 4639-4642 (2010).

27 Rauscher, H., Behrendt, F. & Behm, R. J. Fabrication of surface nanostructures by scanning tunneling microscope induced decomposition of SiH4 and SiH2Cl2. *J Vac Sci Technol B* **15**, 1373-1377 (1997).

28 Chockla, A. M. & Korgel, B. A. Seeded germanium nanowire synthesis in solution. *Journal of Materials Chemistry* **19**, 996-1001, doi:Doi 10.1039/B816954c (2009).

29 Virwani, K. R., Malshe, A. P. & Rajurkar, K. P. Understanding sub-20 nm breakdown behavior of liquid dielectrics. *Physical Review Letters* **99** (2007).

30 Henderson, W. & McIndoe, J. S. *Mass Spectrometry of Inorganic, Coordination, and Organometallic Compounds*. 47-54 (John Wiley & Sons, 2005).

31 Martinez, R. V. & Garcia, R. Nanolithography based on the formation and manipulation of nanometer-size organic liquid menisci. *Nano Letters* **5**, 1161-1164 (2005).

CHAPTER 3: Ge and Si Nanostructure AFM Direct Write

Abstract

After determining an initial model for the AFM direct write of diphenylgermane in Chapter 2, Chapter 3 presents a generalized reaction mechanism for group IVb DPX (X=Ge, Si) molecules. Using a combination of experimental methods (AFM, EI-MS) and simulations, the steps of the proposed reaction mechanism are investigated. In this reaction scheme, electrons tunnel from the tip into the precursor molecules, which initiates a chemical reaction that fragments the molecules.[2] The desired material is deposited on the substrate, while the majority of the carbon and hydrogen leave as benzene in the reaction volume.

3.1 Introduction

Scanning probe-based techniques offer a novel solution to studying localized chemistry on the nanoscale. Due to their ability to apply a localized stimulus or reactant to a spatially confined area, scanning probes have been used to study chemistry for applications from lithography to catalysis.[1] Additionally, much focus on the past twenty years has been on the use of electric fields in conjunction with scanning probe lithography. External electric fields (EEFs) above a certain threshold (ca ~V/Å) can induce the rearrangement of electronic orbitals in atoms and molecules, inducing field-assisted chemical reactions.[2] The spatial confinement offered by scanning probe lithography offers a way to access electric fields of this magnitude on the nanoscale. SPL techniques using electric fields as a stimulus include electron-field induced transfer of tip coatings to a surface[3,4], electrochemical deposition from precursor solutions,[5] and electrochemical dip-pen nanolithography.[6,7] Electric fields have also been used in conjunction with scanning probe microscopy to locally oxidize Si,[8] form carbonaceous deposits and etch

resists,[9-12] and recently, to direct write fabricate inorganic nanostructures using a biased AFM tip.[13,14]

The AFM direct write process uses low energy field emitted electrons to drive chemical reactions. A variety of techniques, including STM-induced CVD[15,16] and electron beam induced deposition (EBID)[17,18] also use low energy electrons to induce the deposition of inorganic nanostructures from inorganic precursors. In these two techniques, the precursor is normally in the gaseous form. While researchers have developed an understanding of silicon oxidation kinetics[15] and have recently posited models for carbonaceous deposition from the gas phase,[16,17] an initial model for the direct write of inorganic nanostructures has only recently been suggested.[18]

3.2 Developing an AFM Direct Write Model for Inorganic Precursors of the Form DPX

In this chapter, we attempt to further understand fundamental processes occurring in the high-field reaction of $C_{12}H_{12}X$ (X=Ge, Si). In brief, a biased AFM tip traces desired shapes along the silicon sample while a meniscus is condensed via saturated precursor vapor at the tip-sample interface (Figure 3.1a).[18] This experiment can also be performed while the silicon sample and AFM tip are immersed in the liquid precursor.[13,14] Due to tip-sample proximity, even a moderate 10 V bias induces an electric field with peak values above 10^9 V m^{-1} near the tip-sample interface (Figure 3.1b). High-field reactions of diphenylgermane (DPG) and diphenylsilane (DPS) via AFM demonstrate the direct-write of silicon and germanium nanostructures; and have been further adapted to conductive stamping of Ge and Si features.[14] We have previously proposed a model for high field direct write wherein an electron tunnels from the AFM tip into the precursor molecule, forming a temporary negative ion (TNI). The TNI subsequently fragments into organic byproducts, which dissolve back into the reaction

volume, and the desired inorganic species. In this article, we expand our model and verify the reaction sequence through a combination of experimental data and computer simulation. By working with diphenylgermane and diphenylsilane, we can directly probe the effect of inorganic species on the high field electrochemical reaction between the tip and the sample.

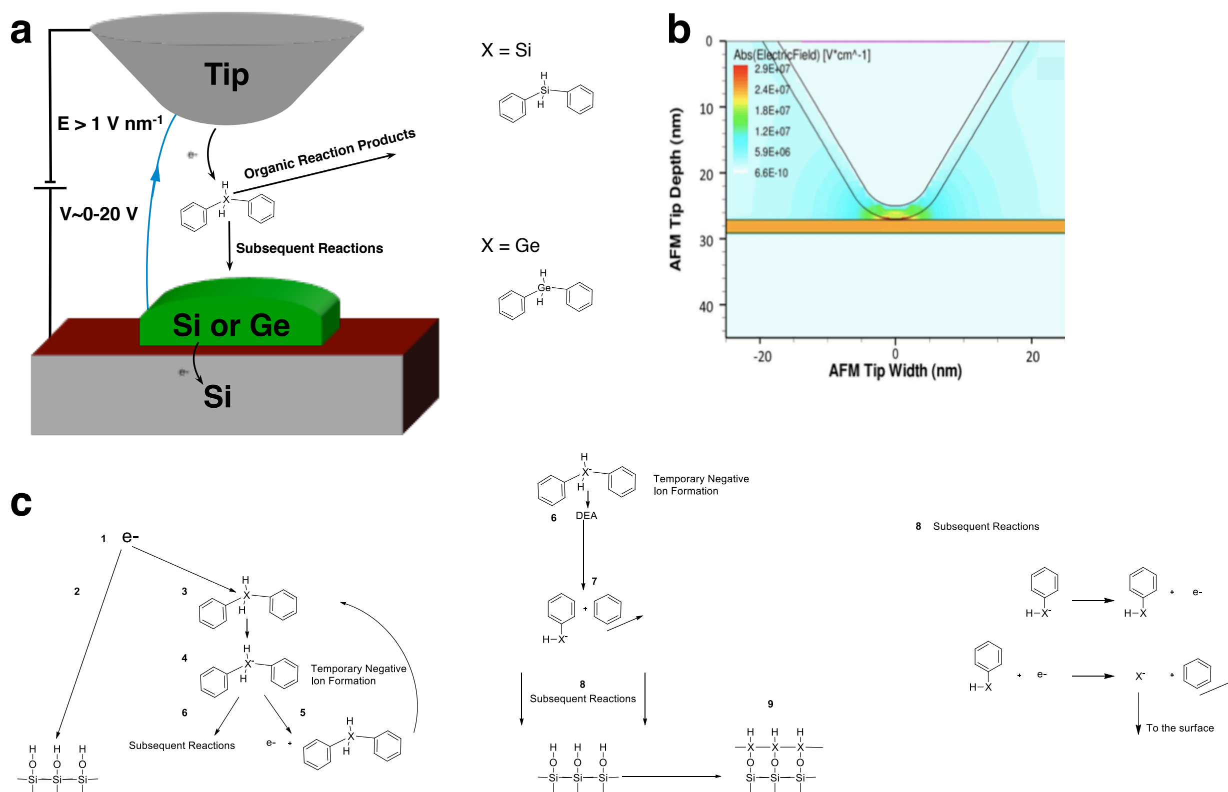

Figure 3.1 (a) Schematic of the probe sample geometry and deposition process for AFM direct-write. A moderate sample bias (~0-20V) induces a large electric field (>10^9 V m^{-1}/ >1V nm^{-1}). Electrons tunnel from the tip into the precursor molecule, where X = Ge or Si (b), and cause the fragmentation of the precursor and deposition of the desired product. (b) Electric field simulation for the AFM direct write process. (c) Generalized diagram of DPX breakdown pathways in the tip-sample gap. Electrons are field-emitted from the AFM tip (c1) and can either tunnel through the oxide into the Si wafer (c2) or into a DPX molecule (c3), forming a TNI (c4). The TNI can undergo autodetachment of the electron (c5) or fragment via one of several dissociative electron attachment pathways (c6,7). One the TNI has undergone fragmentation; it will undergo further reactions (c8), ultimately leading to the nanostructure formation (c9). Any of the charged particles will experience field-diffusion in the localized electric field (c).

The first step of our proposed reaction pathway is the field emission of an electron from the AFM tip via Fowler-Nordheim tunneling (Figure 3.1 Step 1). Previous calculations on the reaction efficiency as a function of average electron energy indicate that most of the emitted electrons cross the tip-sample interface without inducing the dissociation of a DPG molecule.[18] This indicates that the most probable electron pathway does not lead to a deposition event. One way that this occurs is when the electron directly tunnels from the tip, though the oxide layers of the tip and substrate, and to the underlying silicon wafer (Figure 3.1c Step 2). However, the electron can also tunnel from the tip through the tip oxide into the LUMO on the precursor molecule, forming a temporary negative ion (TNI) (Figure 3.1c Step 3). In AFM direct write of inorganic nanostructures, the precursor is treated as a conductive liquid, so instead of tunneling into the LUMO of the molecule, the electron tunnels into the conduction band.

The TNI can be formed in before the precursor molecule reaches the surface or can be formed after the molecule has reached the surface. The localized electric field at the tip apex (Figure 3.1b) can induce field diffusion of the TNI or subsequent charged fragments. This produces a feedstock for the reaction to occur by replenishing molecules in the tip-sample interface. Field-induced diffusion can cause the TNI to experience a change in electric field between initial TNI formation and subsequent breakdown steps. However, unlike STM-CVD, where field-induced diffusion plays a large role in deposition,[19] field-induced accumulation plays a much smaller role in AFM based lithography because the liquid precursor is already tightly packed in proximity to the tip-sample gap.

To determine the precursor dependence of the tunneling process, the energy levels of the precursors were determined through a combination of experiments and literature values. In the Fowler-Nordheim tunneling process (Figure 3.2a), the conduction band and bending of the tip

oxide do not depend on the precursor. The barrier between the Si of the AFM tip and the native oxide layer coating it becomes distorted from a rectangular barrier to a triangular barrier. With enough distortion, the barrier becomes thin enough for the Si electrons to tunnel through the oxide. The conduction band of the precursor liquid determines the voltage at which tunneling will occur between the Si AFM tip, oxide, and precursor molecule. The conduction band must be sufficiently energetically lower than the Fermi level of the AFM tip Si. In order to determine the relative position of the conduction band with respect to the vacuum level, we have estimated the electron affinity of each precursor through a combination of experimental measurements and literature values of ionization potential (Figure 3.2b). While ionization potential (IP) is a measurement of the amount of energy needed to remove an electron from the valence band, electron affinity (EA) is a measurement of the energy required to add an electron to the conduction band. The additional electron would be added to the conduction band; therefore, EA provides a direct measurement of the distance between the conduction band and the vacuum level. UV-Vis spectroscopy was performed to obtain the band gap energy of the two precursor molecules in the liquid phase (Figure 3.3). The UV-Vis spectra for DPS is an agreement with previously published data.[20] For optical band gap measurements, DPG and DPS were treated as conducting liquids. The optical band gap of a material can be estimated using the inflection point of the UV-Vis absorption spectrum. The linear portion of the UV-Vis were fit and the x-intercept, or inflection point) was determined. The literature value of the gas phase ionization potential for DPS is 9.23 eV.[21] Data for the IP of DPG does not exist in the literature. However, the IP of triphenylgermane and triphenylsilane are equal.[21] From this information we estimate the IP of DPG to be comparable to that of DPS. Using band gap data in conjunction with an exciton binding energy correction (0.1-1 eV) and the literature IP value, the EA is determined to

be 3.9-4.8 ±0.3eV for DPS and 4.0-4.9 ±0.2 for DPG. From these calculations, the conduction band of DPG may be lower versus vacuum than the conduction band of DPS. The conduction band of DPG might then contribute to a lower onset voltage for tunneling into the DPG than tunneling into the DPS (Figure 3.2a).

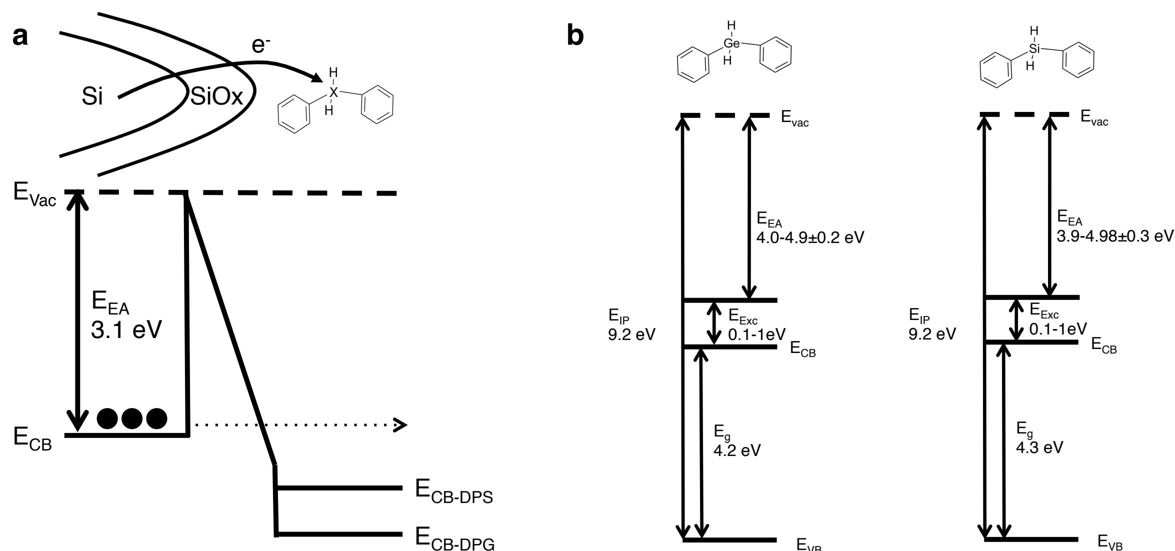

Figure 3.2 (a) Fowler-Nordheim tunneling process schematic. The applied electric field lowers the barrier for an electron (black circles) in the Si to tunnel through the potential barrier of the oxide. In our proposed model, the field-emitted electron tunnels into the conduction band of the DPX molecule. Because the conduction band of DPG is lower in energy than that of DPS, the onset voltage for tunneling is expected to be lower. (b) Band diagram for diphenylsilane (right) and diphenylgermane (left). The optical band gap was determined using UV-Vis spectroscopy. An exciton binding energy correction of 0.1-1 eV. Is employed as well. From a combination of literature and experimental values, we have determined the ionization potential (IP) and electron affinity (EA) of each molecule.

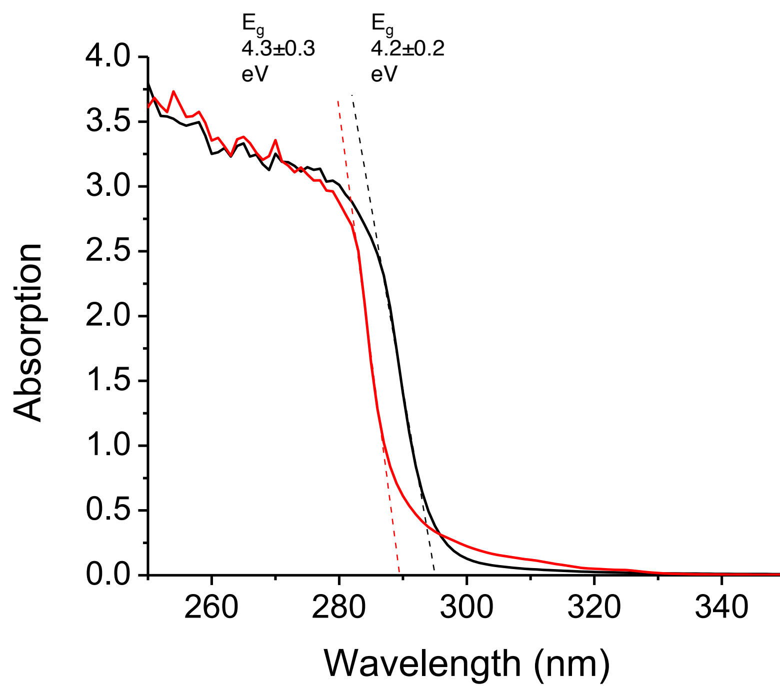

Figure 3.3 UV-vis spectra diphenylgermane (black) and diphenylsilane (red) with linear trend lines (dashed black = DPG, dashed red = DPS)

To test the tunneling step and the predicted difference in onset voltage for DPG and DPS, current was measured across the tip-sample interface with a stationary tip and a function of applied voltage (Figure 3.4). From this data, the corresponding onset voltage for diphenylgermane is 7±2 V, while the onset voltage for diphenylsilane molecule is 9±2 V (Fig. 3.4). The difference in onset voltages indicates that higher energy may be need for TNI formation with the DPS molecule. The observed difference in onset voltages is larger than that predicted by the difference in electron affinity between DPG and DPS.

To further understand the writing process for different precursors, we have produced features with different bias voltages (Fig. 3.5). To minimize the effects of the growth material accumulating under the tip, we translate the tip at a constant rate (1 μm sec^{-1}) while writing lines on the sample. To minimize tip convolution effects, the images were recorded in air in tapping mode with a new tip (r~10 nm). This writing study was performed at voltages within the threshold range, but below voltages that contribute to irregular features and small explosive discharges.[18,22] As expected, for each precursor, the heights and width increase with applied voltage. Deposited volume as a function of time was calculated as a function of height, width, and write speed. For voltages near the onset writing voltages, small differences between the deposited volume are observed. Above ~12V, the deposited volume of the precursors becomes comparable, indicating that higher applied voltages, the breakdown pathway becomes similar. As higher voltages are applied, the barrier to Fowler-Nordheim tunneling becomes thinner and tunneling into either DPG or DPS is then favorable.

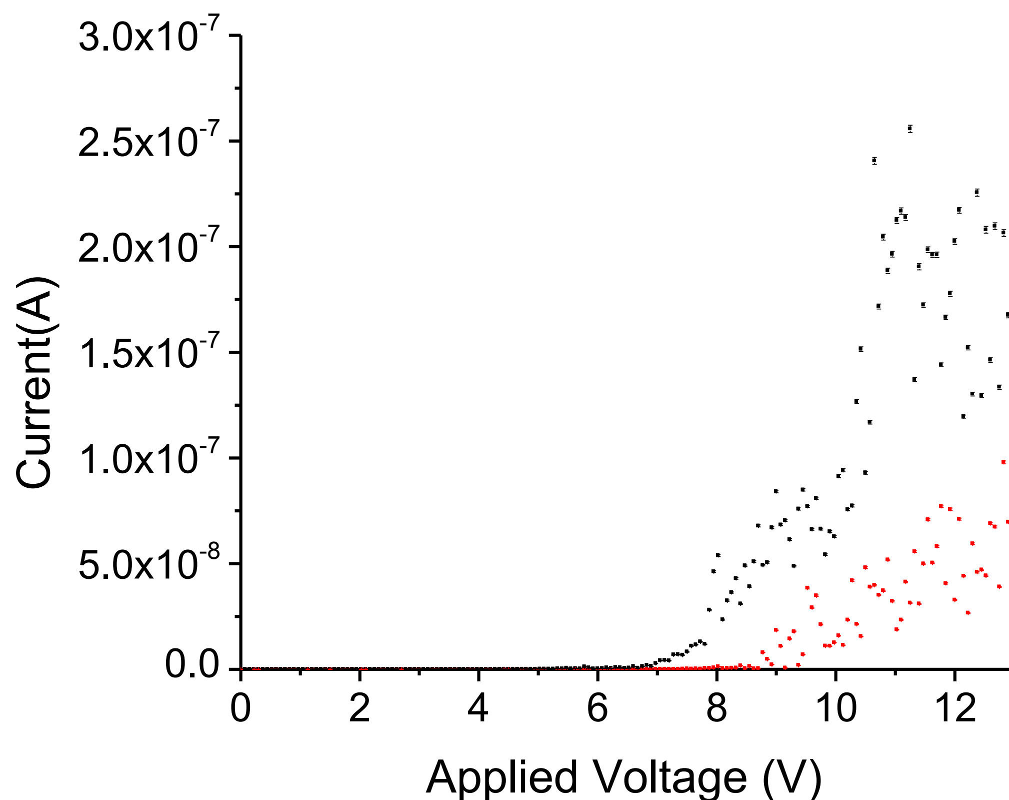

Figure 3.4 Current versus applied voltage (measured positive on the sample) obtained via an averaged I–V sweep with a stationary tip for diphenylgermane (black) and diphenylsilane (red) on an HMDS-treated surface. Current measurements were taken using a condensed meniscus of inorganic vapor at voltages near the onset voltage for DPG and DPS writing.

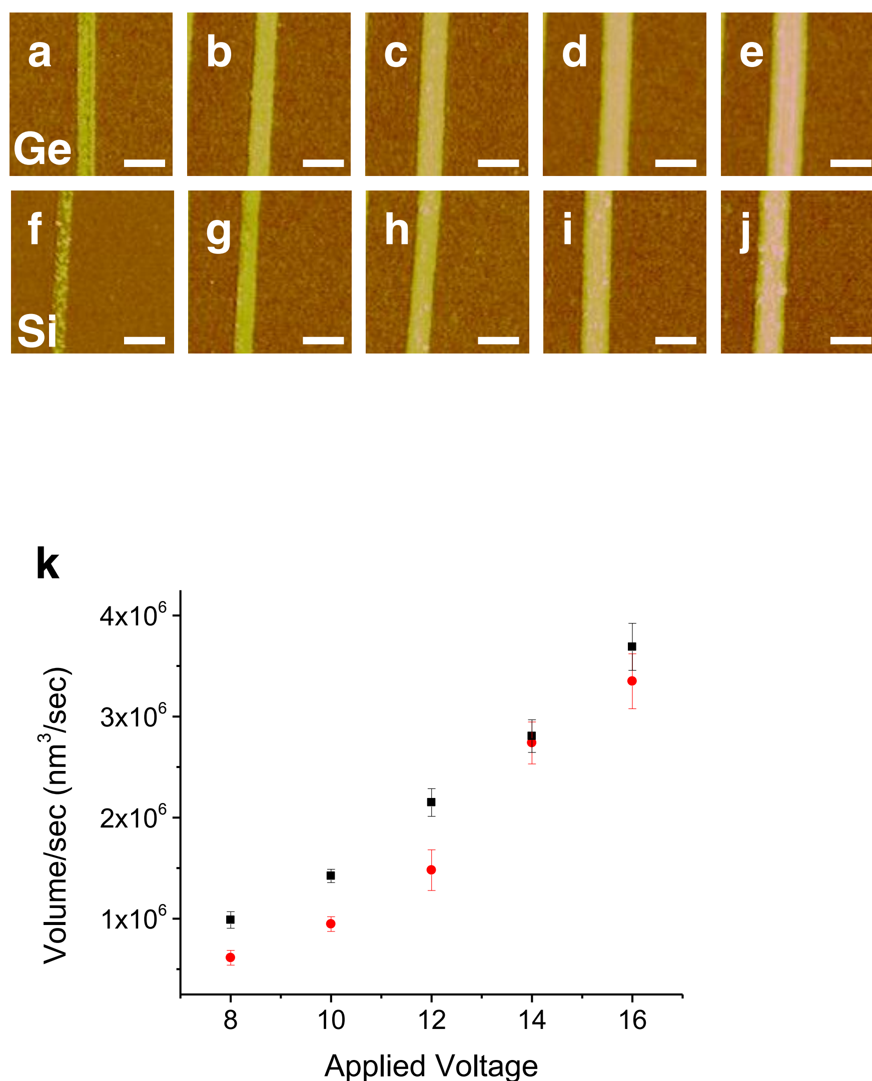

Figure 3.5 Comparison of lines fabricated from DPG and DPS (top and bottom) at applied voltages of 8 (a,f), 10 (b,g) , 12 (c,h), 14 (d,i), and 16 V (e, j) from L to R (a). Lines deposited at a write speed of 1 μm s^{-1}. Scale bar = 250 nm, height scale from brown to bright yellow = 10 nm. Comparison of volume of lines fabricated from DPG (black squares) and DPS (red circles) (k).

The next step in our proposed model is the fragmentation of the temporary negative ion into further reactants. TNIs can decay by multiple mechanisms: autoemission of the captured electron (Figure 3.1c Step 5) and dissociative electron attachment (DEA) (Figure 3.1c Step 6).[23] Like the direct tunneling from the AFM tip into the substrate, autoemission does not result in deposition. The autoemitted electron can either tunnel through the oxide to the Si or to interact with a subsequent molecule. The DPX molecule returns to the reaction feedstock where it can undergo further reactions with field emitted electrons. In dissociative electron attachment, the TNI decays into a negative charged and neutral fragments (Figure 3.1c Step 7).[23,24] The effect of timescale on the TNI decay processes was investigated using two different surface terminations: an evaporated metal layer on native oxide/Si and a native oxide Si layer. Performing direct write on metal surfaces did not reliably yield structures in the typical voltage range used for writing (0-20V). The presence of the surface oxide layer lengthens the time it would take the electron to tunnel from the tip to the Si substrate making it more likely that the TNI will breakdown before the electron dissociates from the molecule. On the metal surface, the tunneling rate is too fast for the temporary negative ion to dissociate in the short path length between the tip and the substrate. The tunneling rate through the oxide layer is sufficiently slow enough compared to the TNI fragmentation as to allow fragmentation.

After confirming electron tunneling into the precursor molecules, we then investigated the potential dissociative electron attachment routes of the TNI. Direct analysis of the reaction fragments is limited by the sub-attomolar quantities of precursor reacted during the direct write process. In order to understand potential breakdown pathways of these precursors, we use electron impact ionization mass spectroscopy (EI-MS) in an attempt at elucidating the reaction pathway on the macroscale.[18] In such an experimental set-up, a field equivalent to the one

present during AFM writing cannot be induced. In an effort to reproduce the AFM conditions, the electrons that would give a reasonable signal to noise ratio and be comparable with the deposition voltages were employed. Spectra were collected for DPG and DPS at 14 and 17 eV (Figure 3.6, 3.8).[1] While the eV from EI-MS does not necessarily match the voltage bias in the AFM experiment, these data can be used to provide a qualitative trend between electron energy and precursor reaction.

The analysis for the different acceleration voltages for these spectra focused on three areas: the molecular ion region, the region corresponding to the loss of one phenyl group, and the sub-100 m/z region. Sub-100 m/z peaks include the elemental fragment, benzene, and lower mass fragments. Germanium fragments exhibit an isotope pattern corresponding to the three naturally occurring isotopes at above 20% (70,72,74) and two others that appear in lesser percentage (73, 76), while silicon fragments exhibit only three isotopes, where one isotope (28) is more abundant than the other two isotopes (29, 30) combined.

For the molecular ion region at all acceleration voltages, the DPG and DPS spectra show molecular ion peaks, the isotope distribution of the inorganic element, and the isotope distribution of carbon. In addition, hydrogen losses from the phenyl groups are observed in the 17 and 70 eV spectra. In DPG, the isotopic distribution predicts the most abundant signal for the loss of one phenyl group to be at 158 m/z and predicts 106 m/z for DPS daughter ion. From the relative ratios of the daughter ions to the molecular ions, it is apparent that the diphenylgermane readily forms daughter ions. However, the relative ratio of daughter to parent ion in the diphenylsilane spectra is less, suggesting that reaction of DPS may be less energetically favorable than for DPG. In order to evaluate if the first reaction step is the loss of benzene or the

[1] During the analysis of the germanium spectra, it became apparent that contamination peaks occur at 79, 119, and 94.

loss of a hydrogen, we compared the relative ratio of the parent and daughter ions and also to the predicted peak for the loss of one hydrogen from the molecular ion. For DPG, the relative intensities are as follows: 230>158>229. The same trend is observed for DPS, with the relative intensity pattern of 183>106>184. Collision induced decay was also performed at 17 eV for both diphenylsilane and diphenylgermane (Fig. 3.7). Both of these CID spectra indicate that the fragmentation from the parent ion to the daughter ion occurs through the loss of a neutral benzene molecule. As a whole, the EI-MS spectra indicates that while both precursors decompose by loss of the phenyl groups, this process may be more energetically favorable for DPG then for DPS. Initial DFT and VASP calculations also indicate that the most energetically favorable fragmentation route from DPG with one electron is the loss of a neutral phenyl through cleaving one phenyl and one hydrogen bond.[18,25] This reaction could possibly proceed as a 1-step loss of both the hydrogen and phenyl or through the dissociation of the TNI into a phenyl radical which then abstracts a hydrogen from the parent molecule.

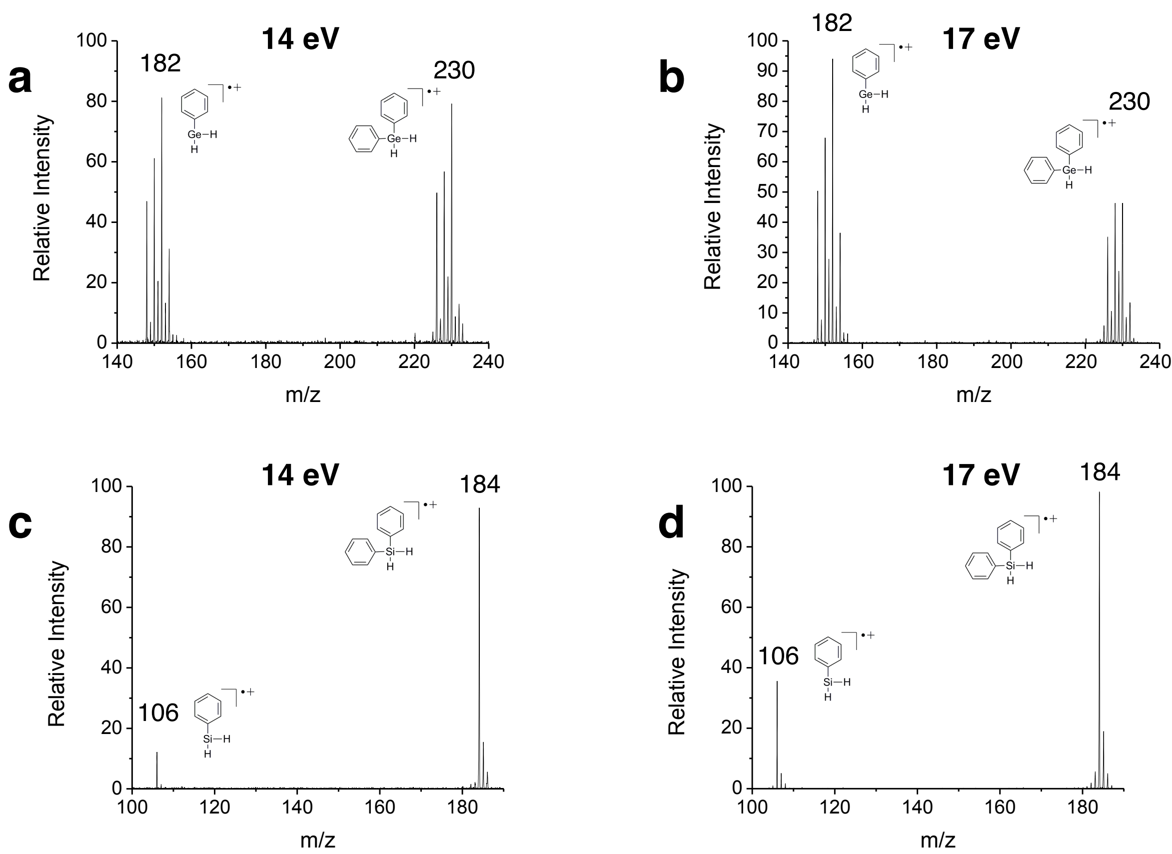

Figure 3.6 Electron Impact Mass Spectrometry data acquired from liquid diphenylgermane (top row) and diphenylsilane (bottom row) using 14 eV (a,c) and 17 eV (b,d) ionization electrons. The signature of molecular fragments of breakdown from the molecular ion to the molecular ion minus one phenyl is present for both DPG and DPS at 14 and 17 eV

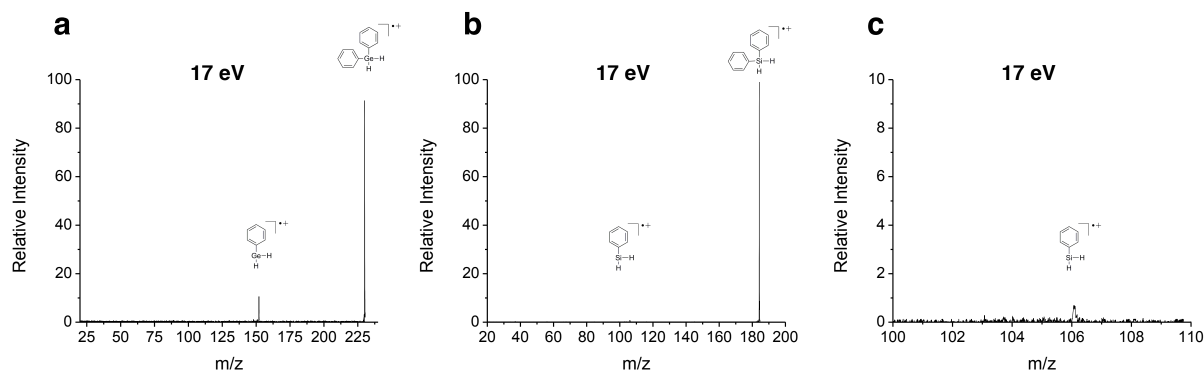

F**igure 3.7** Collision induced dissociation (CID) data acquired from liquid diphenylgermane (a) and diphenylsilane using 17 eV (b,c) ionization electrons. The molecular ion containing the most abundant isotope was chosen for DPG (230 amu) and DPS (184 amu). CID indicates that these molecular ions both fragment by losing one neutral phenyl.

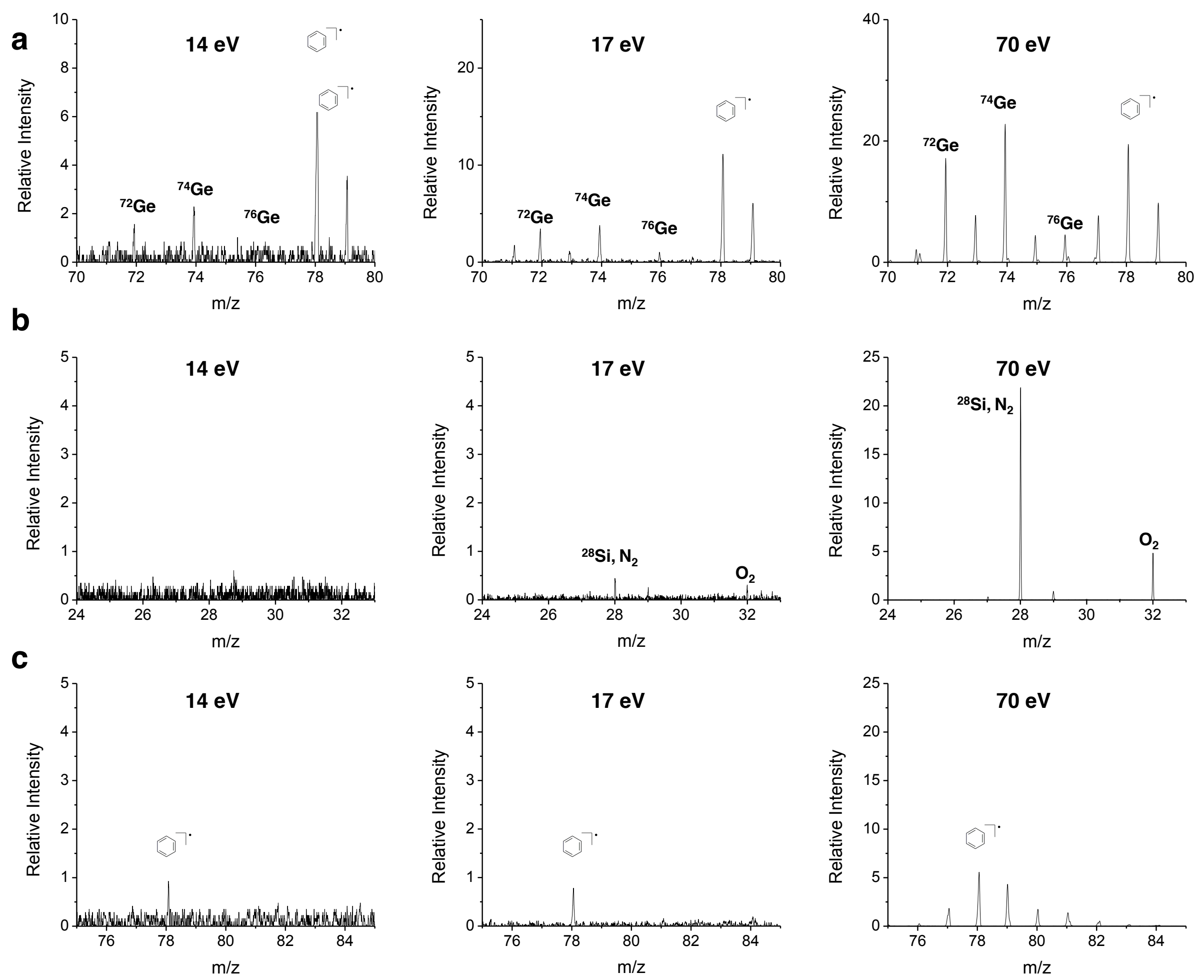

Figure 3.8 a) Diphenylgermane EI-MS for 14, 17, and 70 eV. The Ge isotope pattern is present in each of these spectra, as well as the benzene fragment signal. b) Diphenylsilane EI-MS for 14,17, and 70 eV for the Si fragment c) Diphenylsilane EI-MS at 14,17, and 70 eV for the benzene fragment signal

The differences in molecular ion to PhXH ion ratio may be explained by a difference in the Ge-C and Si-C bond strengths. Bond strengths are not available for these specific molecules, but a qualitative discussion about bond lengths- inversely proportional to bond strength can be used for a qualitative picture. The bond length for Ge-C in phenylgermane was determined to be 1.94 Å, while the bond length for Si-C in phenylgermane was determined to be 1.84 Å.[26] In tetraphenyl analogues, the mean bond length between the Ph and Ge was 1.95 Å, but 1.87 Å between Ph and Si.[27] As bond strength is inversely proportional to bond length, these bond lengths indicate that the Si-C(phenyl) bond is stronger than the Ge-C(phenyl) bond. In the previous calculations based on the Ph_4X species, the Ge-C bond in Ph_4Ge has a bond strength of 3.44±0.09 eV, compared to 3.21±0.03 eV for the Si-C bond in Ph_4Si.[28,29] For CH_3XH_3 compounds, Ge-C was calculated to be 3.16 eV vs 3.56 eV for the Si-C bond.[30] The trend observed in the literature is that the Ge-C bond is lower in energy than the Si-C bond. This trend suggests that both the degree of aryl substitution and the inorganic central atom play a role in the bond strength. The higher bond strength, in addition to low polarity, makes the Si-C bond both kinetically and thermodynamically stable.[31,32] Additionally, group IVB organometallic compounds contain vacant nd orbitals (3d for Si, 5d for Ge), which have energies close to the s and p-orbitals of the outer electron shell.[33] In phenylsilanes, the pi electrons of the benzene ring can donate electron density to the vacant 3d orbitals of Si.[34] It has been shown, at least in the case of triphenylgermane, that a germanium atom is less capable f a dπ-pπ interaction than Si.[33]

There are many subsequent fragmentation steps after the first TNI decay; gas phase DEA reactions can involve numerous and complex pathways to a final product.[35] For processes using an electron beam to decompose physisorbed $Pt(PF_3)_4$ to Pt, TNI followed by DEA is proposed for the first step, with several consecutive collisions needed to form Pt.[36] It is speculated that Pt^-

loses it's electron via losing the electron to the substrate or undergoing electron-induced detachment.[36] $C_6H_6X^-$ can undergo further reactions in the reaction volume before it reaches the surface or it can attach to the surface before undergoing subsequent reaction steps. While there are a myriad of reaction pathways for this fragment, we posit a pathway for these subsequent reactions is for $C_6H_6X^-$ to undergo autodetachment of the electron and then undergo TNI formation from a different field-emitted electron (Figure 3.1c Step 8). This TNI also fragments via losing a phenyl group, yielding Ge^- (Figure 3.1c Step 8). Following the first dissociation of the DPX TNI, the final fragment may also be achieved by subsequent collisions or electron-induced dissociation. In the final step of the proposed reaction pathway, the nanostructure itself is formed. Characterization of the final product has been previously performed via time-of-flight secondary ion mass spectrometry (ToF-SIMS) and photoemission electron microscopy resolved near edge x-ray absorption fine structure (PEEM-NEXAFS).[13,14] This data confirms that the structures fabricated in this technique primarily inorganic, with trace carbon contamination. Furthermore, these two techniques indicate that the high-field chemical reaction is localized, occurring only in in proximity to the tip sample interface.

We also explored alternative pathways for precursor breakdown. Direct ionization of the precursor molecule, yielding DPG^+ or DPS^+, is not favored. If this pathway were viable, material would accumulate on the tip during the writing process, which has not been observed. Additionally, if this pathway were viable, writing could be performed by applying a negative bias to the substrate, which is also not observed. Finally, a large contribution from room-temperature disproportiation can be ruled out as well. Previous long-term studies of diphenylgermane found changes in the index of refraction after four months. This change was attributed to disproportionation, oxidation, or a combination of both.[37] Furthermore,

tetraphenylgermane formation has been observed over time, leading more credence to the theory of RT disproportionation.[37] Any role played by disproportiation in the reaction pathway is limited due to the long timescale over which it occurs at RT.

3.3 Conclusions

In conclusion, we have experimentally investigated the differences in the high field direct write of DPS and DPG. We propose a model where an electron is field-emitted from an AFM tip, can tunnel into the DPX molecule, and form a temporary negative ion. The TNI can undergo autodetachment or fragment through dissociative electron attachment. Subsequent collisions and DEA reactions cause the formation of X nanostructures on the surface. The measured current for each precursors indicates that difference in the EA affinity of the X atom accounts for the difference in onset voltage and deposited volume at lower write voltages. From the current/voltage, volume/voltage, and mass spectroscopy data, we also postulate that the strength of the X-C for both DPS and DPS. This work provides the base to explore further precursor development, specifically the effect of the ligand on deposition, for a variety of exotic precursors, including the III-V and III-VI precursor families.

3.4 References

1 Yeung, K. L. & Yao, N. Scanning Probe Microscopy in Catalysis. *Journal of Nanoscience and Nanotechnology* **4**, 647-690 (2004).

2 Kreuzer, H. J. Physics and chemistry in high electric fields *Surface Science* **246**, 336-347 (1990).

3 Song, J. Q. *et al. Molecular Crystal Liquid Crystal Science and Technology Section A* **294-295**, 51 (1997).

4 Melo, L. V. & Brogueira, P. in *Materials Research Society Spring Meeting.* (Cambridge University Press).

5 Uosaki, K., Koinuma, M., Sekine, N. & Ye, S. in *Solid-Liquid Electrochemical Interfaces ACS Symposium Series* Ch. 14, 189-201 (American Cehmical Society, 1997).

6 Li, Y., Maynor, B. W. & Liu, J. Electrochemical AFM "Dip-Pen" Nanolithography. *Journal of American Chemical Society* **123**, 2105-2106 (2001).

7 Maynor, B. W., Li, Y. & Liu, J. Au "Ink" for AFM "Dip-Pen" Nanolithography. *Langmuir* **17**, 2575-2578 (2001).

8 Avouris, P., Hertel, T. & Martel, R. Atomic Force Microscope Tip-Induced Lodal Oxidation of Silicon: Kinetics, Mechanism, and Nanofabrication. *Applied Physics Letters* **71**, 285-287, doi:10.1063/1.119521 (1997).

9 Rolandi, M., Suez, I., Scholl, A. & Frechet, J. M. J. Fluorocarbon Resist for High-Speed Scanning Proble Lithography. *Angewandte Chemie-International Edition* **46**, 7477-7480 (2007).

10 Suez, I. *et al.* High-field scanning probe lithography in hexadecane: transitioning from field induced oxidation to solvent decomposition through surface modification. *Advanced Materials* **19**, 3570-3573 (2007).

11 Martinez, R. V. & Garcia, R. Nanolithography Based on the Formation and Manipulation of Nanometer-Size Organic Liquid Menisci. *Nano Letters* **5**, 1161-1164 (2005).

12 Martinez, R. V., Losilla, N. S., Martinez, J., Huttel, Y. & Garcia, R. Patterning polymeric structures with 2 nm resolution at 3 nm half pitch in ambient conditions. *Nano Letters* **7**, 1846-1850 (2007).

13 Torrey, J. D. *et al.* Scanning Probe Direct-Write of Germanium Nanostructures. *Advanced Materials* **22**, 4639-4642 (2010).

14 Vasko, S. E. *et al.* Serial and Parallel Si, Ge, and SiGe Direct Write with Scanning Probes and Conductive Stamps. *Nano Letters* **11**, 2386-2389 (2011).

15 Snow, E. S., Jernigan, G. G. & Campbell, P. M. The Kinetics and Mechanism of Scanned Probe Oxidation of Si. *Applied Physics Letters* **76**, 1782-1784 (2000).

16 Calvaresi, M. *et al.* Splitting CO2 with Electric Fields: A Computational Investigation. *Journal of Physical Chemistry Letters* **1**, 3256-3260 (2010).

17 Lee, J., Sorescu, D. C. & Deng, X. Electron-Induces Dissociation of CO2 on TiO2(110). *Journal of American Chemical Society* **133**, 10066-10069 (2011).

18 Vasko, S. E. *et al.* Insights into the high field chemistry of diphenylgermane. *Physical Chemistry Chemical Physics* **13**, 4842-4845 (2011).

19 Lyubinetsky, I., Mezhenny, S., Choyke, W. J. & Yates, J. T. Two Mechanism of Scanning Tunneling Microscope Assisted Nanostructure Formation Using Precursor Molecules. *Journal of Vacuum Science and Technology A* **17**, 1445-1450 (1999).

20 Lang, L. *Absorption Spectra in the Ultraviolet and Visible Region*. Vol. 9 (Academic Press, 1967).

21 Distefano, G., Fignataro, S., Szepes, L. & Borossay, J. Photoelectron Spectroscopy Study of the Triphenyl Derivatives of the Group IV Elements. *Journal of Organometallic Chemistry* **104**, 173-178 (1976).

22 Xie, X. N. *et al.* Creating Polymer Structures of Tunable Electric Functionality by Nanoscale Discharge-Assisted Cross-Linking and Oxygenation. *Journal of the American Chemical Society* **128**, 2738-2744 (2006).

23 Oster, T., Kunh, A. & Illenberger, E. Gas Phase Negative Ion Chemistry. *International Journal of Mass Spectrometry and Ion Processes* **89**, 1-72 (1989).

24 Rauscher, H., Behrendt, F. & Behm, R. J. Fabrication of surface nanostructures by scanning tunneling microscope induced decomposition of SiH4 and SiH2Cl2. *Journal of Vacuum Science & Technology B* **15**, 1373-1377 (1997).

25 Vasko, S. E. *et al.* (2012).

26 Fleming, J. W. & Banwell, C. N. Internal Rotation in Phenylsilane and Phenylgermane and their -D3 derivatives. *Journal of Molecular Spectroscopy* **31**, 318-340 (1969).

27 Mackay, K. M. *The Chemistry of Organic Germanium, Tin, and Lead Compounds*. (John Wiley & Sons, 1995).

28 Calle, L. M. & Kana'an, A. S. Enthalpies and entropies of sublimation of tetraphenylsilane and hexaphenyldisilane. The bond dissociation energies of Si-C and Si-Si. *Journal of Chemical Thermodynamics* **6**, 935-942 (1974).

29 Kana'an, A. S. Enthalpies and entropies of sublimation of germanium tetraphenyl and di-germanium hexaphenyl. The bond dissociation energy of Ge-C and Ge-Ge. *Journal of Chemical Thermodynamics* **6**, 191-199 (1974).

30 Mui, C., Bent, S. F. & Musgrave, C. B. A Theoretical Study of the Structure and Thermochemistry of 1,3-Butadiene on the Ge/Si(100)-2x1 Surface. *Journal of Physical Chemistry A* **104**, 2457-2462 (2000).

31 Buriak, J. M. Organometalic Chemistry on Silicon Germanium Surfaces. *Chemical Reviews* **102**, 1271-1308 (2002).

32 Brook, M. A. *Silicon in Organic, Organometallic, and Polymer Chemistry*. (John Wiley & Sons, 2000).

33 Egorochkin, A. N. *et al.* Frequencies of Ge-H Stretching Modes and the Effect of dπ -pπ Interaction in Organogermanium Compounds. *Journal of Organometallic Chemistry* **76**, 29-36 (1974).

34 Freeburger, M. E. & Spialter, L. Physical Organosilicon Chemistry. I. Nuclear Magnetic Resonance Studies of Ortho-, Meta-, and Para-Substituted Phenyltrimethylsilanes. Evidence Bearing on the Existence of $(p \rightarrow d)\ \pi$ "Back-Bonding" in Phenylsilanes. *Journal of the American Chemical Society* **93**, 1894-1898 (1971).

35 Gohlke, S., Rosa, A., Illenberger, E., Bruning, F. & Huels, M. A. Formation of Anion Fragments from Gas-Phase Glycine by Low Energy (0-15 eV) Electron Impact. *Journal of Chemical Physics* **116**, 10164-10169 (2002).

36 May, O., Kubala, D. & Allan, M. Dissociative Electron Attachment to Pt(PF3)4-A Precursor for Focused Electron Beam Induced Processing (FEBIP). *Physical Chemistry Chemical Physics* **14**, 2979-2982 (2012).

37 Johnson, O. H. & Harris, D. M. Diphenylgermane and dihalodiphenylgermane. *Journal of American Chemical Society* **75**, 5564-5566 (1950).

CHAPTER 4: Germanium Nanostructure Fabrication via AFM Direct Write

Abstract

We have developed an approach to semiconductor nanostructure direct-write using tip of an atomic force microscope (AFM) to control the size, shape, and composition of semiconductor nanostructures.[1-3] In our scheme, the biased probe of an AFM reacts diphenylgermane to create diphenylgermane nanofeartures. Sub-30 nm features are written in arbitrary patterns at velocities as high as 100 μm s^{-1}. Nanostructures fabricated from direct write are characterized using SIMS and x-ray PEEM.

4.1 Introduction

As mentioned in the introduction, AFM-based high field lithography has previously been limited to the deposition of carbonaceous deposits from organic solvents and etch resists. In this chapter, I present the first efforts to deposit inorganic nanostructures via AFM direct write. Using a commercially available inorganic precursor, diphenylgermane, the fabrication of germanium nanostructures in user-defined patterns is demonstrated. Germanium nanostructures are appealing for a variety of electronic and optical applications due to the fact that Ge has a lower bandgap than Si[1] (0.67 vs 1.1 eV) and a higher carrier mobility.[2] While this chapter presents the lab-scale fabrication of Ge nanostructures, efforts towards upscaling will be introduced in the next chapter.

Additionally, characterization strategies for nanostructures fabricated through the high field AFM lithography method are presented. The germanium nanostructures are analyzed for germanium and carbon content using time-of-flight secondary ion mass spectroscopy (ToF-SIMS) and x-ray photoemission electron microscopy (PEEM) are fabricated. The minimal carbon content in these features supports the reaction pathway explored in Chapter II and III. In

the proposed pathway, a temporary negative ion (TNI) is formed from the precursor and a field emitted electron. This TNI subsequent fragments into germanium and phenyl groups. Through additional experiments on the solubility and annealing behavior of the structures, we demonstrate that the nanostructures are Ge-based and contain, at most, trace amounts of oxygen or carbon.

This chapter is presented in a similar form as it was published in *Advanced Materials* Reprinted with permission from Torrey, J.D., Vasko, S. E. *et al.* Scanning Probe Direct-Write of Germanium Nanostructures. *Advanced Materials* **22**, 4639-4642 (2010). (http://onlinelibrary.wiley.com/doi/10.1002/adma.201001987/abstract). Copyright 2010 John Wiley & Sons. This chapter also includes an expanded discussion on characterization techniques, including strategies for approximating the carbon content of inorganic nanostructures fabricated using AFM direct write.

4.2 Scanning Probe Direct Write of Germanium Nanostructures

The integration of dissimilar materials with nanoscale accuracy is a challenging pursuit essential for novel advances in electronics[3] and photonics.[4] Traditional nanofabrication strategies for materials integration often involve multiple lithography and alignment steps or complex wafer bonding procedures.[5] Scanning probes have emerged as attractive tools for nanofabrication in light of their ability to locally deliver desired stimuli[6] or chemicals to a small area of the sample surface.[7] Specifically, the atomic force microscope (AFM) has been employed in several nanofabrication schemes, including anodic oxidation,[8-10] nanoscale etching,[11,12] local conductivity switching,[13] nanoscale polymerization,[14,15] thermochemical lithography,[16-19] and monolayer activation for the directed assembly of nano-objects.[20-23] For materials integration, AFM direct-write methods such as dip-pen nanolithography,[7,24] or high-field lithography[25-27] afford nanometer placement of desired chemical or biological species, as well as solid-state

nanostructures.[25-28] For solid-state nanostructures, high-field lithography is a true one-step scheme because the desired material is locally synthesized during writing and post-patterning processing is not required.[25-28] Furthermore, high-field lithography has demonstrated unparalleled 1 cm s^{-1} write velocities[29] as well as 2 nm-resolution for fluorocarbon and carbon direct write respectively.[30] However, until now this technique has been limited to writing carbon-based nanostructures that can be used as etch resists, but do not add any other material functionality to the silicon substrate.

In this chapter, a novel AFM strategy that writes sub-30 nm germanium nanostructures with deterministic size and placement control is presented. In brief, an AFM tip traces desired shapes along the biased silicon sample while immersed in diphenylgermane (DPG). The proximity of the scanning probe to the biased sample generates an intense (> 10^9 V m^{-1}) electric field that reacts the desired precursor. In tapping mode, the electric field is generated across the nanometer tip-sample gap that is maintained with the microscope feedback. [25-28] In contact mode, the high electric field is induced in close proximity to the contact point. In this proximity, the tip and sample surfaces are not touching and are at nanometer separation.[29] These surfaces are at different potential during patterning because most of the potential drop along the tip-sample circuit occurs across the high-resistance contact point (only a few atoms) when the patterning current flows. This high electric field injects electrons from the tip into the precursor and fragments the charged precursor to write Ge nanostructures onto the substrate (Figure 4.1 and Figure 4.2). It is theorized that the other DPG constituents leave the reaction volume either as benzene or charged organic fragments that dissolve into the liquid. In our strategy, nanostructure direct write is confined to the region of the sample defined by the electric field induced from the tip and can be modulated by turning on and off the bias.

4.3 Ge Direct Write from DPG

Using the method described in Section 4.2, arbitrary shapes of 3 nm tall and 80 nm wide Ge nanostructures are routinely produced at a rate of 1 μm s^{-1} (Figure 4.2a). Increasing write speed to 100 μm s^{-1} grows thinner nanostructures (0.7 nm) as narrow as 25 ± 2 nm (FWHM) (Figure 4.2b and Figure 4.2c, Figure 4.3). Line widths are limited by the tip radius and directly related to write speed and bias, with slower write speeds and higher bias generally producing wider and taller lines (Figure 4.2d). The nanostructure geometry can be precisely determined by simply modifying the writing pattern, as controlled by the AFM Nanoscope software. Deposition only occurs at positive sample voltage above a 6 V threshold, where the current across the gap departs from the linear ohmic regime observed for lower positive sample voltages or negative sample voltages (no deposition of material on the tip is observed up to -20 V sample voltage). These results suggests a reaction mechanism where electrons injected from the tip into the unoccupied molecular orbitals of the precursor, as well as the electric field direction, play important roles. The lack of deposition when the polarity is switched (negative sample voltage) may indicate higher electron injection efficiency of the tip, where the electric field is higher due to its sharpness, with respect to the comparably flat substrate. Above 20 V positive sample bias, nanostructure growth becomes inhomogeneous and erratic; other reactions may occur such as direct field-induced precursor dissociation or field-induced discharge through the thin native oxide layer. Precursor thermochemistry caused by high-temperature localized Joule heating of the area is unlikely; the silicon substrate and the surrounding liquid DPG are macroscopic heat sinks that limit the temperature increase at the tip-sample interface.

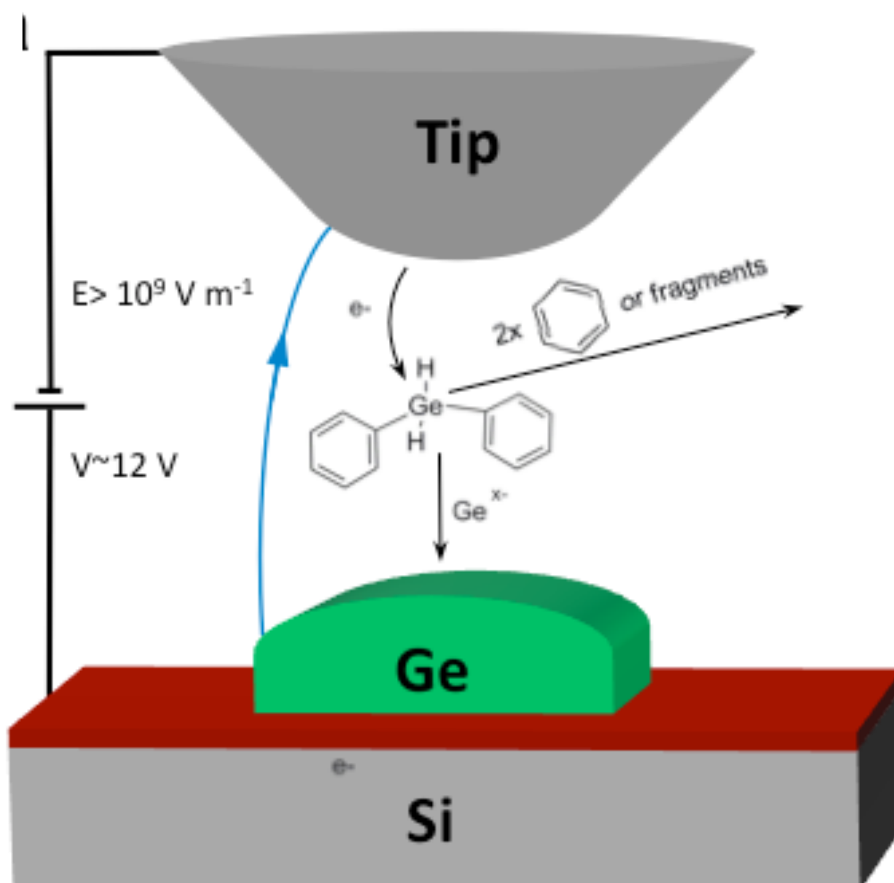

Figure 4.1. Schematic of the probe sample geometry and proposed chemical reaction for Ge nanostructure AFM direct-write. Upon the onset of a ≈12 V bias, electrons tunnel from the tip into an unoccupied DPG orbital. The charged DPG reacts under the high electric field (>10^9 V m^{-1}) and grows Ge from the surface.

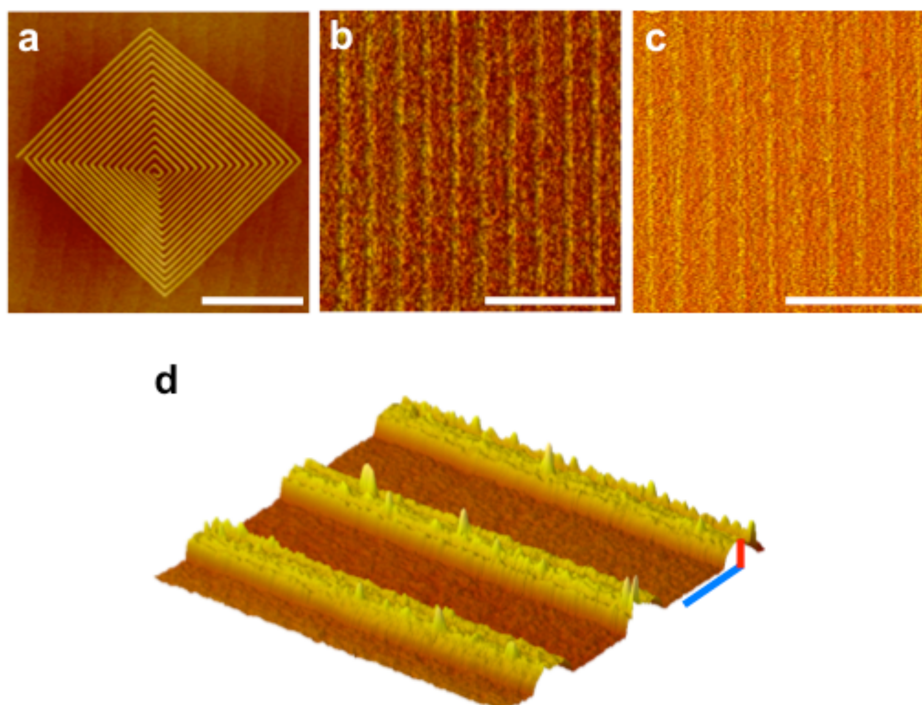

Figure 4.2 Tapping mode AFM images of germanium nanostructures: a) topographic image of spiral written at 12 V and 1 μm s^{-1}, b) 25 nm lines written at 14 V and 100 μm s^{-1}, c) phase image of lines in image (b) showing contrast between the Ge features and the Si substrate, and d) 175 nm wide 5 nm tall lines written at 16 V and 1 μm s^{-1}. Scale bars 5 μm (a), 500 nm (b,c), 300 nm horizontal and 5 nm vertical (d). Height scale from dark brown to bright yellow 5 nm (a,b). Phase scale dark brown to bright yellow 45° (c).

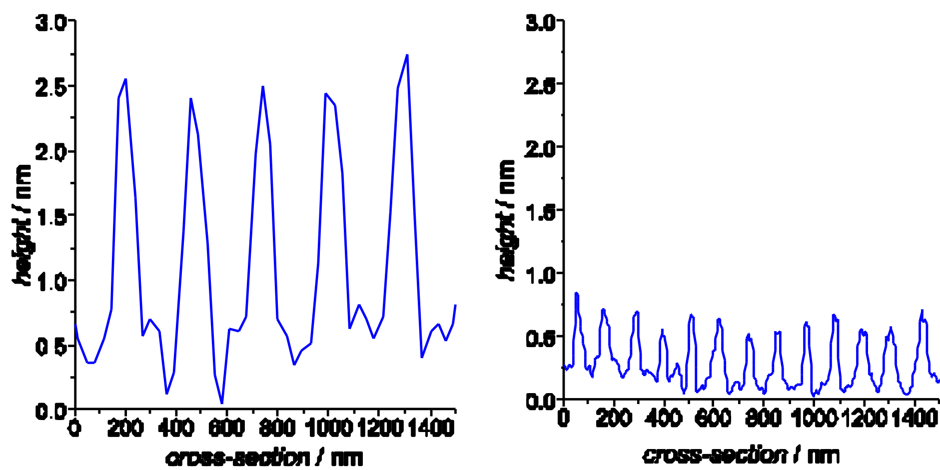

Figure 4.3. Line cross-sections corresponding to the AFM images in Figures 1b and 1c. Ge nanoribbons were written at 12 V and 1 μm s^{-1} and 14 V and 100 μm s^{-1} respectively

4.4 Characterization of Nanostructures Fabricated by AFM Direct Write

4.4.1 Introduction to Characterization of Nanostructures Fabricated by AFM Direct Write

After demonstrating the direct write of nanostructures from DPG, the next step was to develop a characterization protocol. The size of the nanostructures typically produced by AFM direct write, 5μm x 5μm x 5nm, makes characterization a challenging endeavor. The following subsections describe the techniques used for confirmation of the localized nature of the reaction, including confirmation of Ge in the deposited structures. Additionally, qualitative and first approximation quantitative analysis of the carbon content is described, as well as the first efforts towards understanding the microstructure of structures fabricated using this technique.

4.4.2 Time-of-Flight Secondary Ion Mass Spectroscopy

Time-of-Flight Secondary Ion Mass Spectrometry be used to examine the chemical functionality, segregation of constituents and impurities (laterally and with depth), and the cleanliness of a surface.[31] In the ToF-SIMS technique, a focused ion beam, the primary ions, bombards the surface of the sample (Figure 4.4).[31] Through atomic collisions, these primary ions transfer their energy to target atoms, beginning a collision cascade.[31] It is important to note that the collision cascade destroys the molecular integrity of the entire sample not only at the surface, but at deeper layers due to the trajectory of the primary recoil atoms.[32] The lateral resolution is given by the desorption process, which is given by the dimensions of the collision cascade.[32] The dimensions of the cascade are a function of the primary ion, including its mass, energy, angle of incidence, and polyatomicity, in addition to the mass and density of the target.[32] The energy from the cascade is partially transmitted back to the surface, giving surface atoms and fragments enough energy to overcome their surface binding energy.[31] While most of the fragments and atoms that come off of the surface are neutral, there exists a fraction of atoms that are positively

charged and a fraction of atoms that are negatively charged, one of which the user picks to mass analyze.[31] Only a fraction of the molecules on the surface are ejected as charged particles, between 10^{-6} and 10^{-1} of the total atoms are secondary ions.[32] The secondary ions are analyzed by passing them through a high voltage potential and then determining their mass using the time of flight from the sample to the detector.[31]

ToF- SIMS can be run in two different modes: static SIMS and dynamic SIMS. Static SIMS offers the user the ability to gain chemical and molecular information from the unperturbed surface because it uses a low flux (10pA-5nA) and only sputters up to ~0.1% of the top monolayer.[31] In dynamic SIMS, a higher flux is used (μA) to understand the elemental distribution of the sample, in addition to performing depth profiling. For inorganic nanostructure characterization experiments, ToF-SIMS was performed in dynamic mode.

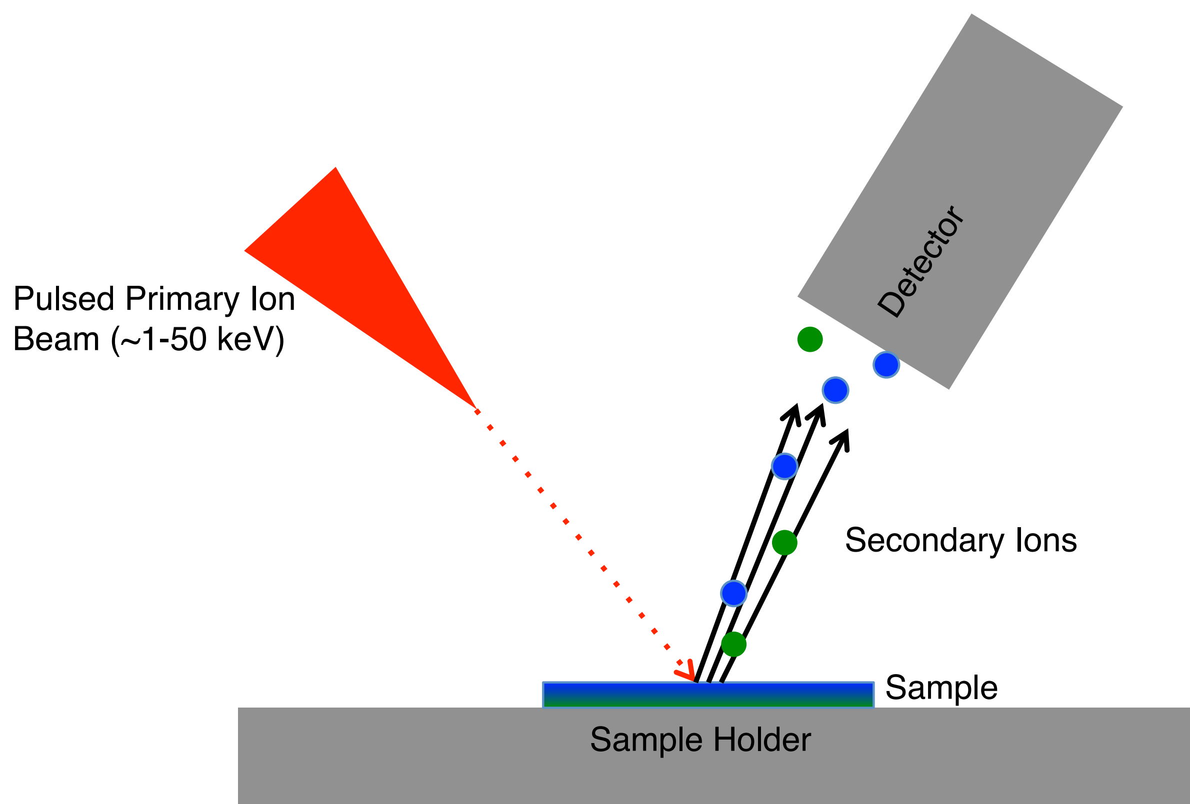

Figure 4.4 ToF-SIMS schematic. In the ToF-SIMS process, a pulsed primary ion beam strikes the sample, causing the formation of secondary ions which pass through a mass analyzer.

To verify our conjecture for the reaction mechanism forming Ge nanostructures from DPG, the chemical composition of the nanostructures is initially analyzed via Time-of-Flight Secondary Ion Mass Spectroscopy (ToF-SIMS) (Figure 4.5**)**. Time-of-flight secondary ion mass spectroscopy (ToF-SIMS) was performed at the Environmental Molecular Sciences Laboratory at Pacific Northwest National Laboratory with a TOF.SIMS5 spectrometer (ION-TOF GmbH, Germany). A 25 keV Bi^+ ion beam, which is focused into a diameter of ~250 nm with a current of 0.6 pA at 20 kHz repeating rate, is used to image the area of interest. Each image is 256 × 256 pixels with 40 scans. Positive ions are analyzed and a 1.0 keV O_2^+ beam is used for sputtering the sample between measurements. Sputtering is used to remove surface contamination, it is estimated that 30 s of sputtering removes approximately 2 nm of material if using silicon dioxide as reference.[33]

To facilitate sample location, larger microscopic pads are fabricated by writing, from DPG, several lines in close proximity to each other (Figure 4.5a). Initial ToF-SIMS scans do not reveal any structure specificity for Ge^+ or CH_3^+ ions (Figure 4.5b and Figure 4.5e), indicating the presence of trace precursor contamination everywhere on the surface as may be expected from exposure to the liquid DPG. However, upon a brief O_2^+ cleaning, germanium is selectively found only in the nanofabricated structures (Figure 4.5c). The absence of CH_3^+ signal suggests no carbon incorporation (Figure 4.5f). Upon further cleaning with the oxygen beam, the Ge ion signal becomes progressively weaker, indicating that the entire germanium-containing structures are being sputtered away (Figure 4.5d).

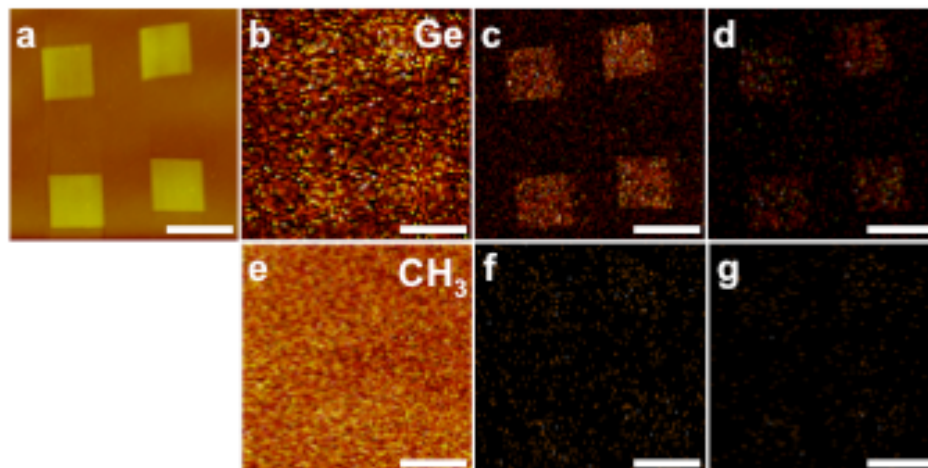

Figure 4.5 AFM image (a) and ToF-SIMS images (scale bars 20 μm) of 5 nm tall pads (16 V, 3 μm s^{-1}) after 450 °C Ar anneal. Germanium ion count (from dark brown to yellow) (b–d) and CH_3^+ ion count (e–g) are presented. Panels (b,e) were collected with no surface treatment, (c,f) after 10 s sputter cleaning with an O_2^+ beam to remove surface contamination, and (d,g) after 45 s of sputtering.

4.4.3 Photoemission Electron Emission Microscopy-Near Edge X-Ray Absorption Fine Structure

To further investigate the nature of the direct write products, we also employ near-edge x-ray absorption fine structure (NEXAFS) as recorded by a photo emission electron microscope (PEEM) (Figures 4.6 and 4.7). PEEM-NEXAFS spectra provide bonding information for a nanostructure, such as the type and directionality of the bond. In PEEM, the sample is exposed with x-rays of the desired wavelength produced by synchrotron radiation. Absorbed x- rays cause the excitation of an inner/core electron to either an excited state like the lowest unoccupied molecular orbital (LUMO) or to be completely ionized. When the energy of the x-rays matches the energy difference between the core level and an unoccupied state, the cross section for the transition is increased. The core state is left empty, and secondary electrons are generated by the decay of the core hole (Figure 4.6).[34] A cascade of low-energy electrons is created from Auger processes and inelastic electrons, some of which penetrate the sample surface, escape into vacuum and are collected and focused on a CCD detector by the PEEM optics.[34] The energy range of PEEM-2 is 200-1300 eV, while the spatial resolution is ~50-100 nm. Additionally, most of the signal is generated in the top 2-5 nanometers of the sample surface.[34] Thus, this makes this technique unique in that the chemical content of a nanostructure structure can be determined with spatial resolution on the nanoscale.

PEEM-NEXAFS has been successful in characterizing high-field-lithography-fabricated carbon pads[26,29] and is capable of detecting elemental carbon in all molecular forms and fragments. Spectromicroscopic characterization was carried out at beamlines 7.3.1 (PEEM-2) and 11.0.1 (PEEM-3) of the Advanced Light Source at the Lawrence Berkeley National Laboratory. PEEM records the total electron yield (TEY), a measure of the x-ray absorption of

the sample, with a maximum spatial resolution of ca. 50 nm. Local C K-edge (PEEM-2) and Ge $L_{2,3}$-edge (PEEM-3) NEXAFS spectra were obtained with ca. 0.3 eV energy resolution from stacks of PEEM images taken at successive x-ray energies. The detector dark current was subtracted and the spectra were normalized to unity from 5 to 10 eV before the edge jump to extract chemical information that is encoded in the energy-dependent absorption of the sample. Non-energy-dependent effects caused by differences in illumination and local work function were thus removed.

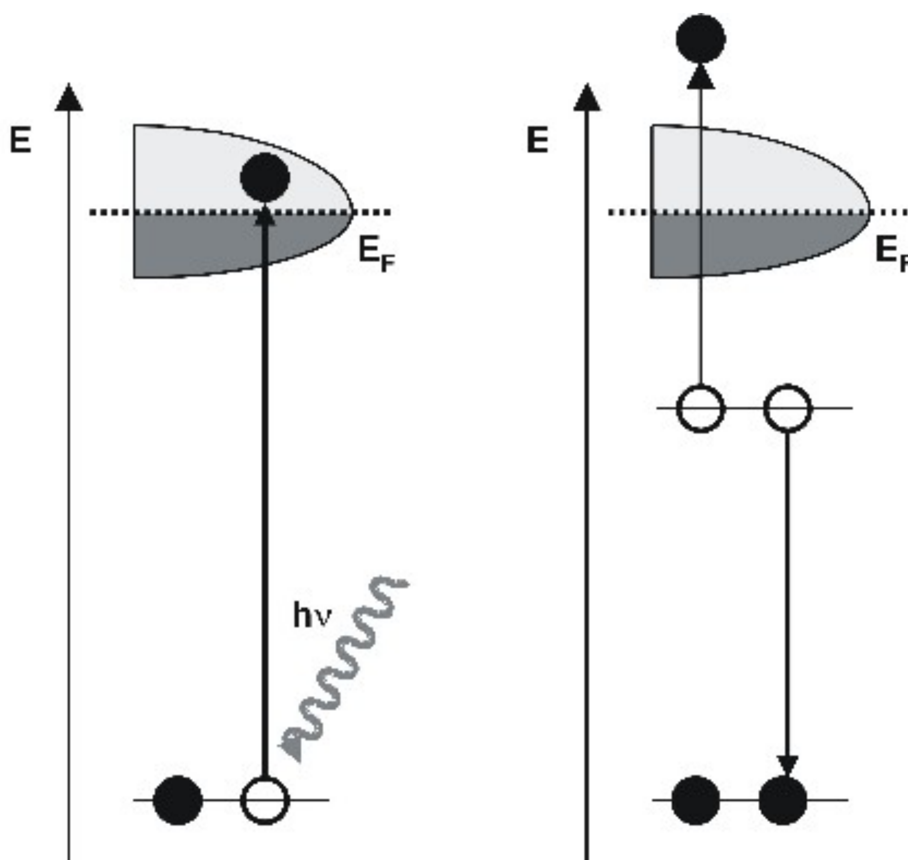

Figure 4.6 NEXAFS-PEEM Process
(Reprinted with permission from Dr. A.Scholl, Lawrence Berkeley National Laboratory)

4.4.4 PEEM-NEXAFS for C Content in AFM Direct Write Structures

The presence of carbon in the Ge structures is initially assessed by comparing C K-edge spectra of nanostructures fabricated from n-octane and structures fabricated from DPG. The n-octane shows a peak at 285.7 eV and a broad edge onset at 290 eV. These features correspond to the transition of a photoelectron from the 1s → π^* and a 1s → σ^* transition respectively.[35] This indicates the presence of sp^2 and sp^3 hybridized carbon, which is consistent with previous results on AFM direct write of n-octane. NEXAFS C-K edge spectra for room temperature Ge structures and structures annealed at 450°C in argon show a decrease in signal for annealed samples (Figure 4.7). Rather than a decrease in signal, carbonaceous structures display a transformation of bonding arrangement from sp^3 to sp^2 upon annealing.[8] This provides qualitative proof that structures fabricated from DPG are not carbonaceous in nature. NEXAFS is also used to quantitatively assess the carbon content of the Ge nanostructures (Figure 4.7). Previously, PEEM-NEXAFS and EELS have been used to quantify the sp^2 to sp^3 ratio in carbonaceous structures.[29,36,37] In NEXAFS ratio calculations; a sample is normally compared to a HOPG sample, which consists of pure sp^2 carbon. For these experiments, germanium samples are compared to reference samples of carbon deposited using AFM direct write in order to determine a first approximation of the carbon content of the Ge stuctures. The structures fabricated from n-octane contain solely carbon; therefore, this sample is chosen as a carbon standard. As in previous NEXAFS work for AFM direct write, spectra are acquired by the PEEM around the C Kedge both on and off the direct write structures.[26,29] The signal on the structure is divided by the signal off the structure, which serves as an I_0 correction to compensate for the energy dependence of the X-ray flux in the beam line.[29] For all data, the π^* transition peak is shifted to 284.4 eV and the curve is baselined to 0 at 280 eV. The carbon data is then normalized to 1 at

the π^* transition peak. In order to evaluate carbon content, the area between 280-305 eV was chosen to incorporate sp^2 and sp^3 carbon signals. The area under the curve was integrated by setting a baseline at y= 0 using a trapezoidal approximation in Origin. The area under the Ge curve for the annealed and post-annealed samples were integrated using the same procedure. Carbon content is defined as

$$Atomic\ Percent\ Carbon = \frac{Area_{DPG\ Pads}}{Area_{n-octane\ Pads}} * \frac{\frac{Density_C}{MW_c}}{\frac{Density_{Ge}}{MW_{Ge}}} * 100$$

The error was determined by using peak-to-peak noise of each spectrum as the error in each spectrum and integrating the noise over the selected energy range and then propagating the error.

In the Ge pads deposited from DPG as annealed, the atomic percent carbon content was **18.8±6.2%**, while the weight percent was **3.1±1%.**

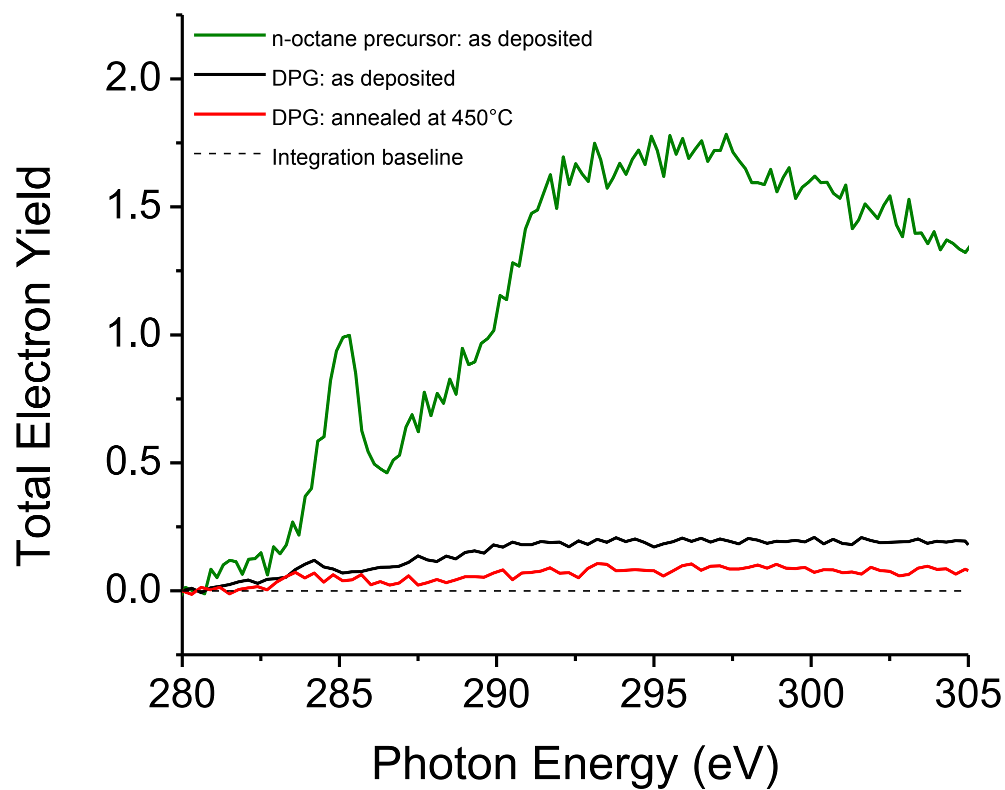

Figure 4.7 NEXAFS spectra acquired at the onset of the C K-edge on Ge pads at room temperature (black), annealed at 450°C (red), and pads written with n-octane precursor (green) to verify C content of Ge structures.

4.4.5 PEEM-NEXAFS for Inorganic Content in AFM Direct Write Structures

NEXAFS-PEEM was also used to confirm the presence of Ge in the nanostructures. Total electron yield (TEY, Figure 4.8a) images collected with PEEM after the Ge L3 edge (1218 eV), including the Ge L2 edge (1248 eV), shows higher germanium content on the structures than on the substrate (Figure 4.8c), which is in agreement with the ToF-SIMS data. The shape and structure of the Ge L2,3 edges are also an indicator of the crystallinity of a germanium-based material. Absorption spectroscopy performed on a Ge single crystal ingot cleaved down the (111) direction in ultrahigh vacuum showed a sharp L3 edge structure consisting of three peaks and then a series of broad peaks extending to the L2 edge.[38] From comparisons of amorphous Ge (a-Ge) and crystalline Ge (c-Ge), it is apparent that c-Ge spectra are dominated by an initial steep edge followed by a local minimum which then increases again towards the L2 edge (Fig 4.8d).[39,40] The spectra of a-Ge are smoothed out and the local minimum is almost completely absent from the structure.[40] A comparison of Ge L2,3 spectra from structures fabricated from DPG (Figure 4.8c) and a crystalline Ge wafer (Figure 4.8b) indicates that the fabricated nanostructures posses c-Ge character; as seen from the sharp edge in both spectra, as well as the local minimum between the L2 and L3 edges.

The presence of oxide contamination and physisorbed germanium oxide was also analyzed. Germanium predominantly oxidizes to GeO and GeO_2. While GeO_2 is soluble in water,[41] no dissolution of structures produced from AFM direct write in water is observed. GeO, the less stable oxide, sublimes at 710°C.[42] Upon high temperature annealing of the deposited structures, no change in volume is observed. These results indicate the formation of oxides during the process may not be a favorable pathway. It is likely that upon exposure to

atmosphere, a thin layer of oxide will form and that smaller nanostructures may oxidize throughout. The Ge L2,3 edges in NEXAFS are used to probe the S character of the unoccupied density of states above the Fermi level.[43] From previous NEXAFS analysis of Ge quantum[33] dots, peaks after the Ge edge have been labeled as Ge-O peaks with a 4p to 2s transition.[43] At approximately ~1222 eV, the Ge-O characteristic peak is observed.[39] In both the analyzed wafer (Figure 4.8b) and the nanostructures (Figure 4.8c), this peak is present and is most likely due to atmospheric exposure. This peak may be more pronounced in the nanostructures due to their high surface-to-volume ratio of the nanostructure compared to the Ge wafer.

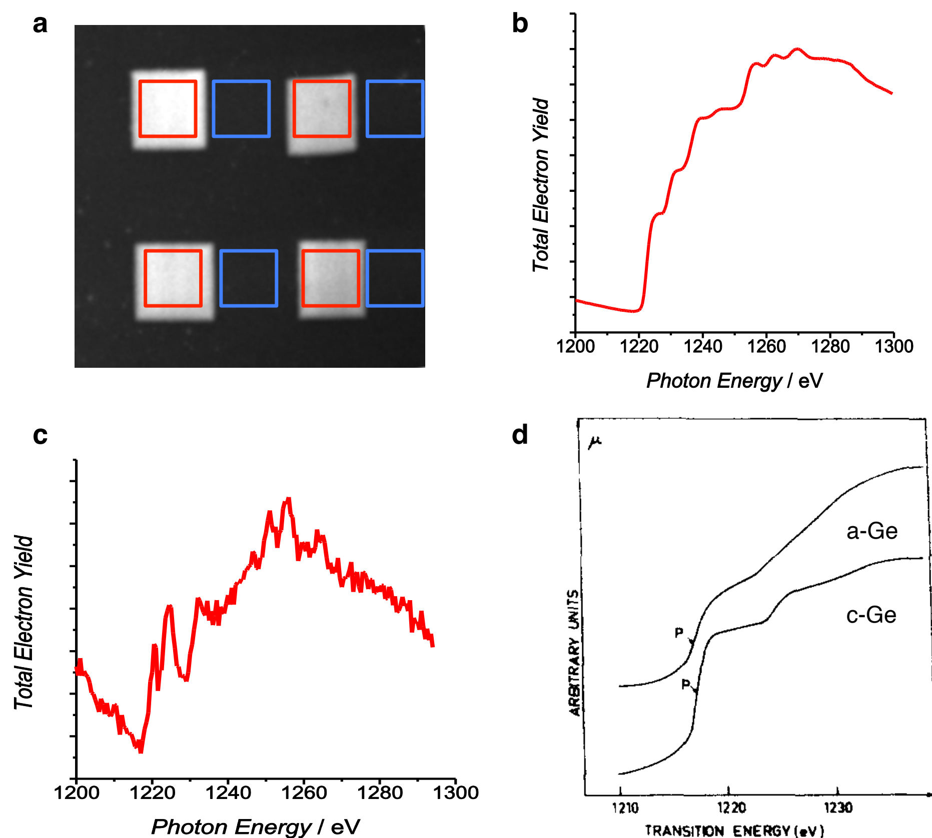

Figure 4.8. a) Total electron yield image (X-ray energy 1222 eV) and b) Ge L2,3 edge spectrum acquired on a Ge wafer. c) Ge L2,3 edge spectrum acquired on Ge structures written from DPG (12 V, 1 μm s^{-1}) and d) Literature comparison of a-Ge and c-Ge (Reprinted with permission from Belin, E., Cardinaud, C., Senemaud, C. & Dixmier, J. X-Ray absorption spectroscopy study of Ge Empty States in Crystalline and Amorphous Phases, Amorphous Ge:H and Si1-xGex:H. *Journal of Non-Crystalline Solids* **77&78**, 331-334 (1985)). For b-d, small variations in the edge onset arise from different experimental conditions and NEXAFS calibration.

4.4.6 Transmission Electron Microscopy

Transmission electron microscopy (TEM) was attempted in order to determine the epitaxial and crystalline nature of the deposited nanostructures structures. Due to the typical feature size produced by AFM direct write, sample preparation is complicated, requiring specialized equipment and a compelx series of steps. Samples for TEM are prepared from AFM direct write structures using focused ion beam (FIB) milling to cut a cross-section of the nanostructures and mill the cross-section until it is electron transparent. The FIB process requires the protection of the nanostructures, followed by cutting, milling, and mounting the sample on a grid for TEM analysis (Figure 4.9a). While an initial TEM analysis demonstrated possible nanostructure crystallinity (Figure 4.9b), efforts to conduct full TEM analysis did not yield viable results. FIB sample preparation was attempted in collaboration with industry (Semion), academic(ASU, BU), and national lab partners (EMSL/PNNL) without the completion of a viable TEM sample. Unfortunately, FIB sample preparation often causes damage and contamination of the sample due to the beam;[44] this damage was present in the attempted samples. Sample preparation on TEM grids with silicon and gold membranes was also attempted, but proved unsuccessful due to the fragility of the membrane. The complex nature of TEM sample preparation for AFM direct write structures will be the subject of future group work.

a

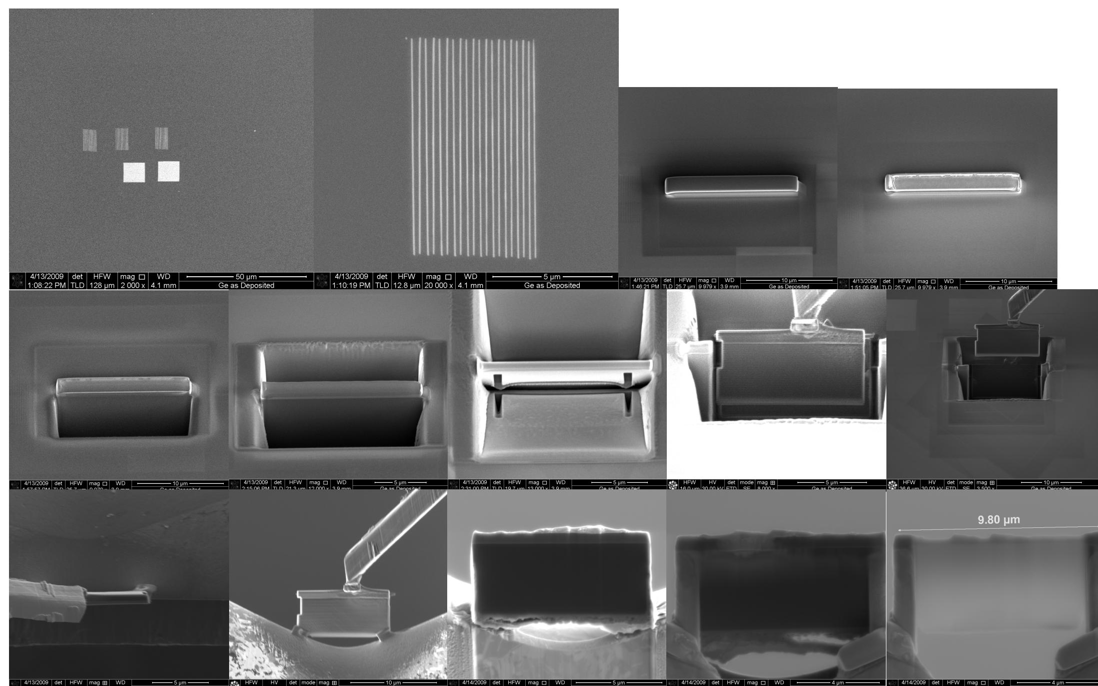

b

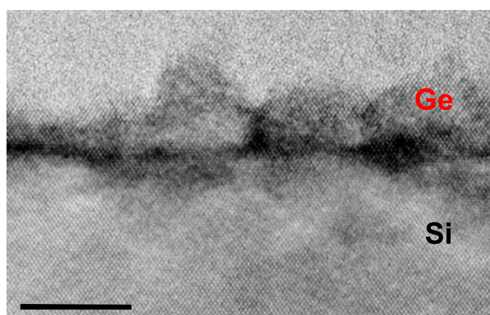

Figure 4.9 (a) FIB sample preparation sequence (Courtesy B.Arey, EMSL-PNNL). (b)TEM image of the Ge/Si interface. Scale bar = 5 nm. (Courtesy G. Tam and J. Tolle, Arizona State University)

4.5 Conclusions

From these analyses, we conclude that the direct write nanostructures are composed of germanium with little or no carbon contamination. It is likely that upon exposure to the atmosphere a thin layer of germanium oxide will form and some of the thinner nanostructures may oxidize throughout; this can be prevented by protecting the surface with covalently-bound self-assembled monolayers.[45] However, we do not observe dissolution of the nanostructures in water (as expected for GeO_2)[41] nor high temperature sublimation (as expected for the less stable GeO).[33] It is possible that the trace precursor observed in SIMS might create a capping layer that protects the structures from oxidation. Notably, the nanostructures do not suffer from any carbon contamination, which is often a problem when using organometallic precursors.[46] Carbon-free low-temperature synthesis of germanium nanowires from DPG has previously been demonstrated,[47] thus suggesting that DPG is a viable precursor for this growth process. Benzenes are known to be very stable leaving groups in normal conditions, but in the high-field area of the tip-sample interface, the exact chemical reactions occurring during nanostructure direct write require careful modeling that will be the subject of a future publication.

In conclusion, we have established a facile scheme for the 100 μm s^{-1} direct write of sub-30 nm germanium nanostructures with a commercially available precursor. This method merges the deterministic placement control of nanolithography with the ease of bottom-up growth in a single process. Our scheme can produce nanostructures with the same precision as electron beam-induced deposition[48] or STM-induced CVD,[49,50] but is not limited to working in vacuum with gaseous precursors that significantly limits scope and throughput. As a direct write method, it also significantly improves upon previous scanning probe strategies for Ge or metal fabrication in that it is not limited to complex substrates specifically designed for the purpose of

patterning,[51,52] and it does not require any cumbersome post-fabrication wet-etching steps.[53] Furthermore, the Ge nanostructure direct write occurs as velocities as high as 100 μm s^{-1} and is fully compatible with multiple AFM tips working in parallel[54,55] or conducting nanostructured stamps[30] opening the possibility for higher throughput nanofabrication. Finally, a broad variety of solid-state materials can be written using this new method, by appropriately selecting precursors from the expansive library already developed for semiconductor MOCVD, allowing the facile fabrication of complex heterostructures for electronics and photonics applications.

4.6 References

1 Streetman, B. G. & Banerjee, S. *Solid State Electronic Devices-5th Ed.*, (Prentice Hall, 2000).

2 Wang, D. & Dai, M. *Applied Physics A: Materials Science & Processing* **85**, 217-225 (2006).

3 Vinet, M. *et al.* Germanium on Insulator and New 3D Architecture Opportunities for Integration. *Intenational Journal of Nanotechnology* **7**, 304-319 (2010).

4 Liang, D. & Bowers, J. E. Photonic integration: Si or InP substrates? *Electronics Letters* **45**, 578 - 581 (2009).

5 Roelkens, G. *et al.* III-V/silicon photonics for on-chip and intra-chip optical interconnects. *Laser & Photonics Reviews* **4**, 751-779 (2010).

6 Garcia, R., Martinez, R. V. & Martinez, J. Nano-chemistry and scanning probe nanolithographies. *Chemical Society Reviews* **35**, 29 (2006).

7 Ginger, D. S., Zhang, H. & Mirkin, C. A. The evolution of dip-pen nanolithography. *Angewandte Chemie-International Edition* **43**, 30-45 (2004).

8 Rolandi, M., Quate, C. F. & Dai, H. A New Scanning Probe Lithography Scheme with a Novel Metal Resist *Advanced Materials* **14**, 191-194 (2002).

9 Avouris, P., Hertel, T. & Martel, R. Atomic Force Microscope Tip-Induced Lodal Oxidation of Silicon: Kinetics, Mechanism, and Nanofabrication. *Applied Physics Letters* **71**, 285-287, doi:10.1063/1.119521 (1997).

10 Maoz, R., Frydman, E., Cohen, S. R. & Sagiv, J. "Constructive Nanolithography": Inert Monolayers as Patternable Templates for In-Situ Nanofabrication of Metal–Semiconductor–Organic Surface Structures—A Generic Approach. *Advanced Materials* **12**, 725-731 (2000).

11 Kim, Y., Kang, S. K., Choi, I., Lee, J. & Yi, J. In situ Negative Patterning of p-Silicon via Scanning Probe Lithography in HF/EtOH Liquid Bridges. *Journal of American Chemical Society* **127**, 9380-9381 (2005).

12 Jang, J.-W. *et al.* Electrically Biased Nanolithography with KOH-Coated AFM Tips. *Nano Letters* **8**, 1451-1455 (2008).

13 Cen, C., Thiel, S., Mannhart, J. & Levy, J. Oxide Nanoelectronics on Demand. *Science* **323**, 1026-1030 (2009).

14 Xie, X. N. *et al.* Creating Polymer Structures of Tunable Electric Functionality by Nanoscale Discharge-Assisted Cross-Linking and Oxygenation. *Journal of the American Chemical Society* **128**, 2738-2744 (2006).

15 Germain, J., Rolandi, M., Backer, S. A. & Frechet, J. M. J. Sulfur as a novel nanopatterning material: an ultrathin resist and a chemically addressable template for nanocrystal self assembly. *Advanced Materials* **20**, 4526-4529 (2008).

16 Wang, D. *et al.* Thermochemical Nanolithography of Multifunctional Nanotemplates for Assembling Nano-Objects. *Advanced Functional Materials* **19**, 3969-3702 (2009).

17 Fenwick, G. *et al.* Thermochemical nanopatterning of organic semiconductors. *Nature Nanotechnology* **4**, 664-668 (2009).

18 Pires, D. *et al.* Nanoscale Three-Dimensional Patterning of Molecular Resists by Scanning Probes. *Science* **328**, 732-735 (2010).

19 Knoll, A. W. *et al.* Probe-Based 3-D Nanolithography Using Self-Amplified Depolymerization Polymers *Advanced Materials* **22** (2010).

20 Backer, S. A., Suez, I., Fresco, Z. M., Rolandi, M. & Frechet, J. M. J. Covalent Formation of Nanoscale Fullerene and Dendrimer Patterns. *Langmuir* **23**, 2297-2299 (2007).

21 Fresco, Z. M. & Frechet, J. M. J. Selective Surface Activation of a Functional Monolayer for the Fabrication of Nanometer Scale Thiol Patterns and Directed Self-Assembly of Gold Nanoparticles. *Journal of American Chemical Society* **127**, 8302-8303 (2005).

22 Unruh, D. A., Mauldin, C., Pastine, S. J., Rolandi, M. & Frechet, J. M. J. Bifunctional Patterning of Mixed Monolayer Surfaces Using Scanning Probe Lithography for Multiplexed Directed Assembly. *Journal of American Chemical Society* **2010**, 6890-6891 (2010).

23 Fresco, Z. M., Suez, I., Backer, S. A. & Frechet, J. M. J. AFM-Induced Amine Deprotection: Triggering Localized Bond Cleavage by Application of Tip/Substrate Voltage Bias for the Surface Self-Assembly of Nanosized Dendritic Objects. *Journal of American Chemical Society* **126**, 8374-8375 (2004).

24 Salaita, K., Wang, Y. & Mirkin, C. A. Applications of Dip-Pen Nanolithography. *Nature Nanotechnology* **2**, 145-155 (2007).

25 Suez, I., Backer, S. A. & Frechet, J. M. J. Generating an Etch Resistant "Resist" Layer From Common Solvents Using Scanning Probe Lithography in a Fluid Cell. *Nano Letters* **5**, 321-324 (2005).

26 Suez, I. *et al.* High-field scanning probe lithography in hexadecane: transitioning from field induced oxidation to solvent decomposition through surface modification. *Advanced Materials* **19**, 3570-3573 (2007).

27 Garcia, R. *et al.* Nanopatterning of carbonaceous structures by field-induced carbon dioxide splitting with a force microscope. *Applied Physics Letters* **96**, 143110:143111-143113 (2010).

28 Fu, L., Liu, X., Zhang, Y., Dravid, V. P. & Mirkin, C. A. Nanopatterning of “Hard” Magnetic Nanostructures via Dip-Pen Nanolithography and a Sol-Based Ink. *Nano Letters* **3**, 757-760 (2003).

29 Rolandi, M., Suez, I., Scholl, A. & Frechet, J. M. J. Fluorocarbon Resist for High-Speed Scanning Proble Lithography. *Angewandte Chemie-International Edition* **46**, 7477-7480 (2007).

30 Martinez, R. V., Losilla, N. S., Martinez, J., Huttel, Y. & Garcia, R. Patterning polymeric structures with 2 nm resolution at 3 nm half pitch in ambient conditions. *Nano Letters* **7**, 1846-1850 (2007).

31 Sodhi, R. N. S. Time-of-flight secondary ion mass spectrometry (TOF-SIMS):— versatility in chemical and imaging surface analysis. *The Analyst* **129**, 483-487 (2004).

32 Hagenhoff, B. *Mikrochimica Acta* **132**, 259-271 (2000).

33 Kita, K. *et al.* Control of high-k/germanium interface properties through selection of high-k materials and suppression of GeO volatilization. *Applied Surface Science* **254**, 6100-6105 (2008).

34 *Photoemission Electron MIcroscopy Ultrafast Dynamics-Tutorial-PEEM Technique*, 2009).

35 Ziethen, C. *et al.* Orbital Mapping of Carbon Thin Films by XANES-spectromicroscopy. *Journal of Electron Spectroscopy and Related Phenomena* **107**, 261-271 (2000).

36 Berger, S. D. & McKenzie, D. R. EELS analysis of vacuum arc-deposited diamond-like films. *Philosophical Magazine Letters* **57**, 285-290 (1988).

37 Fallon, P. J. & Brown, L. M. Analysis of Chemical-Vapour-Deposited Diamond Grain Boundaries Using Transmission Electron Mircroscopy and Parallel Electron Energy Loss Spectroscopy in a Scanning Tunneling Electron Microscope. *Diamond and Related Materials* **2**, 1004-1011 (1993).

38 Naoe, S. *et al.* L3 Absorption Spectrum of Germanium Single Crystal. *Journal of Electron Spectroscopy and Related Phenomena* **79**, 5-8 (1996).

39 Glover, C. J., Ridgway, M. C., Llewellyn, D. J., Kluth, P. & Johanessen, B. Formation and electronic structure of germanium nanocrystals formed by ion beam synthesis. *Nuclear Instruments and Methods in Physics Research B* **238**, 306-209 (2005).

40 Belin, E., Cardinaud, C., Senemaud, C. & Dixmier, J. X-Ray absorption spectroscopy study of Ge Empty States in Crystalline and Amorphous Phases, Amorphous Ge:H and Si1-xGex:H. *Journal of Non-Crystalline Solids* **77&78**, 331-334 (1985).

41 Oliveira, A. B., Medeiros-Ribeiro, G. & Azevedo, A. Submicron fabrication by local anodic oxidation of germanium thin films. *Nanotechnology* **20** (2009).

42 Xie, T. *et al.* Characterization and growth mechanism of germanium nitride nanowires prepared by an oxide assisted method. *Journal of Crystal Growth* **283** (2005).

43 Heigl, F. *et al.* in *14th International Conference on X-Ray Absorption Fine Structure (XAFS14)* Vol. 190 012130: 012131-012136 (Journal of Physics Conference Series, 2009).

44 Mayer, J., Giannuzzi, L. A., Kamino, T. & Michael, J. TEM Sample Preparation and FIB-Induced Damage. *MRS Bulletin* **32**, 400-407 (2007).

45 Wang, D., Chang, Y.-L., Liu, Z. & Dai, H. Oxidation Resistant Germanium Nanowires: Bulk Synthesis, Long Chain Alkanethiol Functionalization, and Langmuir−Blodgett Assembly. *Journal of American Chemical Society* **127**, 11871-11875 (2005).

46 Koops, H. W. P., Kaya, A. & Weber, M. Fabrication and characterization of platinum nanocrystalline material grown by electron‐beam induced deposition. *Journal of Vacuum Science and Technology B* **13**, 2400-2403 (1995).

47 Chockla, A. M. & Korgel, B. A. Seeded germanium nanowire synthesis in solution. *Journal of Materials Chemistry* **19**, 996-1001 (2009).

48 Crozier, P. A., Tolle, J., Kouvetakis, J. & Ritter, C. Synthesis of uniform GaN quantum dot arrays via electron nanolithography of D2GaN3. *Applied Physics Letters* **84**, 3441-3443 (2003).

49 deLozanne, A. Pattern Generation below 0.1 micron by Localized Chemical Vapor Deposition with the Scanning Tunneling Microscope. *Japanese Journal of Applied Physics* **33**, 7090-7093 (1994).

50 Marchi, F. *et al.* Direct patterning of noble metal nanostructures with a scanning tunneling microscope. *Journal of Vacuum Science and Technology B* **18**, 1171-1176 (2000).

51 Yanagi, H. & Ohno, T. Nanofabrication of Gold Particles in Glass Films by AFM-Assisted Local Reduction. *Langmuir* **Langmuir**, 4773-4776 (1999).

52 Lee, M., O'Hayre, R., Prinz, F. B. & Gur, T. M. Electrochemical nanopatterning of Ag on solid-state ionic conductor RbAg4I5 using atomic force microscopy. *Applied Physics Letters* **85**, 3552-3554 (2004).

53 Anstankova, K. N. *et al.* Scanning-probe-induced local decomposition of solid germanium monoxide films: The nano-patterning of Germanium. *Journal of Surface Investigation: X-Ray, Synchrotron, and Neutron Techiques* **3**, 773-780 (2009).

54 Wilder, K., Soh, H. T., Atalar, A. & Quate, C. F. Nanometer-scale patterning and individual current-controlled lithography using multiple scanning probes. *Review of Scientific Instruments* **70**, 2822-2828 (1999).

55 Salaita, K. *et al.* Massively Parallel Dip–Pen Nanolithography with 55 000-Pen Two-Dimensional Arrays. *Angewandte Chemie International Edition* **45**, 7220-7223 (2006).

CHAPTER 5: Ge, Si, and $Si_{1-x}Ge_x$ Nanostructure Fabrication

Abstract

Precise materials integration in nanostructures is fundamental for future electronic and photonic devices. We demonstrate Ge, Si, and SiGe nanostructure direct-write with deterministic size, geometry, and placement control. The biased probe of an atomic force microscopy (AFM) reacts diphenylgermane or diphenylsilane to direct-write Ge, Si, and SiGe nano and heterostructures. Parallel direct-write is available on large areas by substituting the AFM probe with conducting microstructured stamps. This facile strategy can be easily expanded to a broad variety of semiconductor materials through precursor selection.

5.1 Introduction

In the prior chapters, nanostructure direct-write using the tip of an atomic force microscope to control the size, shape, and composition of semiconductor nanostructures has been demonstrated.[1-3] In this chapter, the AFM direct write technique is expanded to the fabrication of Ge, Si, and SiGe nanostructures as well as Ge/Si heterostructures. The biased probe of an AFM reacts diphenylgermane or diphenylsilane to direct-write Ge and Si nano and heterostructures.

Low-cost, high throughput of semiconductor heterostructures also remains a challenge. To this end, parallel patterning using the high field direct write technique has been demonstrated using a flexible stamp approach and will be discussed in this chapter. By substituting the AFM probe with conductive, microstructured stamps, the high field chemical reaction can be scaled up from one reaction site at the tip-sample gap to a large array of reaction sites.

This chapter is presented in a similar form as it was published in *Nano Letters*,[1] with an expanded discussion on reactive stamping and large scale throughput. Reprinted with permission from Vasko, S. E. *et al.* Serial and Parallel Si, Ge, and SiGe Direct Write with

Scanning Probes and Conductive Stamps. *Nano Letters.* **11**, 2386-2389 (2011) (http://pubs.acs.org/articlesonrequest/AOR-zWeTYCW2CBii6KEjvmI8). Copyright 2011 American Chemical Society.

5.2 Serial Ge, Si, and SiGe Direct Write with Scanning Probes

Recent advances in epitaxial transfer[2-4] and vapor-liquid-solid growth (VLS)[5-7] have demonstrated precise materials integration in semiconductor nanostructures. These nanostructures will likely play a key role in the future of electronic and photonic devices.[8] Advantages of multi-material nanostructures range from strain induced gain in charge carrier mobility[9] to composition dependent band gap engineering.[10] Epitaxial transfer produces high performance electronic and photonic devices. However, epitaxial transfer still involves traditional semiconductor fabrication, which may not be the best option when performance is not the only design driver. Amongst these, solid-state semiconductor photovoltaic applications would greatly benefit from a less demanding materials integration alternative.[11] VLS growth offers a cost-effective wide library of available materials ranging from Ge, Si, $Si_{1-x}Ge_x$[12,13] and III-Vs.[14] While geometry and placement control has been greatly improved,[15] obtaining deterministic growth for effective on-chip integration is still challenging. An intriguing strategy is to localize growth using scanning probes instead of a catalyst particle. This strategy allows to precisely control growth placement as well as growth direction. In this fashion, metallic and semiconductor features have been demonstrated via scanning tunneling microscope chemical vapor deposition (STM-CVD).[16-18] However, low throughput and high vacuum conditions required during growth limit such nanostructures to laboratory devices. The atomic force microscope (AFM) can fabricate nanostructures in ambient conditions.[19-25] Several AFM techniques such as dip-pen nanolithography (DPN)[26,27] and high-field carbon direct-write[28,29]

have been successfully demonstrated with greatly increased throughput. DPN affords fast writing at large scale with multiple self-aligned parallel tips.[30] High throughput large-scale carbon direct-write can be performed at 1 cm s^{-1} tip speeds[28] or by using microstructured conducting stamps that mimic multiple parallel tips.[31] Recently, we have demonstrated that AFM high field direct-write can write sub-30 nm carbon-free Ge nanostructures as a faster, more-approachable alternative to STM-CVD.[1,32,33]

Here, we show that this direct-write strategy can pattern broad variety of semiconductor nanostructures. Ge, Si, and SiGe heterostructures can be fabricated both with single AFM tips as well as conducting stamps (Figure 5.1). Individual tips offer nanometer resolution in small areas, while conducting stamps afford low-cost high-throughput large-area nanofabrication. For high resolution direct-write, a biased AFM tip traces desired shapes on the substrate while both are immersed in an inorganic liquid precursor (Figure 5.1a). A quartz cell designed for imaging in fluid (~ 1 ml) is used to contain the precursor. The electric field between the tip and the substrate ($> 10^9$ V m^{-1}) initiates the chemical reaction that deposits the desired material onto the substrate.[33] As previously demonstrated, Ge direct-write is accomplished from diphenylgermane (DPG, Gelest).[32,33] For Si direct write we choose the Si equivalent of DPG, diphenylsilane (DPS, Sigma-Aldrich) (Figure 5.1b). This family of precursors with aromatic groups is particularly suited for the AFM direct-write reactions. For these precursors, the most energetically favorable fragmentation route under high field and electron bombardment involves the two phenyls and the two hydrogens leaving as benzene.[33] This leaves a Ge or Si radical or ion free for deposition onto the substrate. The direct-write product should thus be free of any carbon contamination, which is often a problem when using organometallic precursors.

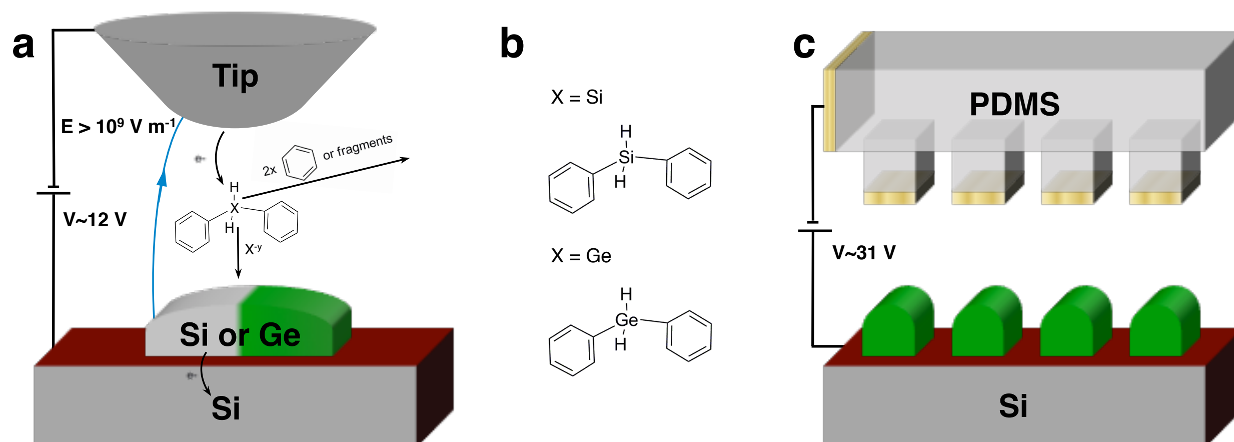

Figure 5.1. Schematic of the probe sample geometry and deposition process for AFM direct write (a) and parallel patterning via stamping (c). In the AFM direct write geometry, a moderate bias (≈12V) is applied, inducing a large electric field ($>10^9$ V m^{-1}). Electrons tunnel from the tip into the precursor molecule, where X= Ge or Si (b), and cause the subsequent fragmentation of the precursor and deposition of the desired inorganic atom. In the parallel patterning scheme, this reaction occurs at each of the multiple nanoscale asperities present on the stamp, yielding an array of deposited structures.

5.3 Deposition of Ge and Si Hetrostructures

Ge and Si heterostructures are routinely produced at a rate of 1 μm sec^{-1} (Figure 2a-c). Complex architectures made of Ge and Si nanostructures can be easily fabricated. This is accomplished in a single direct-write session without the need of tip-sample realignment. First, Ge direct-write is performed in DPG (Figure 5.2a, Pac-Man). Second, the reaction volume is flushed with an excess (> 20 ml) of DPS to ensure minimal precursor cross-contamination. Third, Si direct write is performed from DPS (Figure 5.2a, Pac-Dot). This is quite a general procedure that can produce Ge and Si heterostructures (Figure 5.2b and c). Cross-bar architetures with Ge and Si nanoribbons intersecting each other are easily obtainable. Close analysis of the junctions shows that the second material (Si) is written on the top of the first one (Ge) when the direct-wrtie patterns are crossed (Figure 5.2c). Complex Ge and Si nanoribbon junction devices may thus be fabricated using AFM direct-write. To further the variety of materials, proof-of-concept SiGe nanostructures were made (Figure 5.2d). SiGe direct write is available because DPG and DPS are mutually soluble and can be easily introduced in the reaction volume.

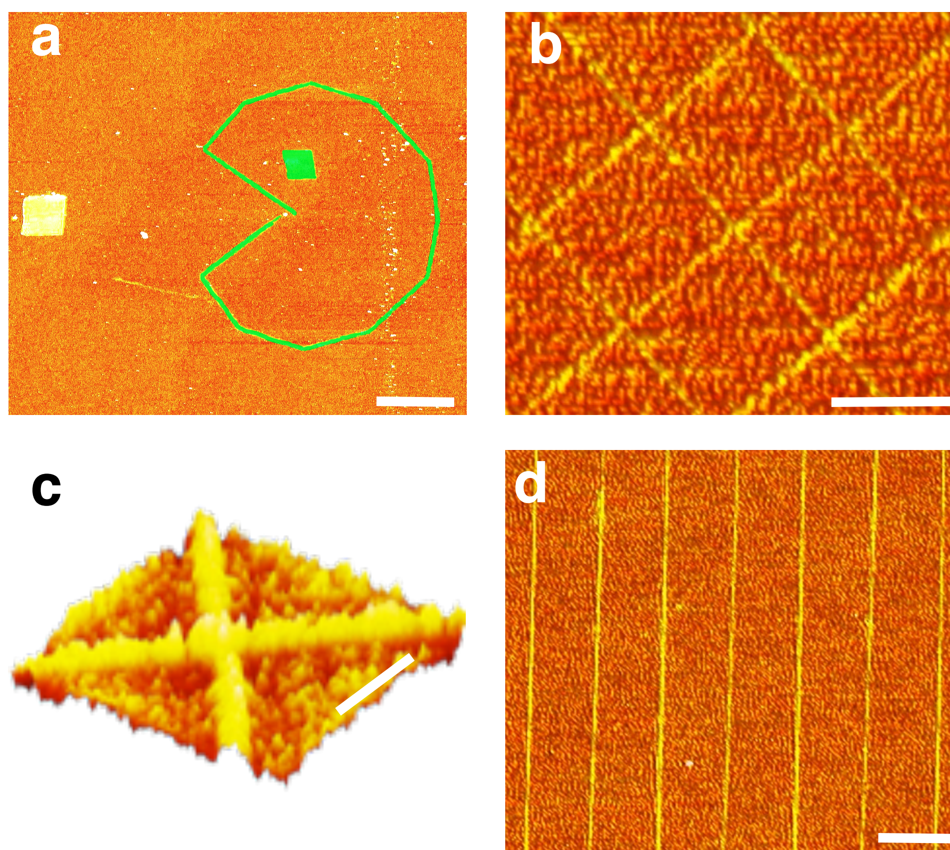

Figure 5.2. Tapping mode topographic AFM images of: a) False-colored Ge (green) and Si heterostructure PacMan. Ge pacman written at +12 V (sample) and 1 μm s^{-1}, Ge eyeball written at +11 V (sample) and 1 μm s^{-1}, Si pellet written at +12 V (sample) and 5 μm s^{-1}. b) Ge and Si crossbars, Ge lines written at +16 V (sample) and 1 μm s^{-1}, Si lines written at +12 V (sample) and 1 μm s^{-1}, c) Detailed view of a crossbar node from the previous image d) ~70 nm wide SiGe lines written at 10 V and 100 μm s^{-1} Height scale from dark brown to bright yellow 10 nm (a), 5 nm (b,c,d), (c). Scale bar= 500 nm (a), 500 nm (b), 300 nm (c), 1 μm (d). B and d were enhanced with 45° virtual illumination.

5.4 Characterization of Ge, Si, and $Si_{1-x}Ge_x$ Nanostructures

To ensure high-quality of the Ge and Si direct-write patterns, we perform careful chemical analysis of patterns deposited from filtered DPG and DPS (Whatman filter, 0.2 μm). Chemical composition is first determined using time-of-flight secondary ion mass spectroscopy (ToF-SIMS; Figure 5.3a-i).[28,32] To facilitate sample location, DPG, DPS, and 1:1 DPG:DPS microscopic pads are fabricated via AFM direct write (Figure 5.3a, d, g). Since a Si nanostructure on a Si wafer does not provide chemical contrast, samples were prepared on a thin W film. From the ToF-SIMS scans, germanium (Figure 5.3a-c) and silicon (Figure 5.3d-f) are found only in structures nanofabricated from DPG and DPS respectively. For the sample prepared from DPG:DPS, both semiconductors are present in the SIMS spectra (Figure 5.3g-i). However, it was not possible to determine if the Ge:Si ratio matches the solution stoichiometry. This will require careful refinement of these measurements.

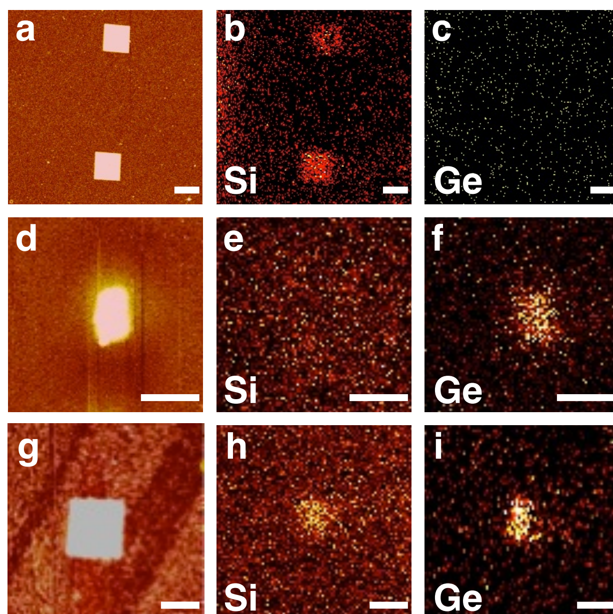

Figure 5.3. Representative AFM images of Si, Ge, and SiGe (a, d, g) pads (scale bars 2.5 µm, height scale = 10 nm) and ToF-SIMS images (scale bars 2.5 µm, 256 x 256 pixels, 40 scans) of Si, Ge, and SiGe nanostructures respectively. Silicon ion count (from dark brown to yellow, b, e, h) and Germanium-74 ion count (c, f, i). Data was collected after cleaning with a 1 keV O^{2+} beam to remove surface contamination.

TEY

280 285 290 295 300

Photon Energy / eV

As purity is essential for electronic grade semiconductors, we carefully evaluate carbon contamination of the patterns. To this end, we employ near-edge X-ray absorption fine structure (NEXAFS) as recorded by a photo-emission electron microscope (PEEM; Figure 5.4).[32,34,35] NEXAFS spectra were obtained with ca. 0.3 eV energy resolution from stacks of PEEM images taken at successive X-ray energies. Here, we estimate the relative carbon content from the C K-edge spectra of patterns prepared from DPG, DPS, and n-octane for comparison.[32] From this data, it is clear that Ge fabricated nanostructures are completely carbon free and that Si fabricated structures contain, at most, carbon traces. The Ge result is not totally surprising. Ge has no carbon solubility in a broad temperature range. On the other hand, carbon readily dissolves in silicon in the formation of silicon carbide. The lack of carbon on the Si structures confirms that the phenyls on the precursor molecules are indeed good leaving groups for this chemistry. Using the method developed for a first approximation of carbon content in an AFM direct write nanostructure introduced in Chapter Four, the carbon content of the Si nanostructures was also calculated (Figure 5.5). For the Si annealed sample, the atomic percent carbon content was **15.8±3.8%** and the weight percent carbon content was **5.4±1.8%**.

From this result, it is foreseeable that other diphenyl or triphenyl- type organometallic precursors may be used to expand the composition of available nanostructures. Exciting possibilities include using group III and group V precursors to create compound semiconductors. Furthermore, these precursors may be added in small quantities to DPG or DPS to dope nanostructures during growth.

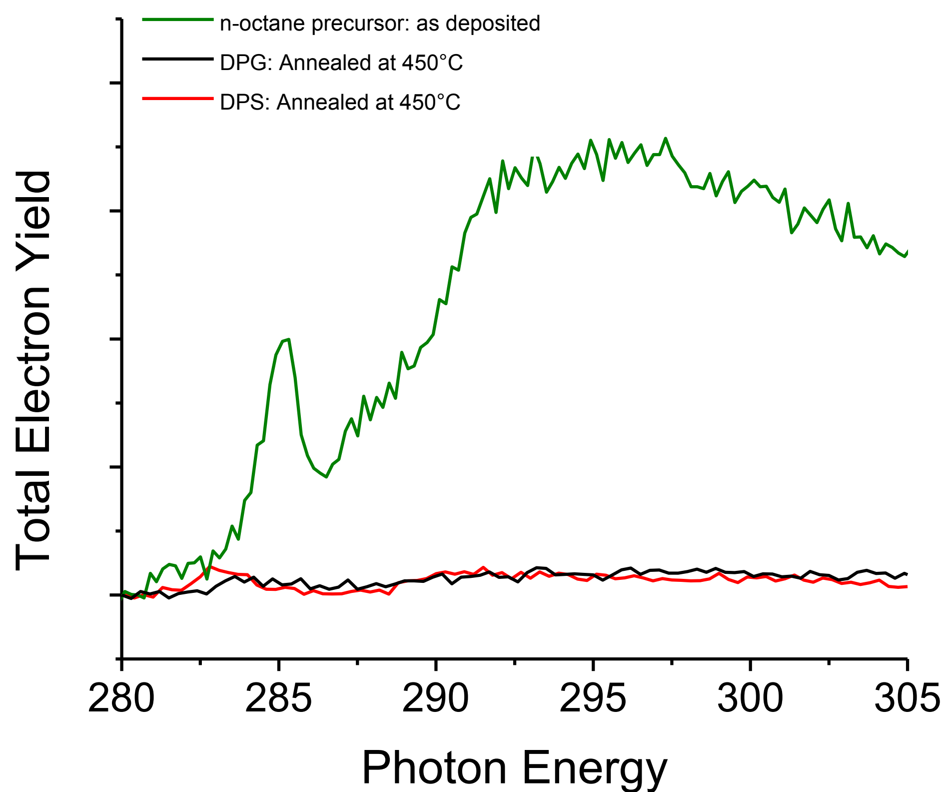

Figure 5.4
NEXAFS spectra acquired at the onset of the C K-edge (285.7 eV) on Ge pads written from DPG (black), Si pads written from DPS (red), and pads written with n-octane precursor (green) to verify C content of Ge and Si structures.

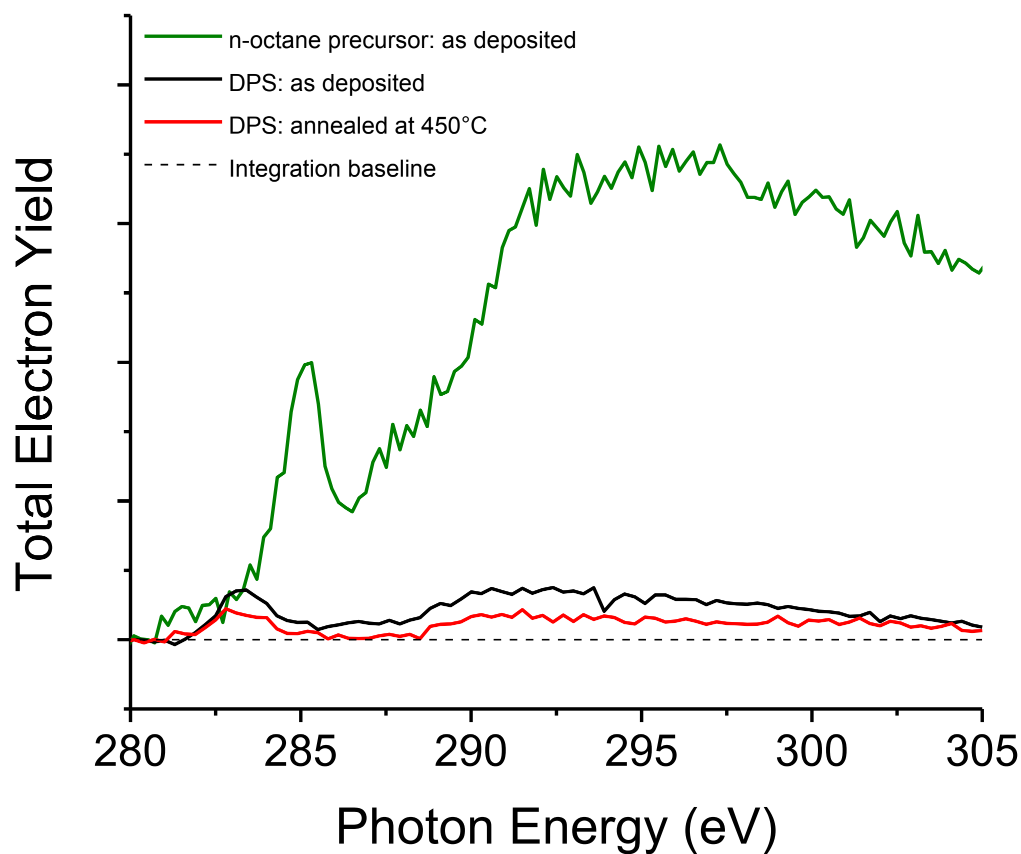

Figure 5.5
NEXAFS spectra acquired at the onset of the C K-edge on Si pads at room temperature (black), annealed at 450°C (red), and and pads written with n-octane precursor (green) to verify C content of Si structures.

5.5 Reactive Stamping

5.5.1 Introduction to Reactive Stamping

Throughput is a recurring concern for scanning probe based fabrication strategies. Carbon direct-write is feasible on large areas at velocities as high as 1 cm s^{-1}.[28,36] However, we have not yet found appropriate precursors to replicate such velocities in semiconductor direct-write. An alternate strategy to increase throughput is to mimic multiple tips working in parallel by using microstructured conductive stamps. Parallel patterning via stamping has been demonstrated for oxide[37] and carbonaceous features.[31] Results from organic precursor direct write are particularly encouraging for our efforts, given the similar high-field reactions involved during deposition. For rapid demonstration of this concept, a simple stamping machine was built by taking advantage of the precise position control of the AFM platform. This approach follows the same philosophy of polymer pen lithography and eliminates the need for the fabrication of a complex stamping device. In our approach, 2 mm x 4 mm flexible stamps are mounted onto the liquid cell, which is used during AFM direct-write (Figure 5.6a).

5.5.2 Stamp Preparation

Polydimethylsiloxane (PDMS) stamps were prepared by previously developed replica molding using the surface of a blank compact disc (CD) as the master.[37] The finished stamp consists of an array of 200 nm tall parallel lines at 1.4-µm pitch (Figure 5.6b). PDMS preparation used the SYLGARD 184 elastomer kit; the elastomer base and curing agent were mixed in 10:1 proportion. After pouring the mixture over the master, the PDMS was cured at 100°C for 1 hour. The stamp is subsequently peeled from the master. The stamps were coated with a 5 nm Cr adhesion layer and a 50 nm gold conductive layer using a Balzers PLS 500 e-beam evaporator.

5.5.3 Proof-of-Concept Ge and Si Nanostructure Stamping on Si(100)

The AFM liquid cell provides a contained environment for the condensation of an inorganic meniscus between the stamp and the substrate. A conductive substrate is mounted on the AFM piezo stage. The liquid cell/substrate environment is purged of water by flushing dry N_2 at 3 L min^{-1} for 30 min. Then either a DPG or DPS meniscus is formed between the stamp features and the surface by saturated vapor at 3.5 L min^{-1} for one hour. Nanoscale features are deposited applying a stamp-sample bias (31.2 V on the substrate for 2 min using a Tektronix PS283 DC power supply). Using this technique, large arrays of both silicon (Figure 5.6c) and germanium nanostructures (Figure 5.6d) are easily fabricated. Further inspection of the samples reveals patterns spanning areas of several millimeter square. This technique can be extended to stamps fabricated using blank and written DVDs and Blu-Rays, and is also compatible with multiple AFM tips in parallel.[38]

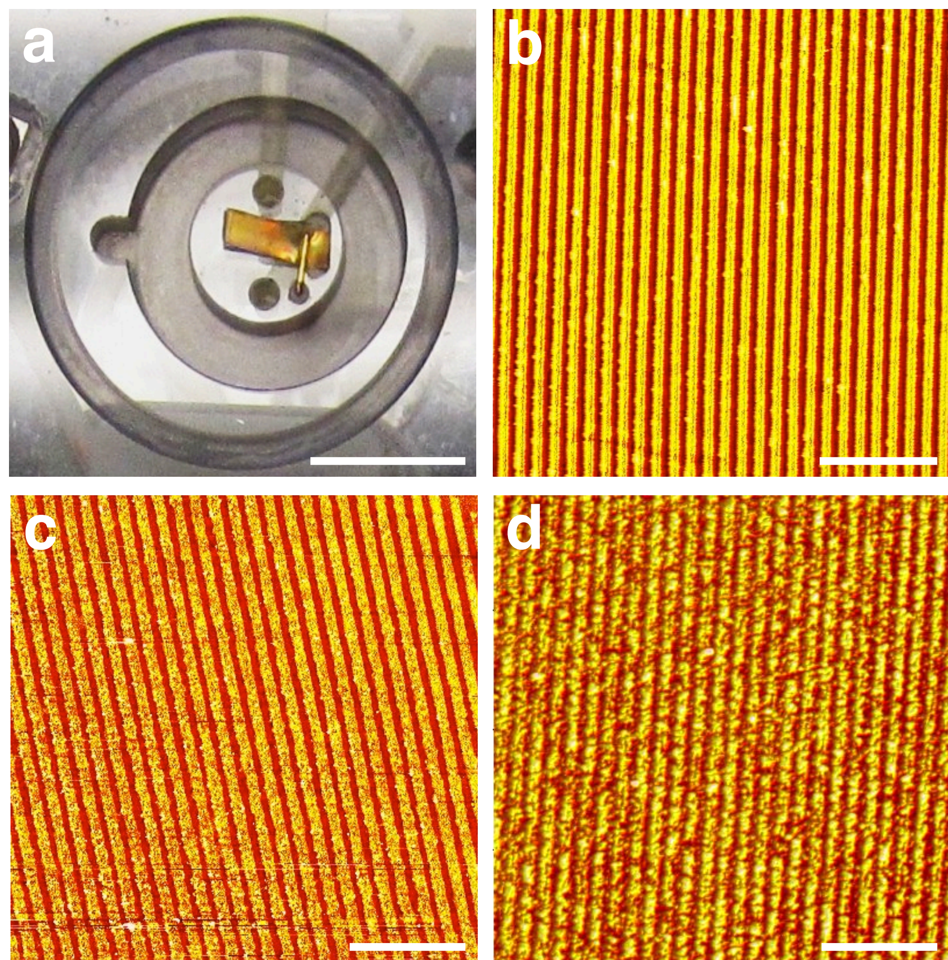

Figure 5.6. Gold coated PDMS stamp mounted in the AFM quartz liquid cell (a). Tapping mode AFM images of stamp master (b). Si structures fabricated on the Si substrate with +31 V (sample) pulse for 2 minutes (c). Ge structures fabricated on the silicon substrate with a 32 V (sample) pulse for 2 minutes (d). Scale bar =1 cm (a), 10 μm (b-d). Height scale from dark brown to bright yellow = 200 nm (b), 20 nm (c,d).

5.5.4 Large Area Reactive Stamping Using Photomask Aligner Technology

There is no fundamental limitation for how large stamps can be fabricated; stamps can be fabricated using molds of any shape or feature size. In order to demonstrate this, I have designed and built a reactive stamping add-on for a simple 4-inch mask aligner to produce stamping prototypes on the wafer-scale in conjunction with Hideki Sato from the Japanese Patent Office. For applications where crystallinity or feature size is not the greatest concern (eg. Si photovoltaics), this technology could be of future interest for large-scale production of nanoscale features.

Mask aligners, typically used for photolithography, have built in features for alignment and contact. Additionally, most mask aligners feature a wafer chuck, which holds the wafer in place using an applied vacuum, and a gas purge line. We eliminate the photolithography aspects of the mask aligner and concentrate on its ability to bring into contact wafers with large lithography areas. Replica molding as described in 5.5.1 was used to produce stamps with a diameter of 4.7" (the average diameter of a CD, Fig. 5.7a). In the large area-patterning scheme, standard quartz mask replaces the AFM liquid cell, and provides the solid backing for the flexible stamp (Fig. 5.7b-1). The stamp is mounted on the quartz mask and a 5nm Cr adhesion layer followed by a 50 nm Au layer evaporation. Electrical contact between the mask and the stamp is obtained through connecting the Au layers on each with silver paste. The gas purge lines on a standard 4" aligner have been modified (Fig. 5.7b-2) to allow the flow of nitrogen and diphenylgermane or diphenylsilane to the reactive stamping area (Fig 5.7b-3). Contact is performed visually and confirmed by monitoring the conductivity between the stamp and substrate. After the flowing the precursor for an adequate time period, contact is made, and a voltage is applied between the stamp and substrate (Fig 5.7b-4). By simply rotating the substrate

and introducing a different precursor to the system, complex heterostructures can be fabricated over a large scale.

Future work on the development of this technology will include demonstration of Ge and Si wafer scale stamping. Initial testing of the mask aligner stamping add-on have shown promising results for producing oxide features with a water meniscus. Currently several polymers with different elastic modulus are available for making the stamp. Furthermore, harder coatings, such as diamond-like carbon, will improve stamp lifetime. Both of these options will be explored by future group members.

a

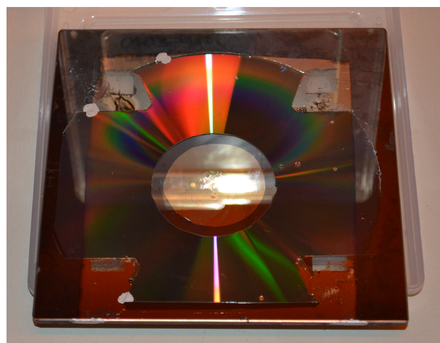

Figure 5.7. Gold-coated PDMS stamped fabricated from an entire CD (a). Schematic of wafer-scale reactive stamping prototype (b), including mounting of wafer-scale stamp (b1), retrofitting gas purge lines (b2,3), and application of an external voltage (b4).

5.6 Conclusions

In conclusion, we have demonstrated that Si, Ge, and SiGe nanostructures can be easily fabricated with AFM and microcontact printing direct-write with commercially available precursors. AFM direct write merges the deterministic placement control of nanolithography with the chemical control of bottom-up growth in a single process. High throughput fabrication has been demonstrated using conducting nanostructured stamps to produce large arrays of Ge and Si nanostructures. This proof-of-concept demonstration lays the groundwork for the expansion of this technique to extensive library of CVD precursors. By exploiting this library, the direct write and stamping approaches can provide a cost-effective approach to a wide variety of materials for devices.

5.7 Referencess

1 Vasko, S. E. *et al.* Serial and Parallel Si, Ge, and SiGe Direct Write with Scanning Probes and Conductive Stamps. *Nano Letters* **11**, 2386-2389 (2011).

2 Ko, H. *et al.* Ultrathin compound semiconductor on insulator layers for high performance nanoscale transistors. *Nature* **468**, 286-289 (2010).

3 Yoon, J. *et al.* GaAs photovoltaics and optoelectronics using releasable multilayer epitaxial assemblies. *Nature* **465**, 329-333 (2010).

4 Paniccia, M., Rao, R. M. & Yee, W. M. Optical Probing of Flip Chip Packaged Microprocessors. *Journal of Vacuum Science and Technology B* **16**, 3625-3630 (1998).

5 Chen, R. *et al.* Nanolasers grown on silicon. *Nature Photonics* **5**, 1-6 (2011).

6 Greytak, A. B., Lauhon, L. J., Gudiksen, M. S. & Lieber, C. M. Growth and Transport Properties of Complementary Germanium Nanowire Field-Effect Transistors. *Applied Physics Letters* **84**, 4176-4178 (2004).

7 Wu, Y., Xiang, J., Yang, C., Lu, W. & Lieber, C. M. Single-crystal metallic nanowires and metal/semiconductor nanowire heterostructures. *Nature* **430**, 61-65 (2004).

8 Soref, R. The Past, Present, and Future of Silicon Photonics. *IEEE Journal of Selected Topics in Quantum Electronics* **12**, 1678-1687 (2006).

9 Tromp, R. M. & Ross, F. M. Advances in In Situ Ultra High Vacuum Electron Microscopy: Growth of SiGe on Si. *Annual Review of Materials Science* **30**, 431-439 (2000).

10 Mooney, P. M. & Chu, J. O. SiGe Technology: Heteroepitaxy and High-Speed Microelectronics. *Annual Review of Materials Science* **30**, 335-362 (2000).

11 Lill, M. & Schroder, B. Preparation of amorphous hydrogentated silicon-germanium material and solar cells using the thermocatalytic chemical vapor deposition. *Applied Physics Letters* **74**, 128401286 (1999).

12 Meyerson, B. S. UHV/CVD growth of Si and Si:Ge alloys: chemistry, physics, and device applications. *Proceedings of the IEEE* **80**, 1592-1608 (1992).

13 Potapov, A. V., Orlov, L. K. & Ivin, S. V. The growth kinetics of Si1-xGex layers from SiH4 and GeH4. *Thin Solid Films* **336**, 191-195 (1999).

14 Kuykendall, T. *et al.* Crystallographic Alignment of High-Density Gallium Nitride Nanowire Arrays. *Nature Materials* **3**, 524-528 (2004).

15 Tian, B., Xie, P., Kempa, T. J., Bell, D. C. & Lieber, C. M. Single crystalline kinked semiconductor nanowire superstructures. *Nature Nanotechnology* **4**, 824-829 (2009).

16 Laracuente, A., Bronikowski, M. J. & Gallagher, A. Chemical Vapor Deposition of Nanometer-Size Aluminum Features on Silicon Surfaces Using an STM Tip. *Applied Surface Science* **107**, 11-17 (1996).

17 Kent, A., Shaw, T., von Molnar, S. & Awschalom, D. D. Growth of High Aspect Ratio Nanometer-Scale Magnets with Chemical Vapor Deposition and Scanning Tunneling Microscopy. *Science* **262**, 1249-1252 (1993).

18 Ehrichs, E. E., Yoon, S. & de Lozanne, A. L. Direct writing of 10 nm features with the scanning tunneling microscope. *Applied Physics Letters* **53**, 2287-2289 (1988).

19 Wei, Z. *et al.* Nanoscale Tunable Reduction of Graphene Oxide for Graphene Electronics. *Science* **11**, 1373-1376 (2010).

20 Pellegrino, L. *et al.* (Fe, Mn)3O4 Nanochannels Fabricated by AFM Local-Oxidation Nanolithography using Mo/Poly(methyl methacrylate) Nanomasks. *Advanced Materials* **18**, 3099-3104 (2006).

21 Germain, J., Rolandi, M., Backer, S. A. & Frechet, J. M. J. Sulfur as a novel nanopatterning material: an ultrathin resist and a chemically addressable template for nanocrystal self assembly. *Advanced Materials* **20**, 4526-4529 (2008).

22 Rolandi, M., Quate, C. F. & Dai, H. A New Scanning Probe Lithography Scheme with a Novel Metal Resist *Advanced Materials* **14**, 191-194 (2002).

23 Tseng, A. A., Notargiacomo, A. & Chen, T. P. Nanofabrication by Scanning Probe Microscope Lithography: A Review. *Journal of Vacuum Science and Technology B* **23** (2005).

24 Knoll, A. W. *et al.* Probe-Based 3-D Nanolithography Using Self-Amplified Depolymerization Polymers *Advanced Materials* **22** (2010).

25 Pires, D. *et al.* Nanoscale Three-Dimensional Patterning of Molecular Resists by Scanning Probes. *Science* **328** (2010).

26 Braunschweig, A. B., Huo, F. & Mirkin, C. A. Molecular Printing. *Nature Chemistry* **1**, 353-358 (2009).

27 Bellido, E., de Miguel, R., Ruiz-Molina, D., Lostao, A. & Maspoch, D. Controlling the Number of Proteins with Dip-Pen Nanolithography. *Advanced Materials* **22**, 352-355 (2009).

28 Rolandi, M., Suez, I., Scholl, A. & Frechet, J. M. J. Fluorocarbon Resist for High-Speed Scanning Probe Lithography. *Angewandte Chemie International Edition* **46**, 7477-7480 (2007).

29 Suez, I. *et al.* High-Field Scanning Probe Lithography in Hexadecane: Transition from Field Induced Oxidation to Solvent Decomposition through Surface Modification. *Advanced Materials* **19**, 3570-3573 (2007).

30 Salaita, K. *et al.* Massively Parallel Dip-Pen Nanolithography with 55000-Pen Two-Dimensional Arrays. *Angewandte Chemie* **118**, 7378-7381 (2006).

31 Martinez, R. V., Losilla, N. S., Martinez, J., Huttel, Y. & Garcia, R. *Nano Letters* **7**, 1846-1850 (2007).

32 Torrey, J. D. *et al.* Scanning Probe Direct-Write of Germanium Nanostructures. *Advanced Materials* **22**, 4639-4642 (2010).

33 Vasko, S. E. *et al.* Insights into the high field chemistry of diphenylgermane. *Physical Chemistry Chemical Physics* **13**, 4842-4845 (2011).

34 Rolandi, M., Suez, I., Scholl, A. & Frechet, J. M. J. Fluorocarbon Resist for High-Speed Scanning Proble Lithography. *Angewandte Chemie-International Edition* **46**, 7477-7480 (2007).

35 Suez, I. *et al.* High-field scanning probe lithography in hexadecane: transitioning from field induced oxidation to solvent decomposition through surface modification. *Advanced Materials* **19**, 3570-3573 (2007).

36 Ginger, D. S., Zhang, H. & Mirkin, C. A. The evolution of dip-pen nanolithography. *Angewandte Chemie-International Edition* **43**, 30-45 (2004).

37 Albonetti, C. *et al.* Parallel-local anodic oxidation of silicon surfaces by soft stamps. *Nanotechnology* **19**, 43530:1-9 (2008).

38 Rolandi, M. *et al.* Inorganic Nanostructre Reactive Direct-Write and Growth. United States of America patent (2012).

Bibliography

1 *Photoemission Electron Microscopy Ultrafast Dynamics-Tutorial-PEEM Technique*, 2009).

2 Albonetti, C. *et al.* Parallel-local anodic oxidation of silicon surfaces by soft stamps. *Nanotechnology* **19**, 43530:43531-43539 (2008).

3 Anstankova, K. N. *et al.* Scanning-probe-induced local decomposition of solid germanium monoxide films: The nano-patterning of Germanium. *Journal of Surface Investigation: X-Ray, Synchrotron, and Neutron Techiques* **3**, 773-780 (2009).

4 Avouris, P., Hertel, T. & Martel, R. Atomic Force Microscope Tip-Induced Lodal Oxidation of Silicon: Kinetics, Mechanism, and Nanofabrication. *Applied Physics Letters* **71**, 285-287, doi:10.1063/1.119521 (1997).

5 Backer, S. A., Suez, I., Fresco, Z. M., Rolandi, M. & Frechet, J. M. J. Covalent formation of nanoscale fullerene and dendrimer patterns. *Langmuir* **23**, 2297-2299, doi:Doi 10.1021/La0631973 (2007).

6 Bard, A. J. & Faulkner, L. R. *Electrochemical Methods*. Second edn, (John Wiley & Sons, 2001).

7 Belin, E., Cardinaud, C., Senemaud, C. & Dixmier, J. X-Ray absorption spectroscopy study of Ge Empty States in Crystalline and Amorphous Phases, Amorphous Ge:H and Si1-xGex:H. *Journal of Non-Crystalline Solids* **77&78**, 331-334 (1985).

8 Bellido, E., de Miguel, R., Ruiz-Molina, D., Lostao, A. & Maspoch, D. Controlling the Number of Proteins with Dip-Pen Nanolithography. *Advanced Materials* **22**, 352-355 (2009).

9 Berger, S. D. & McKenzie, D. R. EELS analysis of vacuum arc-deposited diamond-like films. *Philosophical Magazine Letters* **57**, 285-290 (1988).

10 Braunschweig, A. B., Huo, F. & Mirkin, C. A. Molecular Printing. *Nature Chemistry* **1**, 353-358 (2009).

11 Brook, M. A. *Silicon in Organic, Organometallic, and Polymer Chemistry*. (John Wiley & Sons, 2000).

12 Buriak, J. M. Organometalic Chemistry on Silicon Germanium Surfaces. *Chemical Reviews* **102**, 1271-1308 (2002).

13 Calle, L. M. & Kana'an, A. S. Enthalpies and entropies of sublimation of tetraphenylsilane and hexaphenyldisilane. The bond dissociation energies of Si-C and Si-Si. *Journal of Chemical Thermodynamics* **6**, 935-942 (1974).

14 Calvaresi, M. *et al.* Splitting CO2 with Electric Fields: A Computational Investigation. *Journal of Physical Chemistry Letters* **1**, 3256-3260 (2010).

15 Cen, C., Thiel, S., Mannhart, J. & Levy, J. Oxide Nanoelectronics on Demand. *Science* **323**, 1026-1030, doi:Doi 10.1126/Science.1168294 (2009).

16 Chen, R. *et al.* Nanolasers grown on silicon. *Nature Photonics* **Advance Article**, 1-6 (2011).

17 Chockla, A. M. & Korgel, B. A. Seeded germanium nanowire synthesis in solution. *Journal of Materials Chemistry* **19**, 996-1001, doi:Doi 10.1039/B816954c (2009).

18 Crozier, P. A., Tolle, J., Kouvetakis, J. & Ritter, C. Synthesis of uniform GaN quantum dot arrays via electron nanolithography of D2GaN3. *Applied Physics Letters* **84**, 3441-3443 (2003).

19 Dagata, J. A. *et al.* Modification of hydrogen-passivated silicon by a scanning tunneling microscope operating in air. *Applied Physics Letters* **56**, 2001-2003 (1990).

20 Day, H. C. & Alleee, D. R. Selective Area Oxidation of Silicon With Scanning Force Microscope. *Applied Physics Letters* **62**, 2691-2693 (1993).

21 deLozanne, A. Pattern Generation below 0.1 micron by Localized Chemical Vapor Deposition with the Scanning Tunneling Microscope. *Japanese Journal of Applied Physics* **33**, 7090-7093 (1994).

22 Distefano, G., Fignataro, S., Szepes, L. & Borossay, J. Photoelectron Spectroscopy Study of the Triphenyl Derivatives of the Group IV Elements. *Journal of Organometallic Chemistry* **104**, 173-178 (1976).

23 Egorochkin, A. N. *et al.* Frequencies of Ge-H Stretching Modes and the Effect of dπ -pπ Interaction in Organogermanium Compounds. *Journal of Organometallic Chemistry* **76**, 29-36 (1974).

24 Ehrichs, E. E., Yoon, S. & de Lozanne, A. L. Direct writing of 10 nm features with the scanning tunneling microscope. *Applied Physics Letters* **53**, 2287-2289 (1988).

25 Ehrics, E. E., Yoon, S. & de Lozanne, A. L. Direct writing of 10 nm features with the scanning tunneling microscope. *Applied Physics Letters* **53**, 2287-2289 (1988).

26 Fallon, P. J. & Brown, L. M. Analysis of Chemical-Vapour-Deposited Diamond Grain Boundaries Using Transmission Electron Mircroscopy and Parallel Electron Energy Loss Spectroscopy in a Scanning Tunneling Electron Microscope. *Diamond and Related Materials* **2**, 1004-1011 (1993).

27 Fenwick, G. *et al.* Thermochemical nanopatterning of organic semiconductors. *Nature Nanotechnology* **4**, 664-668 (2009).

28 Fleming, J. W. & Banwell, C. N. Internal Rotation in Phenylsilane and Phenylgermane and their -D3 derivatives. *Journal of Molecular Spectroscopy* **31**, 318-340 (1969).

29 Freeburger, M. E. & Spialter, L. Physical Organosilicon Chemistry. I. Nuclear Magnetic Resonance Studies of Ortho-, Meta-, and Para-Substituted Phenyltrimethylsilanes. Evidence Bearing on the Existence of (p→ d) π "Back-Bonding" in Phenylsilanes. *Journal of the American Chemical Society* **93**, 1894-1898 (1971).

30 Fresco, Z. M. & Frechet, J. M. J. Selective surface activation of a functional monolayer for the fabrication of nanometer scale thiol patterns and directed self-assembly of gold nanoparticles. *Journal of the American Chemical Society* **127**, 8302-8303 (2005).

31 Fresco, Z. M., Suez, I., Backer, S. A. & Frechet, J. M. J. AFM-induced amine deprotection: Triggering localized bond cleavage by application of tip/substrate voltage bias for the surface self-assembly of nanosized dendritic objects. *Journal of the American Chemical Society* **126**, 8374-8375 (2004).

32 Fu, L., Liu, X., Zhang, Y., Dravid, V. P. & Mirkin, C. A. Nanopatterning of "Hard" Magnetic Nanostructures via Dip-Pen Nanolithography and a Sol-Based Ink. *Nano Letters* **3**, 757-760 (2003).

33 Fuller, G. E. in *SPIE.* 14-27.

34 Garcia, R. *et al.* Nanopatterning of carbonaceous structures by field-induced carbon dioxide splitting with a force microscope. *Applied Physics Letters* **96**, -, doi:Artn 143110
Doi 10.1063/1.3374885 (2010).

35 Garcia, R., Martinez, R. V. & Martinez, J. Nano-chemistry and scanning probe nanolithographies. *Chemical Society Reviews* **35**, 29-38 (2006).

36 Germain, J., Rolandi, M., Backer, S. A. & Frechet, J. M. J. Sulfur as a Novel Nanopatterning Material: An Ultrathin Resist and a Chemically Addressable Template

for Nanocrystal Self-Assembly. *Advanced Materials* **20**, 4526-4529, doi:Doi 10.1002/Adma.200802024 (2008).

37 Ginger, D. S., Zhang, H. & Mirkin, C. A. The evolution of dip-pen nanolithography. *Angewandte Chemie-International Edition* **43**, 30-45 (2004).

38 Glover, C. J., Ridgway, M. C., Llewellyn, D. J., Kluth, P. & Johanessen, B. Formation and electronic structure of germanium nanocrystals formed by ion beam synthesis. *Nuclear Instruments and Methods in Physics Research B* **238**, 306-209 (2005).

39 Gohlke, S., Rosa, A., Illenberger, E., Bruning, F. & Huels, M. A. Formation of Anion Fragments from Gas-Phase Glycine by Low Energy (0-15 eV) Electron Impact. *Journal of Chemical Physics* **116**, 10164-10169 (2002).

40 Gotsman, B., Duerig, U., Frommer, J. & Hawker, C. J. Exploiting Chemical Switching in a Diels-Alder Polymer for Nanoscale Probe Lithography and Data Storage. *Advanced Functional Materials* **16**, 1499-1505 (2006).

41 Greytak, A. B., Lauhon, L. J., Gudiksen, M. S. & Lieber, C. M. Growth and Transport Properties of Complementary Germanium Nanowire Field-Effect Transistors. *Applied Physics Letters* **84**, 4176-4178 (2004).

42 Hagenhoff, B. *Mikrochimica Acta* **132**, 259-271 (2000).

43 Heigl, F. *et al.* in *14th International Conference on X-Ray Absorption Fine Structure (XAFS14)* Vol. 190 012130: 012131-012136 (Journal of Physics Conference Series, 2009).

44 Henderson, W. & McIndoe, J. S. *Mass Spectrometry of Inorganic, Coordination, and Organometallic Compounds*. 47-54 (John Wiley & Sons, 2005).

45 Intel. *Moore's Law Inspires Intel Innovation*, <http://www.intel.com/content/www/us/en/silicon-innovations/moores-law-technology.html> (2012).

46 Ito, H. Chemical Amplification Resists: History and Development within IBM. *IBM Journal of Research Development* **41**, 119-130 (1997).

47 Jang, J.-W. *et al.* Electrically Biased Nanolithography with KOH-Coated AFM Tips. *Nano Letters* **8**, 1451-1455 (2008).

48 Johnson, O. H. & Harris, D. M. Diphenylgermane and dihalodiphenylgermane. *Journal of American Chemical Society* **75**, 5564-5566 (1950).

49 Kana'an, A. S. Enthalpies and entropies of sublimation of germanium tetraphenyl and di-germanium hexaphenyl. The bond dissociation energy of Ge-C and Ge-Ge. *Journal of Chemical Thermodynamics* **6**, 191-199 (1974).

50 Kent, A., Shaw, T., von Molnar, S. & Awschalom, D. D. Growth of High Aspect Ratio Nanometer-Scale Magnets with Chemical Vapor Deposition and Scanning Tunneling Microscopy. *Science* **262** (1993).

51 Kim, Y., Kang, S. K., Choi, I., Lee, J. & Yi, J. In situ Negative Patterning of p-Silicon via Scanning Probe Lithography in HF/EtOH Liquid Bridges. *Journal of American Chemical Society* **127**, 9380-9381 (2005).

52 Kita, K. *et al.* Control of high-k/germanium interface properties through selection of high-k materials and suppression of GeO volatilization. *Applied Surface Science* **254**, 6100-6105 (2008).

53 Knoll, A. W. *et al.* Probe-Based 3-D Nanolithography Using Self-Amplified Depolymerization Polymers *Advanced Materials* **22** (2010).

54 Ko, H. *et al.* Ultrathin compound semiconductor on insulator layers for high performance nanoscale transistors. *Nature* **468**, 286-289 (2010).
55 Kolb, D. M., Ullman, R. & Will, T. Nanofabrication of Small Copper Clusters on Gold(111) Electrodes by a Scanning Tunneling Microscope. *Science* **275**, 1097-1099 (1997).
56 Koops, H. W. P., Kaya, A. & Weber, M. Fabrication and characterization of platinum nanocrystalline material grown by electron‐beam induced deposition. *Journal of Vacuum Science and Technology B* **13**, 2400-2403 (1995).
57 Kreuzer, H. J. Physics and chemistry in high electric fields *Surface Science* **246**, 336-347 (1990).
58 Kreuzer, H. J. Physics and chemistry in high electric fields. *Surface and Interface Analysis* **36**, 372-379 (2004).
59 Kuykendall, T. *et al.* Crystallographic Alignment of High-Density Gallium Nitride Nanowire Arrays. *Nature Materials* **3**, 524-528 (2004).
60 Landis, S. *Nano-Lithography*. (Wiley, 2011).
61 Lang, L. *Absorption Spectra in the Ultraviolet and Visible Region*. Vol. 9 (Academic Press, 1967).
62 Laracuente, A., Bronikowski, M. J. & Gallagher, A. Chemical Vapor Deposition of Nanometer-Size Aluminum Features on Silicon Surfaces Using an STM Tip. *Applied Surface Science* **107**, 11-17 (1996).
63 Lee, J., Sorescu, D. C. & Deng, X. Electron-Induces Dissociation of CO2 on TiO2(110). *Journal of American Chemical Society* **133**, 10066-10069 (2011).
64 Lee, M., O'Hayre, R., Prinz, F. B. & Gur, T. M. Electrochemical nanopatterning of Ag on solid-state ionic conductor RbAg4I5 using atomic force microscopy. *Applied Physics Letters* **85**, 3552-3554 (2004).
65 Li, Y., Maynor, B. W. & Liu, J. Electrochemical AFM "Dip-Pen" Nanolithography. *Journal of American Chemical Society* **123**, 2105-2106 (2001).
66 Liang, D. & Bowers, J. E. Photonic integration: Si or InP substrates? *Electronics Letters* **45**, 578 - 581 (2009).
67 Lill, M. & Schroder, B. Preparation of amorphous hydrogentated silicon-germanium material and solar cells using the thermocatalytic chemical vapor deposition. *Applied Physics Letters* **74**, 128401286 (1999).
68 Long, D. A., Unal, K., Pratt, R. C., Malkoch, M. & Frommer, J. Localized "click" chemistry through dip-pen nanolithography. *Advanced Materials* **19**, 4471-4473 (2007).
69 Lyubinetsky, I., Mezhenny, S., Choyke, W. J. & Yates, J. T. Two Mechanism of Scanning Tunneling Microscope Assisted Nanostructure Formation Using Precursor Molecules. *Journal of Vacuum Science and Technology A* **17**, 1445-1450 (1999).
70 Mackay, K. M. *The Chemistry of Organic Germanium, Tin, and Lead Compounds*. (John Wiley & Sons, 1995).
71 Maoz, R., Frydman, E., Cohen, S. R. & Sagiv, J. “Constructive Nanolithography”: Inert Monolayers as Patternable Templates for In-Situ Nanofabrication of Metal–Semiconductor–Organic Surface Structures—A Generic Approach
. *Advanced Materials* **12**, 725-731 (2000).
72 Marchi, F. *et al.* Direct patterning of noble metal nanostructures with a scanning tunneling microscope. *Journal of Vacuum Science and Technology B* **18**, 1171-1176 (2000).

73 Martinez, R. V. & Garcia, R. Nanolithography based on the formation and manipulation of nanometer-size organic liquid menisci. *Nano Letters* **5**, 1161-1164 (2005).

74 Martinez, R. V., Losilla, N. S., Martinez, J., Huttel, Y. & Garcia, R. Patterning polymeric structures with 2 nm resolution at 3 nm half pitch in ambient conditions. *Nano Letters* **7**, 1846-1850 (2007).

75 May, O., Kubala, D. & Allan, M. Dissociative Electron Attachment to Pt(PF3)4-A Precursor for Focused Electron Beam Induced Processing (FEBIP). *Physical Chemistry Chemical Physics* **14**, 2979-2982 (2012).

76 Mayer, J., Giannuzzi, L. A., Kamino, T. & Michael, J. TEM Sample Preparation and FIB-Induced Damage. *MRS Bulletin* **32**, 400-407 (2007).

77 Maynor, B. W., Li, Y. & Liu, J. Au "Ink" for AFM "Dip-Pen" Nanolithography. *Langmuir* **17**, 2575-2578 (2001).

78 Melo, L. V. & Brogueira, P. in *Materials Research Society Spring Meeting.* (Cambridge University Press).

79 Meyerson, B. S. UHV/CVD growth of Si and Si:Ge alloys: chemistry, physics, and device applications. *Proceedings of the IEEE* **80** (1992).

80 Mooney, P. M. & Chu, J. O. SiGe Technology: Heteroepitaxy and High-Speed Microelectronics. *Annual Review of Materials Science* **30**, 335-362 (2000).

81 Mui, C., Bent, S. F. & Musgrave, C. B. A Theoretical Study of the Structure and Thermochemistry of 1,3-Butadiene on the Ge/Si(100)-2x1 Surface. *Journal of Physical Chemistry A* **104**, 2457-2462 (2000).

82 Naoe, S. *et al.* L3 Absorption Spectrum of Germanium Single Crystal. *Journal of Electron Spectroscopy and Related Phenomena* **79**, 5-8 (1996).

83 Oliveira, A. B., Medeiros-Ribeiro, G. & Azevedo, A. Submicron fabrication by local anodic oxidation of germanium thin films. *Nanotechnology* **20** (2009).

84 Oster, T., Kunh, A. & Illenberger, E. Gas Phase Negative Ion Chemistry. *International Journal of Mass Spectrometry and Ion Processes* **89**, 1-72 (1989).

85 Paniccia, M., Rao, R. M. & Yee, W. M. Optical Probing of Flip Chip Packaged Microprocessors. *Journal of Vacuum Science and Technology B* **16**, 3625-3630 (1998).

86 Pellegrino, L. *et al.* (Fe, Mn)3O4 Nanochannels Fabricated by AFM Local-Oxidation Nanolithography using Mo/Poly(methyl methacrylate) Nanomasks. *Advanced Materials* **18**, 3099-3104 (2006).

87 Pires, D. *et al.* Nanoscale Three-Dimensional Patterning of Molecular Resists by Scanning Probes. *Science* **328**, 732-735, doi:Doi 10.1126/Science.1187851 (2010).

88 Potapov, A. V., Orlov, L. K. & Ivin, S. V. The growth kinetics of Si1-xGex layers from SiH4 and GeH4. *Thin Solid Films* **336**, 191-195 (1999).

89 Rauscher, H., Behrendt, F. & Behm, R. J. Fabrication of surface nanostructures by scanning tunneling microscope induced decomposition of SiH4 and SiH2Cl2. *J Vac Sci Technol B* **15**, 1373-1377 (1997).

90 Roelkens, G. *et al.* III-V/silicon photonics for on-chip and intra-chip optical interconnects. *Laser & Photonics Reviews* **4**, 751-779 (2010).

91 Rolandi, M. *et al.* Inorganic Nanostructre Reactive Direct-Write and Growth. United States of America patent (2012).

92 Rolandi, M., Quate, C. F. & Dai, H. A New Scanning Probe Lithography Scheme with a Novel Metal Resist *Advanced Materials* **14**, 191-194 (2002).

93 Rolandi, M., Suez, I., Dai, H. & Frechet, J. M. J. Dendrimer Monolayers as Negative and Positive Tone Resists for Scanning Probe Lithography. *Nano Letters* **4**, 889-893 (2004).

94 Rolandi, M., Suez, I., Scholl, A. & Frechet, J. M. J. Fluorocarbon Resist for High-Speed Scanning Proble Lithography. *Angewandte Chemie-International Edition* **46**, 7477-7480 (2007).

95 Salaita, K. *et al.* Massively Parallel Dip–Pen Nanolithography with 55 000-Pen Two-Dimensional Arrays. *Angewandte Chemie International Edition* **45**, 7220-7223 (2006).

96 Salaita, K., Wang, Y. & Mirkin, C. A. Applications of Dip-Pen Nanolithography. *Nature Nanotechnology* **2**, 145-155 (2007).

97 Snow, E. S. & Campbell, P. M. Fabrication of Si Nanostructures with an Atomic Force Microscope. *Applied Physics Letters* **64**, 1932-1934, doi:10.1063/1.111746 (1994).

98 Snow, E. S., Jernigan, G. G. & Campbell, P. M. The Kinetics and Mechanism of Scanned Probe Oxidation of Si. *Applied Physics Letters* **76**, 1782-1784 (2000).

99 Sodhi, R. N. S. Time-of-flight secondary ion mass spectrometry (TOF-SIMS):— versatility in chemical and imaging surface analysis. *The Analyst* **129**, 483-487 (2004).

100 Soh, H. T., Guarini, K. W. & Quate, C. F. *Scanning Probe Lithography*. (Kluwer Academic Publishers, 2001).

101 Song, J. Q. *et al.* Fabrication of Gold Nanostructures on Graphite Using Atomic Force Microscope. *Molecular Crystal Liquid Crystal Science and Technology Section A* **294-295**, 51 (1997).

102 Soref, R. The Past, Present, and Future of Silicon Photonics. *IEEE Journal of Selected Topics in Quantum Electronics* **12**, 1678-1687 (2006).

103 Streetman, B. G. & Banerjee, S. *Solid State Electronic Devices-5th Ed.*, (Prentice Hall, 2000).

104 Suez, I., Backer, S. A. & Frechet, J. M. J. Generating an etch resistant "resist" layer from common solvents using scanning probe lithography in a fluid cell. *Nano Letters* **5**, 321-324 (2005).

105 Suez, I. *et al.* High-Field Scanning Probe Lithography in Hexadecane: Transition from Field Induced Oxidation to Solvent Decomposition through Surface Modification. *Advanced Materials* **19**, 3570-3573 (2007).

106 Szoszkiewicz, R. *et al.* High-Speed, Sub-15 nm feature size thermochemical nanolithography. *Nano Letters* **7**, 1064-1069 (2007).

107 Tello, M. & Garcia, R. Giant growth rate in nano-oxidation of p-silicon surfaces by using ethyl alcohol liquid bridges. *Applied Physics Letters* **83**, 2339-2341, doi:10.1063/1.1613799 (2003).

108 Tian, B., Xie, P., Kempa, T. J., Bell, D. C. & Lieber, C. M. Single crystalline kinked semiconductor nanowire superstructures. *Nature Nanotechnology* **4**, 824-829 (2009).

109 Torrey, J. D. *et al.* Scanning Probe Direct-Write of Germanium Nanostructures. *Advanced Materials* **22**, 4639-4642 (2010).

110 Tromp, R. M. & Ross, F. M. Advances in In Situ Ultra High Vacuum Electron Microscopy: Growth of SiGe on Si. *Annual Review of Materials Science* **30**, 431-439 (2000).

111 Tseng, A. A., Notargiacomo, A. & Chen, T. P. Nanofabrication by Scanning Probe Microscope Lithography: A Review. *Journal of Vacuum Science and Technology B* **23** (2005).

112 Unruh, D. A., Mauldin, C., Pastine, S. J., Rolandi, M. & Frechet, J. M. J. Bifunctional Patterning of Mixed Monolayer Surfaces Using Scanning Probe Lithography for Multiplexed Directed Assembly. *Journal of American Chemical Society* **2010**, 6890-6891 (2010).

113 Uosaki, K., Koinuma, M., Sekine, N. & Ye, S. in *Solid-Liquid Electrochemical Interfaces ACS Symposium Series* Ch. 14, 189-201 (American Cehmical Society, 1997).

114 Vasko, S. E. *et al.* Insights into the high field chemistry of diphenylgermane. *Physical Chemistry Chemical Physics* **13**, 4842-4845 (2011).

115 Vasko, S. E. *et al.* (2012).

116 Vasko, S. E. *et al.* Serial and Parallel Si, Ge, and SiGe Direct Write with Scanning Probes and Conductive Stamps. *Nano Letters* **11**, 2386-2389 (2011).

117 Vettiger, P. *et al. IBM Journal of Research Development* **44**, 323-340 (2000).

118 Vinet, M. *et al.* Germanium on Insulator and New 3D Architecture Opportunities for Integration. *Intenational Journal of Nanotechnology* **7**, 304-319 (2010).

119 Virwani, K. R., Malshe, A. P. & Rajurkar, K. P. Understanding sub-20 nm breakdown behavior of liquid dielectrics. *Physical Review Letters* **99** (2007).

120 Wang, D., Chang, Y.-L., Liu, Z. & Dai, H. Oxidation Resistant Germanium Nanowires: Bulk Synthesis, Long Chain Alkanethiol Functionalization, and Langmuir−Blodgett Assembly. *Journal of American Chemical Society* **127**, 11871-11875 (2005).

121 Wang, D. & Dai, M. *Applied Physics A: Materials Science & Processing* **85**, 217-225 (2006).

122 Wang, D. *et al.* Thermochemical Nanolithography of Multifunctional Nanotemplates for Assembling Nano-Objects. *Advanced Functional Materials* **19**, 3969-3702 (2009).

123 Wei, Y.-M. *et al.* The Creation of Nanostructures on an Au(111) Electrode by Tip-Induced Iron Deposition from an Ionic Liquid. *Small* **4**, 1355-1358 (2008).

124 Wei, Z. *et al.* Nanoscale Tunable Reduction of Graphene Oxide for Graphene Electronics. *Science* **11**, 1373-1376 (2010).

125 Wilder, K., Soh, H. T., Atalar, A. & Quate, C. F. Nanometer-scale patterning and individual current-controlled lithography using multiple scanning probes. *Review of Scientific Instruments* **70**, 2822-2828 (1999).

126 Wu, Y., Xiang, J., Yang, C., Lu, W. & Lieber, C. M. Single-crystal metallic nanowires and metal/semiconductor nanowire heterostructures. *Nature* **430**, 61-65 (2004).

127 Xie, T. *et al.* Characterization and growth mechanism of germanium nitride nanowires prepared by an oxide assisted method. *Journal of Crystal Growth* **283** (2005).

128 Xie, X. N. *et al.* Creating polymer structures of tunable electric functionality by nanoscale discharge-assisted cross-linking and oxygenation. *J Am Chem Soc* **128**, 2738-2744, doi:10.1021/ja0577241 (2006).

129 Yanagi, H. & Ohno, T. Nanofabrication of Gold Particles in Glass Films by AFM-Assisted Local Reduction. *Langmuir* **15**, 4773-4776 (1999).

130 Yeung, K. L. & Yao, N. Scanning Probe Microscopy in Catalysis. *Journal of Nanoscience and Nanotechnology* **4**, 647-690 (2004).

131 Yoon, J. *et al.* GaAs photovoltaics and optoelectronics using releasable multilayer epitaxial assemblies. *Nature* **465**, 329-333 (2010).

132 Ziethen, C. *et al.* Orbital Mapping of Carbon Thin Films by XANES-spectromicroscopy. *Journal of Electron Spectroscopy and Related Phenomena* **107**, 261-271 (2000).

Appendix A. Experimental Methods

Si (100) substrates (Addison Engineering, B doped, resistivity ρ =0.001-0.005 Ω cm, native oxide thickness ≈2 nm) are cut to ~12mm x ~12mm squares and scratched with a diamond scribe from the center to the bottom edge. They are then cleaned by sonication in acetone, isopropyl alcohol, ethanol, DI water, and annealing in Ar at 550° C for 60 minutes. Nanostructure direct-write was performed on a Veeco Multimode V AFM with a fluid cell operated in contact mode with Sb-doped Si cantilevers (Nanoworld, ρ= 0.02–0.025 Ω cm, spring constant k ≈0.2 N m^{-1}). A bias was applied to the sample (+6 to +10 V) and/or the tip (-12 to 0 V) via the Nanoscope IV controller. The force setpoint was the same as for imaging in contact mode (≈1–10 nN). Patterning at lower or higher forces did not affect the patterns as long as contact with the sample was maintained during writing. After patterning, the samples were rinsed in acetone, methanol, and isopropanol. Tapping mode imaging was performed on the same AFM with Veeco Probes TESP Si (Sb) doped cantilevers (ρ = 0.01–0.025 Ω cm, k =40 N m^{-1}, resonant frequency ν≈300 kHz). Diphenylgermane (Gelest) and diphenylsilane (Sigma-Aldrich) was filtered with a 0.2 μm Whatman filter before use.

For current measurements, the fluid cell is purged of water vapor by flushing with dry nitrogen at a rate of 4 L min-1 for 30 minutes. Diphenylgermane vapor is introduced by bubbling nitrogen carrier gas at 2 L min-1 for one hour prior to the start of the experiments. A bias is applied to the tip (-20 to 20 V) via an Agilent 4155c Semiconductor Parameter Analyzer. The force setpoint is the same as for imaging in contact mode (≈1–10 nN). Patterning at lower or higher forces does not affect the patterns as long as contact with the sample is maintained during writing. After patterning, the samples are rinsed in acetone, methanol, and isopropanol. Tapping mode imaging is performed on the same AFM with Veeco Probes TESP Si Sb doped cantilevers

(ρ= 0.01–0.025 Ω cm, k = 40 N m^{-1}, resonant frequency $\nu \approx$ 300 kHz). Current was collected during writing at different voltages with the same 4155c Semiconductor Parameter Analyzer.

Vita

Stephanie Vasko was born in Oxford, New Jersey. She graduated from Warren Hills Regional High School in 2003, and graduated magna cum laude with a BA in chemistry from Carleton College in 2007. She came to the University of Washington in 2007 and joined the Rolandi group in December 2008.

Stephanie has been awarded a National Science Foundation Integrative Graduate Education and Research Traineeship (NSF-IGERT) in 2008-2009, 2009-2010, and Spring 2011, in addition to the UW Chemistry Department West Fellowship in 2007-2008. She has been the recipient of the BASF Science Scholarship (2003), Hypercube computational chemistry award (2007), and a William Carleton Scholar (2003-2007). In 2012, she graduated with a Doctor of Philosophy in Chemistry from the University of Washington.